The Peculiar Behavior of Baroclinic Waves During the Midwinter Suppression of the Pacific Storm Track

Jeffrey Hiapo Yin

A dissertation submitted in partial fulfillment
of the requirements for the degree of

Doctor of Philosophy

University of Washington

2002

Program Authorized to Offer Degree: Atmospheric Sciences

University of Washington

Abstract

The Peculiar Behavior of Baroclinic Waves During the Midwinter Suppression of the Pacific Storm Track

by Jeffrey Hiapo Yin

Co-Chairs of Supervisory Committee:

Professor David S. Battisti
Atmospheric Sciences

Professor Edward S. Sarachik
Atmospheric Sciences

The midwinter suppression of the Pacific storm track is described in detail based on NCEP Reanalysis data from 1979 to 2001. The midwinter suppression is characterized by an equatorward shift and overall decrease in storm track intensity, measured in terms of eddy total energy (TE), that occurs primarily above 500 mb over the western and central Pacific. The suppression is accompanied by an equatorward shift and overall strengthening of the Pacific jet and a lowering of the tropopause poleward of the jet; it occurs despite the midwinter maximum in baroclinicity.

An eddy energy budget analysis is performed to examine the changes in the flow of eddy energy in baroclinic waves during midwinter. Changes in baroclinic wave structure reduce the efficiency of baroclinic generation of eddy available potential energy (APE); decreased moisture and increased static stability reduce the efficiency of baroclinic conversion of eddy APE to eddy kinetic energy (KE); and shallower baroclinic conversion reduces the

fraction of eddy KE that persists at upper levels. These effects overcome the increase in baroclinicity in midwinter to reduce the eddy TE at upper levels relative to fall and spring.

Lag regression analysis reveals that, in midwinter, temperature perturbations are shallower because of increased upper level static stability and have a larger eastward tilt with height because of the stronger Pacific jet. Shallowing of the temperature perturbations decreases the fraction of eddy KE that persists, and the shallowing and larger tilt both decrease the efficiency of baroclinic generation. The lag regression analysis also shows that baroclinic waves tilt poleward with height in all seasons because of their ageostrophic wind structure.

The combination of the effects of increased upper level static stability associated with the lowering of the tropopause causes most of the midwinter suppression of the Pacific storm track. Increased jet speed and decreased moisture make additional small contributions to the suppression. The poleward tilt with height of baroclinic waves places the maximum upper level eddy energy on the poleward side of the Pacific jet, where it is more efficiently suppressed by the lowering of the tropopause in midwinter.

TABLE OF CONTENTS

LIST OF FIGURES

LIST OF TABLES

ACKNOWLEDGMENTS

This work could never have been done without the support of a huge number of people, and I'd like to acknowledge at least a small subset of those people here. First, on the academic side: My advisors, David Battisti and Ed Sarachik, had the confidence to allow me to do a lot of exploring during my time in graduate school, both inside atmospheric sciences and out (remember Ultimate Discount Travel?), and I learned much more with this freedom to choose my path than I would have otherwise. David's enthusiasm for thinking about interesting climate problems is infectious; I very much enjoyed getting excited with him about the various problems that I tackled while in graduate school. Mike Wallace has been a great resource, particularly in recent months as he's served on my reading committee; his finely tuned sense for how to present science in a clear and focused manner has greatly improved the quality of my dissertation. Dennis Hartmann also played an important role on my committee by asking the difficult questions that forced me to think about the best way to evaluate and present my work, and I really do appreciate being pushed that way. Finally, I appreciate the time and good nature of both of my Graduate School Representatives, Mark Ghiorso of Geology and Bruce Hevly of History, because they truly made the process of graduating more pleasant.

I also received much valuable input from outside my committee. Greg Hakim deserves a world of thanks for opening his door to me every time I had a question about storm tracks, and his experience and PV perspective were important influences on my thinking. Gerard Roe has been a great mind to bounce ideas off of as well, whether I was thinking about ice sheets, baroclinic waves, or anything else in the vast expanse in between. Nili Harnik has been extremely helpful in shaping my thinking about wave propagation, and it's been

really fun exchanging ideas and “speaking the same language” with her. Eric DeWeaver also provided valuable input on my work, as well as a few laughs and a huge store of little-known facts. Dan Vimont has always provided a great sense of humor about science and life in general, and, in my dissertation, contributed his amazing command of Matlab to create the schematic diagrams that are so important for illustrating my ideas on how baroclinic waves work. Camille Li has helped to rekindle my interest in modeling lately with her enthusiasm and fresh perspective, and I particularly appreciate her assistance in the arduous task of proofreading my dissertation. Cecilia Bitz was a great officemate during my early years of graduate school, and I have appreciated the confidence that she has placed in my thinking as we’ve had stimulating discussions on climate modeling. Going back even further, I owe a debt of gratitude to my former research advisors, Tony Clarke at the University of Hawai’i and Daniel Jacob at Harvard, for taking a chance on me as an untested undergraduate and giving me the opportunity to contribute to their research; the field experiment with Tony to measure aerosols on Christmas Island back in 1994 was an inspiring experience! And there are far too many others who have contributed to my intellectual development for me to name them all here.

Outside of academics, countless others have helped me through the graduate school experience. Kristin Larson deserves appreciation without limit for teaching me co-counseling and for her unshakeable support during the past year as we’ve both been working up to graduating. All of my co-counselors have done the important work of showing me that I don’t have to go it alone, and have lightened the burden of distress at many points along the way. Bob Kotchenruther has been a great, supportive roommate and friend as we lived together for five of my seven years of graduate school. More recently, Jessie Minier and Brian Wood have been great housemates and surrogate “parents” in the home that I have made here. My two ultimate teams, Discosity and D’oh!, as well as all the folks I’ve played pickup ultimate with, have provided me with a fun community that I could always turn

to for good times. Fiona Otway has stepped outside of the realm of ultimate to stretch my intellectual boundaries and provide spontaneous diversions, and I've appreciated her supportive friendship during this challenging year. "Yoom" Nguy has been there for me throughout my time in Seattle, as a reliable friend and companion in exploration, and has helped me to push my envelope in many ways. And, as always, there are too many other wonderful people in my life to mention all by name, but many have helped to give me a fun seven years in Seattle, and I appreciate you all!

DEDICATION

To the people of planet Earth.

My knowledge is your knowledge; we're all in this together.

Chapter 1

INTRODUCTION

1.1 What are storm tracks?

Day-to-day weather in the midlatitudes is dominated by the passage of baroclinic waves (e.g., Wallace et al. 1988), the cyclonic phases of which may be thought of as "storms". Regions of particularly large baroclinic wave activity have come to be known as "storm tracks" (Blackmon et al. 1977), although, as these regions are equally populated by cyclones and anticyclones, the term "baroclinic waveguides" might be more appropriate (Wallace et al. 1988). Nevertheless, we will use the term most common in the literature and continue to refer to regions of large baroclinic wave activity as storm tracks.

Storm tracks have typically been identified by maxima in transient eddy statistics, such as the root-mean-square (rms) of 500 mb or 250 mb geopotential height (z), rms of 200 mb meridional wind (v), and 850 mb meridional temperature flux ($v'\theta'$). These statistics may be band-passed to isolate variations on synoptic time scales, usually 2.5–6 days (e.g., Blackmon 1976, Blackmon et al. 1977, Nakamura 1992, Chang 2001), although the specific band-pass filter used is relatively unimportant because transient eddy statistics are dominated by baroclinic waves on synoptic time scales. Fig. 1.1 shows the rms of 250 mb z for 2–10 day transient eddies, based on the NCEP Reanalysis from September 1979 to August 2001, multiplied by the factor [sin(45°)/sin(lat)] as in Nakamura (1992), so that it represents the storm track intensity in terms of a streamfunction-like field. The two most prominent Northern Hemisphere (NH) storm tracks occur over the midlatitude Pacific and Atlantic Oceans, and exhibit more baroclinic wave activity in winter (DJF) than in summer

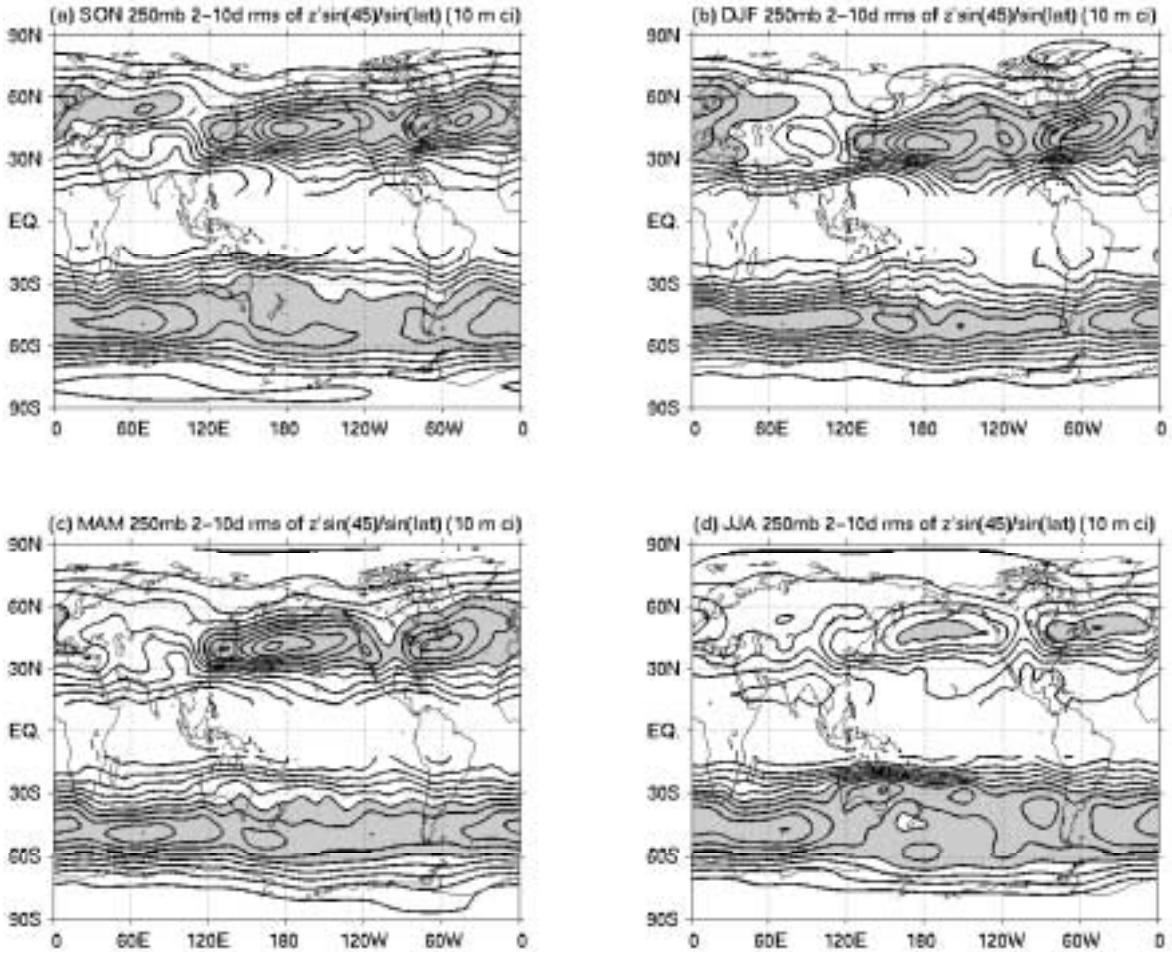

Figure 1.1: Root-mean-square of 250 mb geopotential height, multiplied by the factor sin($45°$)/sin(lat) so that it represents the storm track intensity in terms of a streamfunction-like field, for (a) SON, (b) DJF, (c) MAM, (d) JJA. The contour interval is 10 m; values larger than 80 m are shaded. Values between $10°$S and $10°$N, where the relationship between geopotential height and streamfunction breaks down, have been omitted. Calculations are based on NCEP Reanalysis data from September 1979 to August 2001.

(JJA). However, while the Atlantic storm track reaches its maximum in winter, the Pacific storm track is weaker in winter than in fall (SON) or spring (MAM), and it is this midwinter suppression that we seek to explain in this study. The single Southern Hemisphere (SH) storm track, which extends from the western South Atlantic most of the way around the globe, has a relatively constant intensity throughout the year. The SH storm track is much more zonally symmetric than the NH storm tracks, although it is more zonally symmetric in summer (DJF) than in the other seasons. The greater zonal symmetry of the SH storm track is almost certainly due to the absence of longitudinal variations in topography and land-sea contrasts, factors which strongly influence the NH storm tracks.

In their pioneering study of the NH winter storm tracks, Blackmon et al. (1977) noted that the storm tracks tend to occur on the poleward side of the climatological jets. Fig. 1.2 shows the seasonal variations in 250 mb mean zonal wind (u) which accompany the storm track variations shown in Fig. 1.1. It is apparent that the NH storm tracks do tend to occur slightly poleward and downstream from the localized jets over the Pacific and Atlantic Oceans in all seasons, and both the jets and storm tracks shift equatorward in winter, particularly in the Pacific. This relationship is less clear in the SH, although regions of relatively large 250 mb u do have large variance of 250 mb z associated with them.

In this study, the terms “transient eddies”, “baroclinic waves”, and “storms” will be used interchangeably. This is reasonable because the statistics of- 2-10 day transient eddies that we will examine are dominated by baroclinic waves, or midlatitude storms.

1.2 Why should we care about storm tracks?

The transient eddies in storm tracks play an important role in the general circulation of the atmosphere by transporting large amounts of heat and momentum; they are also responsible for much of what the lay person would consider “weather” in the midlatitudes. Most events of heavy precipitation, strong winds, and rapid temperature changes in the midlatitudes are associated with the synoptic-scale baroclinic waves that dominate the statistics of the storm

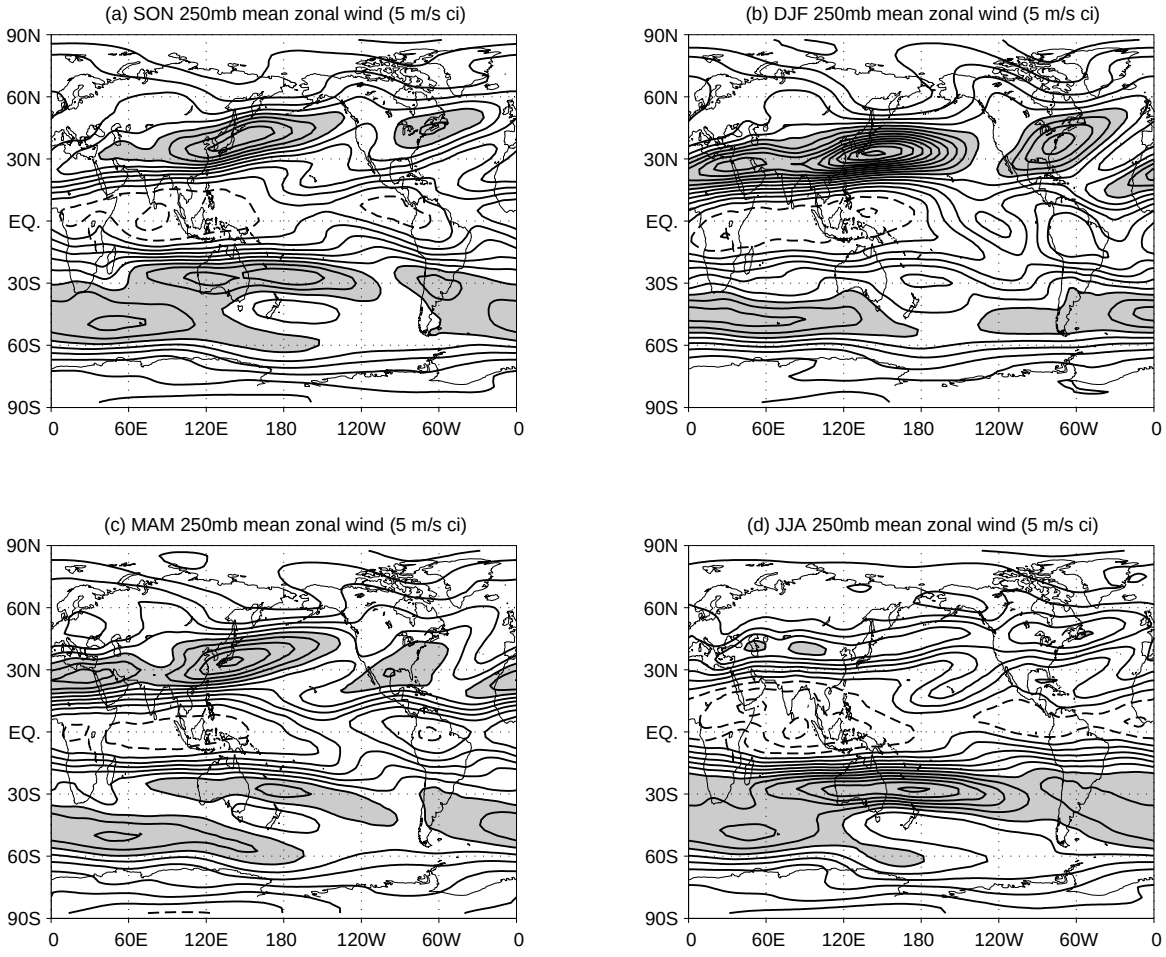

Figure 1.2: 250 mb mean zonal wind for (a) SON, (b) DJF, (c) MAM, (d) JJA. The contour interval is 5 m/s; negative contours are dashed, and values larger than 25 m/s are shaded. Calculations are based on NCEP Reanalysis data from September 1979 to August 2001.

tracks. Finally, changes in the frequency and intensity of these storms have an impact on people's everyday lives.

At present, we do not have a deep enough understanding of the behavior of storm tracks to predict how they will change in a warmer world. A decreasing equator-to-pole temperature gradient as the poles warm more quickly than the tropics implies that the mean baroclinicity of the atmosphere will decrease, reducing the available potential energy on which the baroclinic waves in the storm tracks feed. At the same time, the increasing capacity of the atmosphere to hold moisture implies that the enhancement of baroclinic wave growth by latent heating will increase, which should tend to strengthen the storm tracks. In addition, the mean flow, and in particular the three-dimensional structure of the zonal wind in the jets, appears to organize the transient eddies in ways that are still poorly understood. If we hope to predict how the frequency and intensity of storms will change as the world warms, we should endeavor to better understand how the complex interplay between these factors determines the behavior of the storm tracks.

Fortunately, nature performs an experiment every year in which the baroclinicity, moisture availability, and mean flow are varied, and the resulting seasonal cycle in the storm tracks has some interesting and non-intuitive features. For example, while the NH storm tracks shift equatorward in winter and poleward in summer, the SH storm track remains near the same latitude throughout the year and, if anything, shifts slightly poleward during fall and spring (Trenberth 1991). Perhaps more interestingly, in the NH, the eddy energy in the Atlantic storm track maximizes in winter, when baroclinicity is at a maximum, but the eddy energy in the Pacific storm track maximizes in the fall and spring, with a relative minimum in midwinter during the time of maximum baroclinicity. If we can satisfactorily explain the non-intuitive aspects of the seasonal cycle of the storm tracks, we will be better prepared to predict how the storm tracks will change as increased greenhouse gases warm the Earth.

1.3 What is midwinter suppression?

The midwinter suppression of the Pacific storm track is characterized by an overall decrease and equatorward shift of the maximum in baroclinic wave activity. This decrease in storm track intensity occurs despite the increase in baroclinicity in the Pacific in midwinter. The midwinter decrease in storm track intensity is most pronounced poleward of $40°$N and above 500 mb over the western and central Pacific ($100°$E-$150°$W). We present a more complete description of this phenomenon in Chapter 2.

The midwinter suppression of the Pacific storm track was first noted by Nakamura (1992) in 6-day high-passed transient eddy statistics including the rms of 250 mb z and 850 mb $v'\theta'$. While both measures of storm track intensity are largest during midwinter in the Atlantic, the same measures of Pacific storm track intensity have relative minima spanning January and February flanked by maxima in November and April; the midwinter minimum in the Pacific is more pronounced in the rms of 250 mb z than in 850 mb $v'\theta'$. Nakamura (1992) noted that the midwinter suppression occurs despite the midwinter maximum in low-level baroclinicity (as measured by $Ri^{-\frac{1}{2}}$, where Ri is the Richardson number) in the Pacific. Subsequent studies of the midwinter suppression (Christoph et al. 1997, Zhang 1997, Chang 2001) have confirmed and attempted to explain this non-intuitive result (see section 1.4).

Nakamura (1992) found a negative correlation between baroclinic wave activity and upper-tropospheric jet strength for zonal velocities in excess of 45 m/s, a result that was confirmed by Christoph et al. (1997). Zhang (1997) also found this negative correlation between jet speed and baroclinic wave activity for interannual variations in the Pacific storm track. While this relationship between jet strength and storm track intensity appears to be robust, at least for the Pacific storm track, a satisfactory explanation for this relationship remains to be found.

1.4 Possible mechanisms for the midwinter suppression of the Pacific storm track

Based on the above description of the midwinter suppression, we seek to identify a mechanism (or mechanisms) that accounts for the equatorward shift of the storm track, as well as the decrease in storm track intensity that occurs mostly on the upstream end of the Pacific storm track in the upper troposphere. We have compiled the most plausible of the previously suggested mechanisms for midwinter suppression in the list below. The first five were suggested, in one form or another, by Nakamura (1992), although some have been modified or discounted by subsequent studies. The proposed mechanisms are:

1) The diabatic generation of eddy energy is reduced in midwinter. Nakamura (1992) noted that decreased moisture in midwinter will decrease the latent heating in baroclinic waves and increase the effective static stability, while Chang (2001) added that surface sensible heat fluxes may damp the temperature perturbations in baroclinic waves more effectively in midwinter.

2) The increased jet strength in midwinter may change the structure of baroclinic waves in a way that reduces either their growth rate or their upper-level amplitude. Nakamura (1992) presented evidence that the steering level of baroclinic waves drops in midwinter, and infers from the reduced meridional scale of baroclinic waves that their vertical scale is also reduced in midwinter. Chang (2001), on the other hand, found from regression analysis that baroclinic waves tend to be more trapped at upper levels in midwinter, suggesting that they are less able to tap surface baroclinicity. Christoph et al. (1997) suggested that increased barotropic shear in the stronger midwinter jet may reduce growth rates of baroclinic waves via the "barotropic governor" mechanism of James (1987), which could also explain trapping of waves near upper and lower boundaries. More recently, Nakamura and Sampe (2002) suggested that the strong potential vorticity (PV) gradients in the North Pacific subtropical jet in midwinter may trap propagating baroclinic waves away from the surface baroclinic zone and reduce baroclinic growth in midwinter.

3) The "seeding" of the Pacific storm track by baroclinic waves propagating from

Siberia or the Asian subtropical jet is reduced in midwinter. However, Zhang (1997) performed an empirical orthogonal function analysis of storm track intensity that showed little relationship between baroclinic wave activity over the Pacific and that upstream over Asia, discounting the importance of the seeding mechanism.

4) Excessively strong advection by the strong midwinter jet may cause baroclinic waves to move out of the region of strong baroclinicity in a shorter time so that their spatial growth rate decreases. However, while the phase speed of baroclinic waves increases in midwinter, both Zhang (1997) and Chang (2001) find that the increase in the group velocity of baroclinic wave packets in midwinter is much smaller than the increase in baroclinicity, so the decrease in baroclinic wave activity in midwinter is unlikely to be explained by the rapid propagation of baroclinic wave activity out of the baroclinic region.

5) Baroclinic waves may be dissipated more quickly in midwinter due to excessive diffluence in the exit of the strong jet. Chang (2001) discounted this mechanism because the barotropic conversion term in the eddy energy budget, which is related to the barotropic effects of the jet on eddy energy, actually produces more eddy energy in midwinter than in fall. We also note that the diffluence mechanism would operate in the jet exit region, while the bulk of the midwinter suppression occurs at longitudes where the jet is strongest, so this mechanism is unlikely to explain the observed suppression.

The work of Nakamura (1992), Christoph et al. (1997), and Zhang (1997) has demonstrated a clear negative correlation between the strength of the Pacific storm track and the speed of the Pacific jet, but to date no particular mechanism has been clearly shown to explain this relationship. In this study, we demonstrate that the relationship between the jet and the storm track in the North Pacific can be explained by changes in the tropopause height associated with seasonal variations in the Pacific jet. The mechanism is as follows: The extratropical stationary wave response to the southward shift in tropical convection in midwinter, which strengthens the Pacific jet and shifts it equatorward, also produces downward motion that lowers the tropopause on its poleward flank. This, in turn, produces a large region of increased static stability in the vicinity of the lowered tropopause, which

causes the temperature perturbations in baroclinic waves to be shallower and the associated generation of eddy energy to be less efficient than in fall or spring. As a result, the baroclinic wave activity is reduced above 500 mb on the poleward side of the Pacific jet, which corresponds to the region of maximum midwinter suppression; this explains the observation that baroclinic waves tend to be more localized near the surface and in the subtropical jet. We find that reduced moist heating and the strong advection of temperature perturbations play small supporting roles in causing the suppression, while diffluence is not important.

1.5 Organization of this thesis

In this chapter, we have briefly introduced the subject of storm tracks, described the phenomenon of midwinter suppression in the Pacific storm track, and summarized the possible explanations for this suppression. In the chapters that follow, we will use a number of analysis techniques to examine the differences in the Pacific storm track between November (the fall maximum in storm track intensity), January (the midwinter minimum in storm track intensity), and April (the spring maximum in storm track intensity).

In Chapter 2, we present a four-dimensional description of the midwinter suppression of the Pacific storm track in terms of the total eddy energy for transient eddies with periods of 2–10 days. We illustrate the changes in zonal wind, static stability, and baroclinicity that accompany the midwinter suppression. We also present evidence from observations and GCM experiments that the monthly variations in the Pacific jet and the associated tropopause height are caused by shifts in tropical convection in the western Pacific warm pool.

In Chapter 3, we perform an eddy energy budget analysis (following Orlanski and Katzfey 1991 and Chang 2001) for observed transient eddies with periods of 2–10 days. We determine the changes in the flow of eddy energy that are driving the midwinter suppression of the Pacific storm track, and find that changes in baroclinic wave structure play a large role in the suppression, although the eddy energy budget analysis alone cannot de-

termine the form or cause of these changes in structure.

In Chapter 4, we perform a lag regression analysis (e.g., Lim and Wallace 1991) to determine the differences in observed baroclinic wave structure between November, January, and April. The regression analysis illustrates the causes of the baroclinic wave structure changes that reduce the efficiency of upper level eddy energy generation, demonstrating that the increased static stability due to the lowering of the tropopause is responsible for the bulk of the midwinter suppression.

In Chapter 5, we demonstrate that baroclinic waves tilt poleward with height and show that temperature advection by the ageostrophic wind in baroclinic waves appears to be responsible for their poleward tilt with height. We also extend the results of Lim et al. (1991) and Kwon and Lim (1999) to explain the observed structure of the ageostrophic wind in baroclinic waves. The poleward tilt of baroclinic waves places the maximum upper level storm track intensity on the poleward side of the jet, allowing the lower tropopause poleward of the Pacific jet in midwinter to more effectively suppress the storm track.

Discussion and conclusions are presented in Chapter 6.

Chapter 2

A FOUR-DIMENSIONAL DESCRIPTION OF THE MIDWINTER SUPPRESSION OF THE PACIFIC STORM TRACK

Our efforts to explain the midwinter suppression of the Pacific storm track will proceed more smoothly if we have a detailed picture of the phenomenon that we are attempting to explain. In the literature, storm track intensity has typically been displayed in a meridionally and/or vertically averaged way, or on single pressure levels. In this chapter, we will show monthly maps and vertical cross sections of storm track intensity, upper-level jets, static stability, and baroclinicity in order to provide a four-dimensional description of the midwinter suppression of the Pacific storm track and the accompanying changes in the mean flow.

2.1 Data and analysis techniques

All of the observational analysis in Chapters 2–5 is based on daily mean NCEP/NCAR Reanalysis data from September 1979 to August 2001, which were obtained from the NOAA-CIRES Climate Diagnostics Center website at http://www.cdc.noaa.gov. We choose to use only the data from 1979 onward because the incorporation of satellite data into the NCEP Reanalysis since 1979 has improved the quality of the reanalysis. Transient eddies with periods of approximately 2–10 days are isolated using a "poor man's filter" in which the data are divided into 5-day periods, and eddy quantities are defined as the deviation of the daily means within each 5-day period from the 5-day period mean. We have also redefined each month to be the 6 consecutive 5-day periods which most closely coincide with the actual calendar month; for example, our "November" is Nov 2-Dec 1, "January" is Jan 1-Jan 30,

and “April” is Apr 1-Apr 30. We confirm that each feature pointed out in this study is seen in the first half (1979-1990) and last half (1990-2001) of the data.

2.2 Storm track intensity in terms of eddy energy

We define two types of eddy energy, eddy kinetic energy (KE):

$$K = \frac{1}{2}(u'^2 + v'^2) \tag{2.1}$$

and eddy available potential energy (APE):

$$P = \frac{1}{2}\frac{s^2}{(\Theta_p)^2}\theta'^2 \tag{2.2}$$

where

$$s^2(p) = -\frac{R}{p}\left(\frac{p}{p_0}\right)^{\frac{R}{c_p}}\Theta_p \tag{2.3}$$

is a stability parameter and $\Theta_p(p)$ is the pressure derivative of the basic state potential temperature profile, both of which are appropriate for a standard atmosphere (Holton 1992, Appendix E) and functions of pressure only. The primed variables u', v', and θ' represent departures from 5-day means of zonal wind, meridional wind, and potential temperature, respectively. We note that the magnitude of the eddy APE is somewhat arbitrary, because it depends on the vertical potential temperature gradient of the basic state, which we have chosen to be the Holton (1992) standard atmosphere. This time- and space-invariant basic state was chosen so that the eddy APE can be compared between different months and regions, since it will always be proportional to θ'^2.

The eddy total energy (TE) is simply the sum of eddy KE and eddy APE:

$$TE = K + P \tag{2.4}$$

In this study, we shall use eddy TE averaged between 100 mb and 500 mb as a measure of upper-level storm track intensity. Fig. 2.1 shows the seasonal variations of eddy TE averaged between 100 mb and 500 mb. The seasonal variations of the Pacific, Atlantic, and

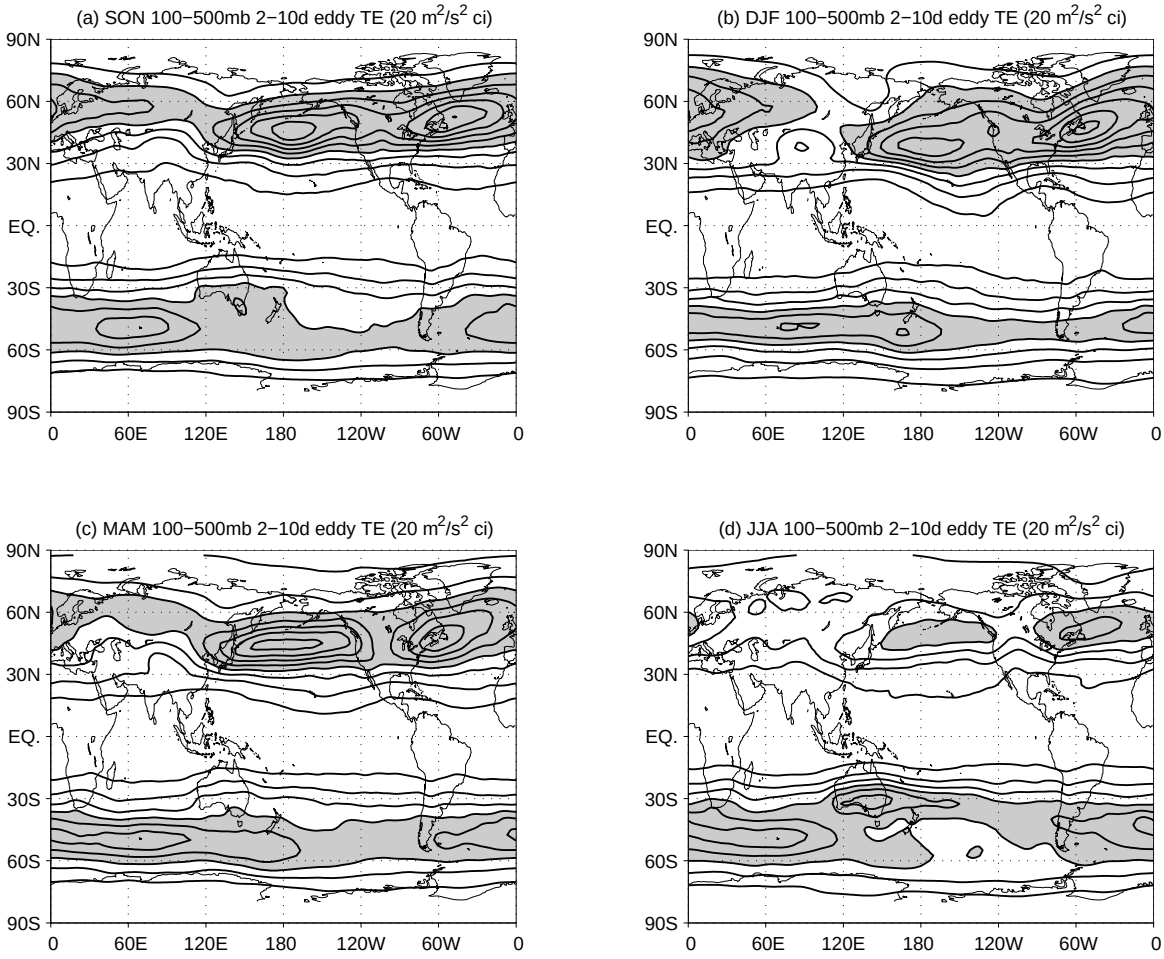

Figure 2.1: Mass-weighted average of eddy TE between 100 mb and 500 mb, for (a) SON, (b) DJF, (c) MAM, (d) JJA. The contour interval is 20 m^2/s^2; values greater than 80 m^2/s^2 are shaded. Calculations are based on NCEP Reanalysis data from September 1979 to August 2001.

SH storm tracks as measured by 100-500 mb eddy TE are similar to those shown in Fig. 1.1 by the rms of 250 mb z, but with a slight poleward shift of the storm tracks; an increase in the intensity of the Atlantic storm track relative to the Pacific storm track, particularly in NH winter (DJF); and a slight downstream shift of the SH storm track in all seasons. These differences reflect the greater response of eddy TE to v'^2, which tends to increase relative to u'^2 towards the downstream end of the storm tracks. We prefer to use eddy TE, rather than the variance of a single dynamical variable, as a measure of storm track intensity because the eddy TE budget can be easily calculated (following Orlanski and Katzfey 1991 and Chang 2001) to better understand the causes of the seasonal variations of the storm tracks. The eddy energy budget will be examined in Chapter 3.

To illustrate the midwinter suppression of the Pacific storm track with finer temporal resolution, we show in Fig. 2.2 the monthly variations of 100-500 mb eddy TE from October to May in the NH midlatitudes. We see that the maximum in Pacific storm track intensity shifts equatorward from October (near $45°$N) to January (between $35°$N and $40°$N), and at the same time decreases in maximum intensity by approximately 20%. Over the same period, the Atlantic storm track shifts slightly equatorward (from $50°$N to $45°$N) but keeps approximately the same maximum intensity. The seasonal trends in both storm tracks reverse between February and April as the spring storm tracks resemble those in fall, although in spring both storm tracks are slightly farther west and the Atlantic storm track is weaker. Although the local maximum in Pacific storm track intensity is largest in October, the storm track spans a wider latitudinal range in November; we shall choose November to represent the fall maximum in Pacific storm track intensity because 100 mb-500 mb eddy TE is larger in November than in Octover when averaged across the storm track from $20°$N to $70°$N. The Pacific storm track intensity is very similar in January and February, but we shall choose January to represent of the midwinter minimum because, when averaged across the Pacific storm track from $20°$N to $70°$N and from $100°$E to $120°$W, eddy TE is slightly less in January than in February. The Pacific storm track intensity is clearly larger in April than in March or May, so we choose April to represent the spring maximum. Thus,

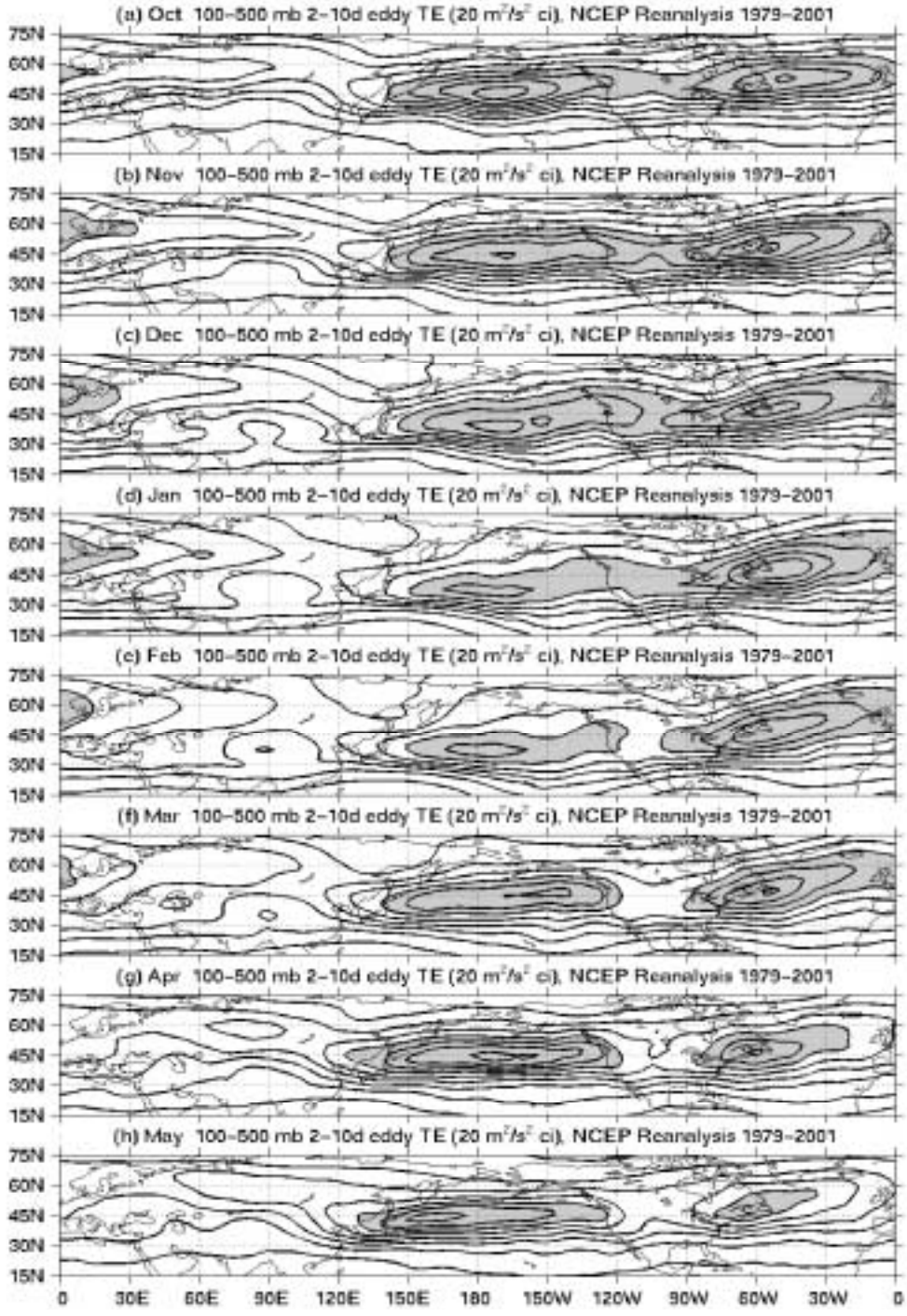

Figure 2.2: Mass-weighted average of eddy TE between 100 mb and 500 mb, for (a) October, (b) November, (c) December, (d) January, (e) February, (f) March, (g) April, (h) May. The contour interval is 20 m^2/s^2; values greater than 120 m^2/s^2 are shaded. Calculations are based on NCEP Reanalysis data from September 1979 to August 2001.

the January − November difference will represent the midwinter suppression relative to fall, and the January − April difference will represent the midwinter suppression relative to spring.

Fig. 2.3 shows eddy TE averaged from $20°$N to $70°$N and 100 mb to 500 mb as a function of longitude for November, January, and April. This latitudinal range spans the regions of largest mean TE in Fig. 2.2 and is consistent with the latitudinal averaging of Chang (2001), whose Fig. 10a is similar, but for eddy KE only averaged between 100 mb and 1000 mb. Eddy TE is larger in April than in November west of $170°$E, indicating the shift of the Pacific storm track towards Asia in spring relative to fall. Between $100°$E and $150°$W, the mass-weighted average of 100 mb-500 mb eddy TE decreases by 9% from November (87.6 m^2/s^2) to January (79.6 m^2/s^2); between $90°$E and $170°$W, this quantity increases by 13% from January (72.1 m^2/s^2) to April (82.4 m^2/s^2). The midwinter suppression in Fig. 2.3 is clearer than that shown in Chang (2001) for two reasons: (1) we compare January with November and April, rather than October; and (2) we focus on synoptic-scale transient eddies, which bear the bulk of the suppression, while Chang (2001) includes eddies on all submonthly time scales. Fig. 2.3 also shows that the Atlantic storm track is stronger in January than in November or April, and in fact it is stronger than in any other month.

The spatial pattern of the midwinter suppression is shown in the top and bottom panels of Fig. 2.4. As in the figures to follow, the middle three panels show maps for November, January, and April, while the top panel shows the January − November difference and the bottom panel shows the January − April difference. The equatorward shift of the storm track from November to January is obvious at all longitudes, but the overall decrease in storm track intensity occurs only over the Pacific. Storm track intensity is considerably larger in January than in April except over eastern Asia and the western Pacific, where it is considerably smaller. Although the differences in Figs. 2.4a and e suggest that the suppression is centered between $45°$N and $50°$N, it is probably more useful to think of a suppression centered farther equatorward that is superimposed on an equatorward shift of

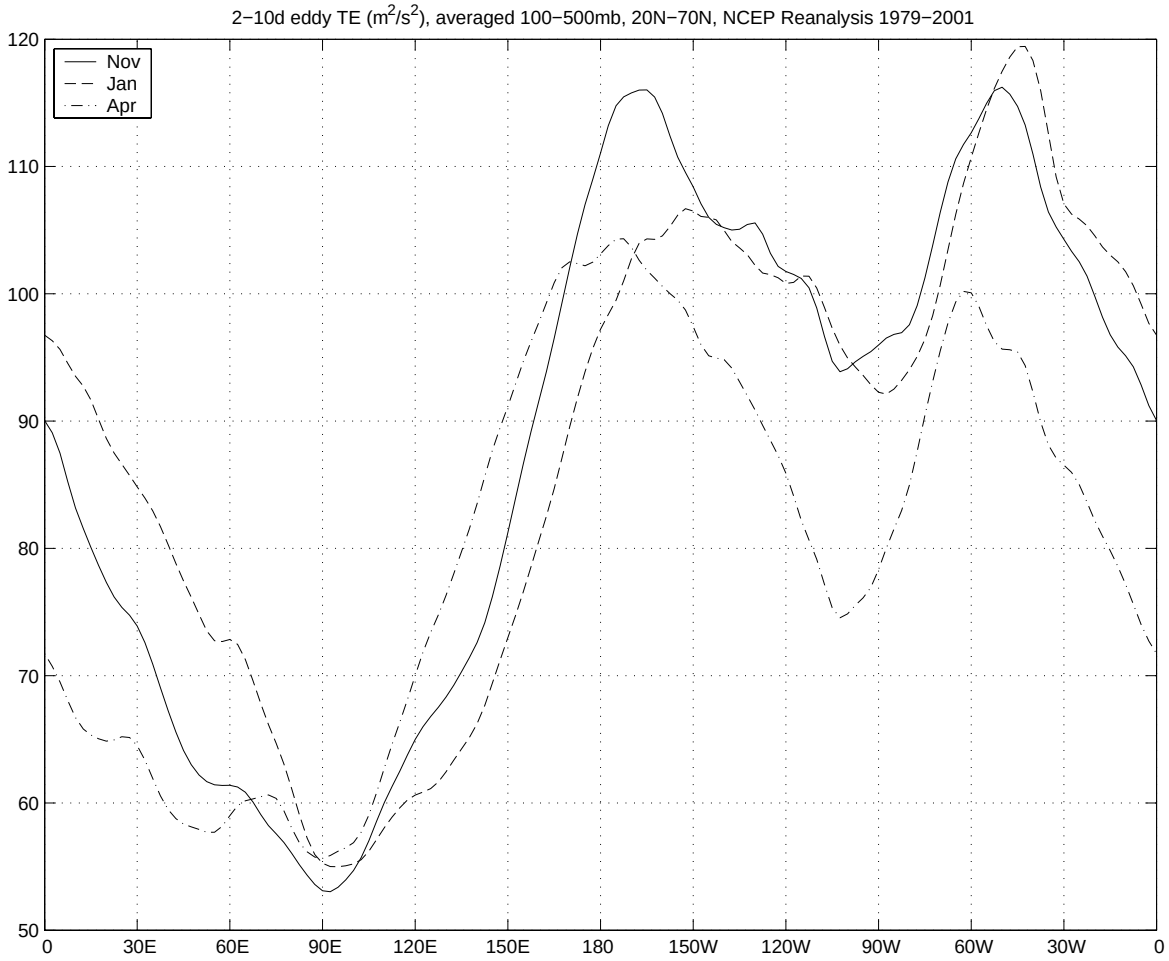

Figure 2.3: Mass-weighted average of eddy TE from 100 mb to 500 mb and from $20°$N to $70°$N, as a function of longitude, for November (solid), January (dashed), and April (dashed-dotted). Calculations are based on NCEP Reanalysis data from September 1979 to August 2001.

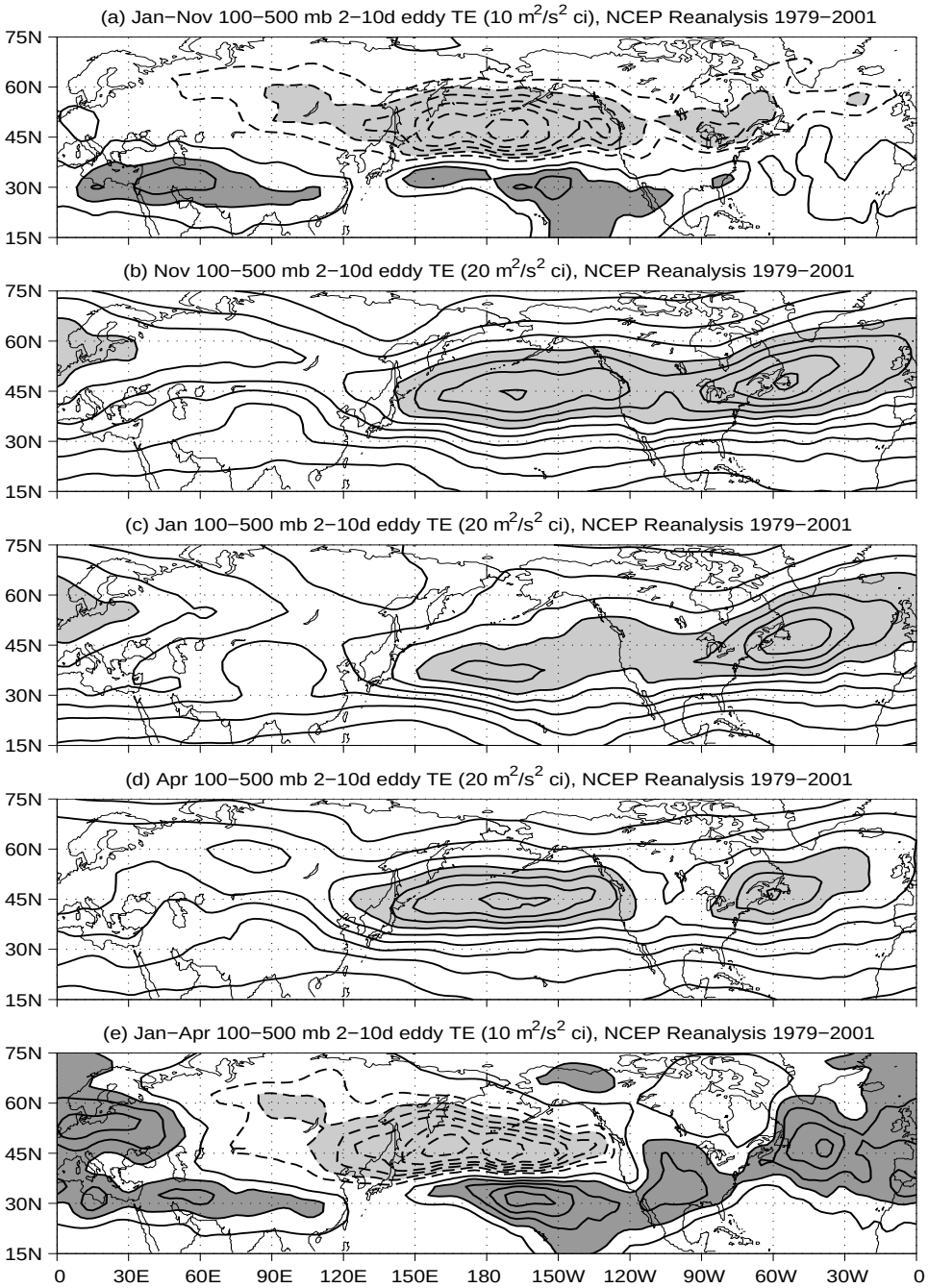

Figure 2.4: Mass-weighted average of eddy TE between 100 mb and 500 mb, for (a) January−November, (b) November, (c) January, (d) April, (e) January−April. In panels (a) and (e), the contour interval is 10 m^2/s^2, with dashed negative contours and the zero contour omitted; light shading indicates values less than -20 m^2/s^2, and dark shading indicates values greater than 20 m^2/s^2. In panels (b)–(d), the contour interval is 20 m^2/s^2; shading indicates values greater than 120 m^2/s^2. Calculations are based on NCEP Reanalysis data from September 1979 to August 2001.

the storm track in midwinter.

To complete the four-dimensional illustration of the midwinter suppression of the Pacific storm track, in Fig. 2.5 we show longitude-pressure cross sections of eddy TE averaged between $20°$N and $70°$N. Focusing on the Pacific sector, from $120°$E to $120°$W, it is clear that the vast majority of the suppression occurs at upper levels, as noted by Nakamura (1992), which justifies our focus on 100-500 mb storm track intensity. Relative to both November and April, there is also less eddy TE near the surface over eastern Asia in January.

To illustrate the structure of the different forms of eddy TE, Fig. 2.6 shows longitude-pressure cross sections of eddy KE, while Fig. 2.7 shows longitude-pressure cross sections of eddy APE. Eddy KE reaches its largest magnitude at upper levels, away from the damping by friction at the surface, while eddy APE is largest near the surface, especially over land where it is damped less quickly by surface sensible heat fluxes than over the ocean, and in the middle troposphere. Eddy KE also tends to be larger in magnitude than eddy APE (note the difference in contour intervals between Fig. 2.6 and Fig. 2.7) . The difference plots show that the suppression of the Pacific storm track at upper levels is dominated by the decrease in eddy KE, while the smaller reduction in eddy TE near the surface over eastern Asia occurs almost exclusively in eddy APE. We argue in the eddy energy budget analysis of Chapter 3 that this low-level reduction in eddy APE over eastern Asia is unlikely to be related to the upper-level reduction in eddy KE over the Pacific.

2.3 Variations in the jets

Much of the previous work on midwinter suppression has focused on the inverse relationship between the strength of the Pacific jet and the intensity of the Pacific storm track (Nakamura 1992, Christoph et al. 1997, Zhang 1997). However, because the structure of the upper-level jets affects both the static stability (see section 2.4) and the baroclinicity (see section 2.5), it is instructive to look beyond just the jet speed and examine the four-

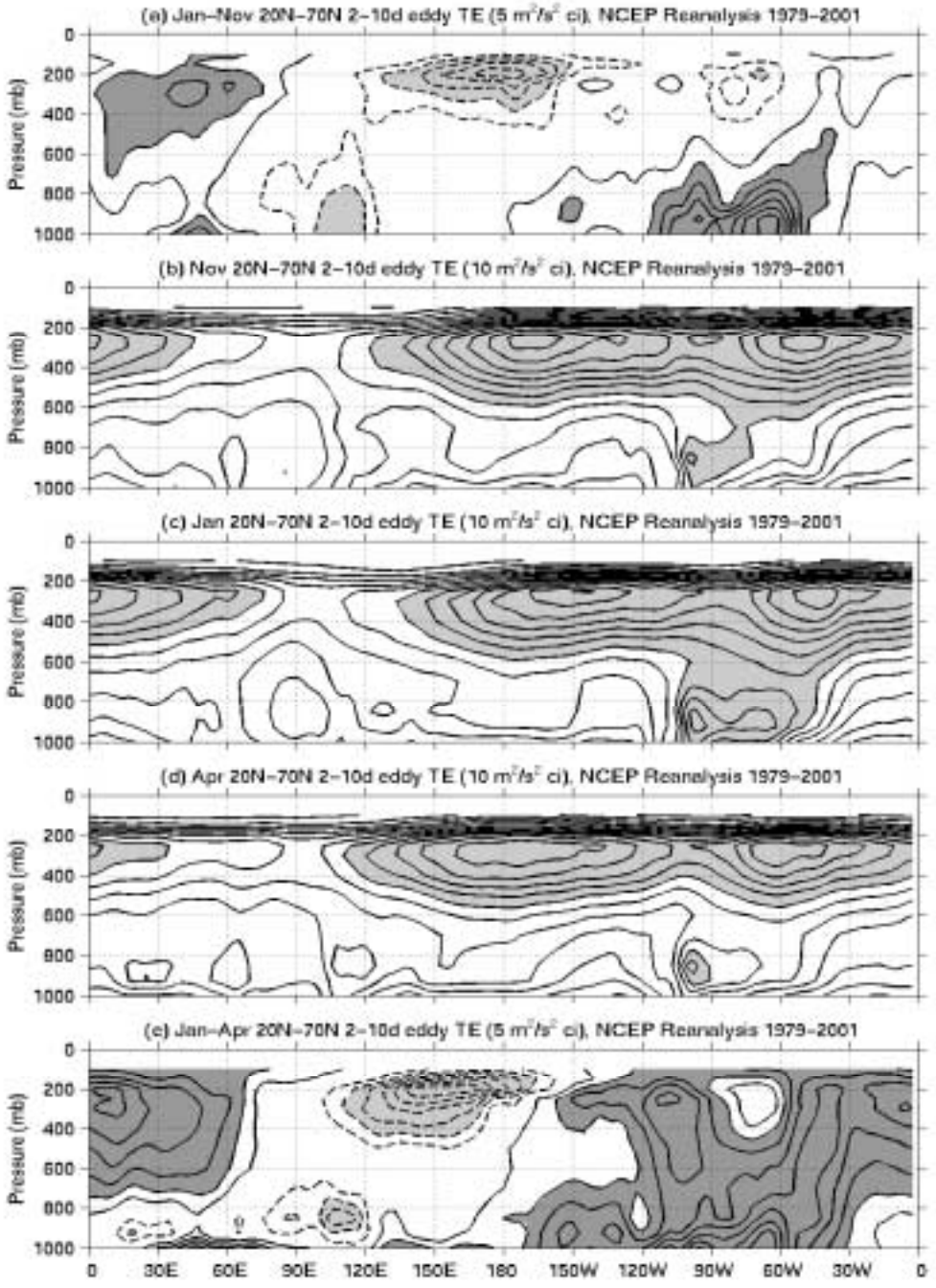

Figure 2.5: Mass-weighted average of eddy TE between $20°$N and $70°$N, for (a) January−November, (b) November, (c) January, (d) April, (e) January−April. In panels (a) and (e), the contour interval is 5 m^2/s^2, with dashed negative contours and the zero contour omitted; light shading indicates values less than -10 m^2/s^2, and dark shading indicates values greater than 10 m^2/s^2. In panels (b)–(d), the contour interval is 10 m^2/s^2; shading indicates values greater than 80 m^2/s^2. Calculations are based on NCEP Reanalysis data from September 1979 to August 2001.

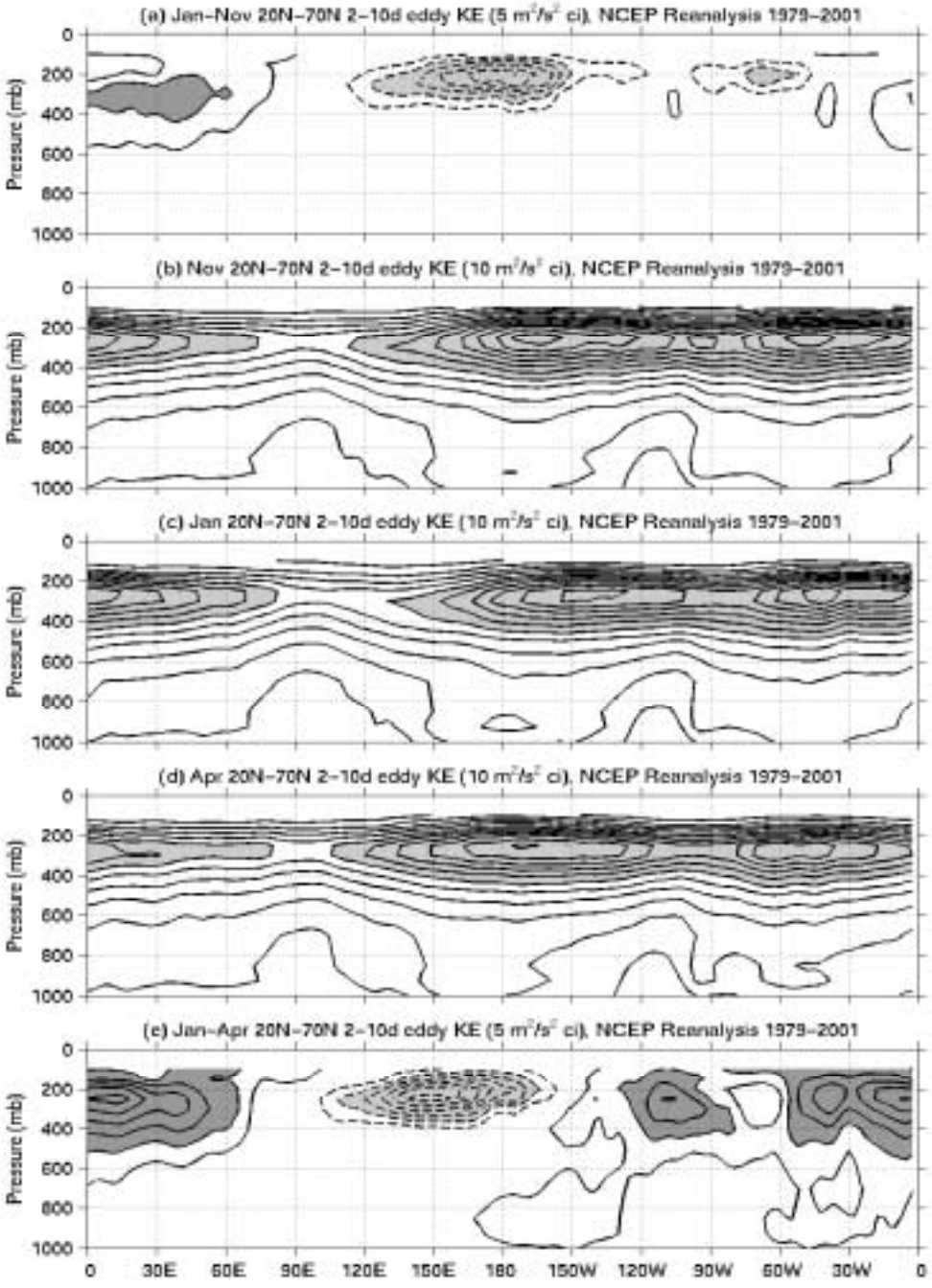

Figure 2.6: Mass-weighted average of eddy KE between $20°$N and $70°$N, for (a) January$-$November, (b) November, (c) January, (d) April, (e) January$-$April. In panels (a) and (e), the contour interval is 5 m^2/s^2, with dashed negative contours and the zero contour omitted; light shading indicates values less than -10 m^2/s^2, and dark shading indicates values greater than 10 m^2/s^2. In panels (b)–(d), the contour interval is 10 m^2/s^2; shading indicates values greater than 60 m^2/s^2. Calculations are based on NCEP Reanalysis data from September 1979 to August 2001.

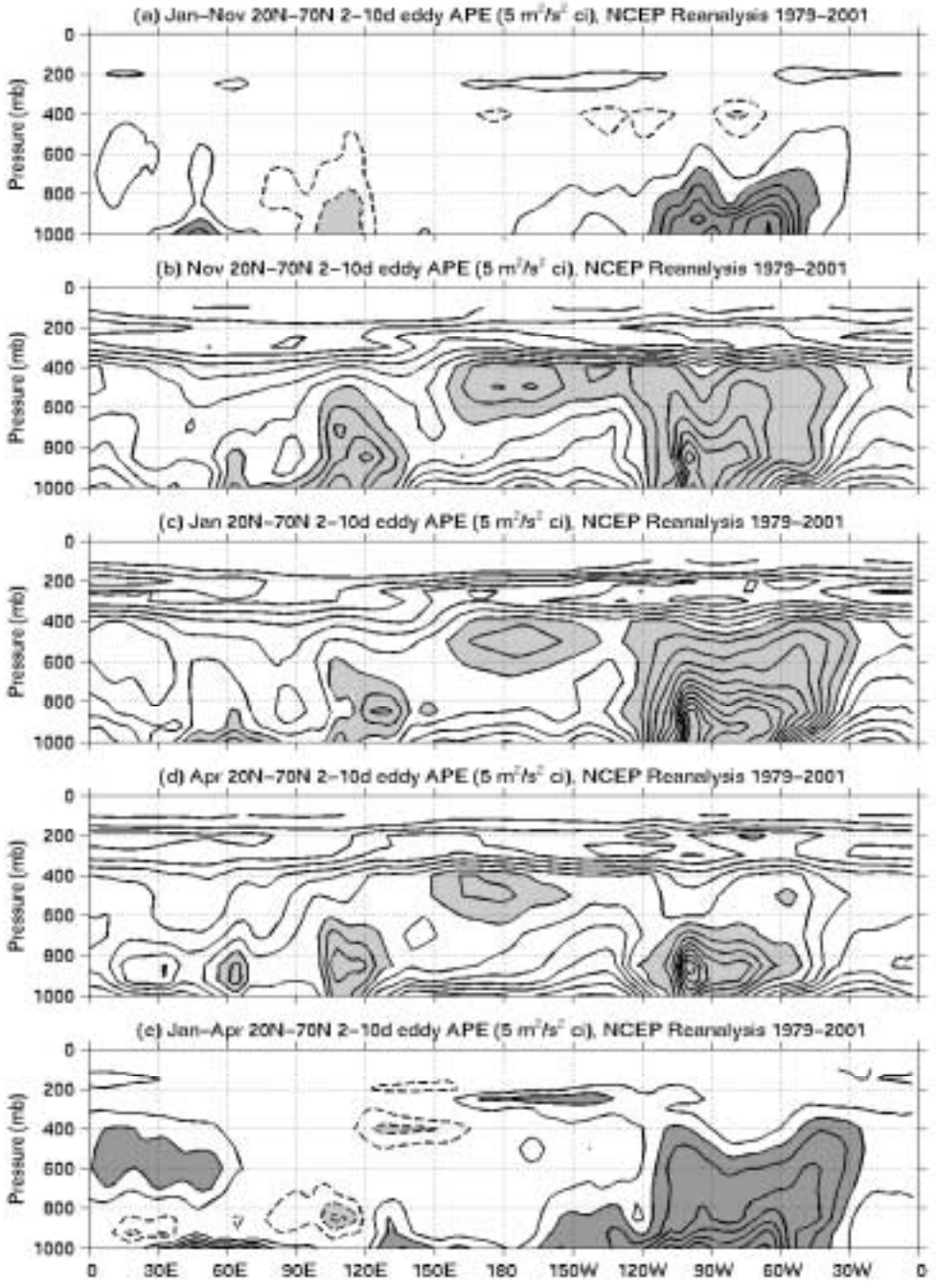

Figure 2.7: Mass-weighted average of eddy APE between $20°$N and $70°$N, for (a) January$-$November, (b) November, (c) January, (d) April, (e) January$-$April. In panels (a) and (e), the contour interval is 5 m^2/s^2, with dashed negative contours and the zero contour omitted; light shading indicates values less than -10 m^2/s^2, and dark shading indicates values greater than 10 m^2/s^2. In panels (b)–(d), the contour interval is 5 m^2/s^2; shading indicates values greater than 40 m^2/s^2. Calculations are based on NCEP Reanalysis data from September 1979 to August 2001.

dimensional evolution of the Pacific jet through the winter.

Fig. 2.8 shows the longitude-pressure cross sections of u that accompany the midwinter suppression of the Pacific storm track, averaged between $20°$N and $70°$N. The difference plots show that both the Pacific and the Atlantic jets get stronger and shift downstream in January relative to November and March. The increase is greatest at upper levels, but extends down to the surface as well.

More instructive is Fig. 2.9, which shows maps of u averaged from 100 mb to 300 mb, where u is largest. The difference plots show that the Pacific jet has a much larger tendency than the Atlantic jet to shift equatorward as it strengthens in January relative to November and April. The Pacific jet is also narrower in January than in November or April, and upper level u is weaker north of the jet in January than in November and, to a lesser extent, April. Comparing Fig. 2.9 to Fig. 2.4, the Pacific storm track has strengthened at latitudes where the Pacific jet is stronger in January, and weakened at latitudes where the jet is weaker, suggesting that more rapid advection out of the baroclinic region is unlikely to be the cause of the observed midwinter suppression.

It is reasonable to ask why the Pacific jet narrows as it strengthens in midwinter. We present two pieces of evidence that the narrowing of the Pacific jet is part of the stationary wave response to the southward shift and strengthening of tropical convection in the western Pacific warm pool region. First, Fig. 2.10 shows the 100-300 mb stationary eddy z field (i.e., with the zonal mean removed) in contours for November, January, and April, with regions of precipitation greater than 8 mm/day shown in thick contours; z is calculated from the NCEP Reanalysis, while the precipitation is taken from the 1979-2000 climatology of the Global Precipitation Climatology Project. As the maximum in tropical convection shifts to the south of the equator and strengthens in midwinter, the stationary wave response over the North Pacific grows larger. The strengthening low over northern Japan not only increases the strength of the Pacific jet, but also decreases the zonal winds to the north of the jet, producing a jet which is stronger and narrower in January than in November or April. The lack of a corresponding change in the Atlantic is probably due to the smaller

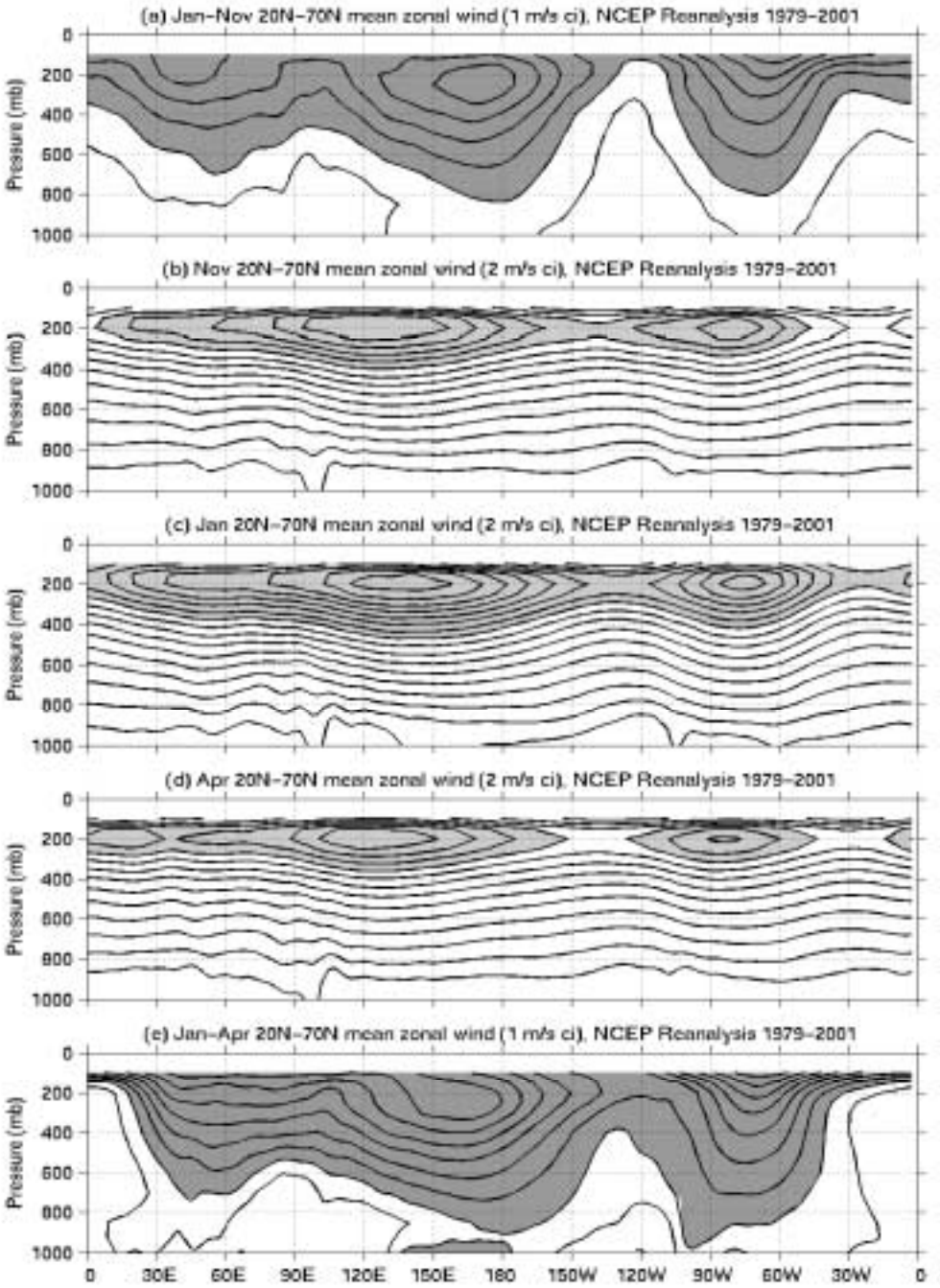

Figure 2.8: Mass-weighted average of mean zonal wind between $20°$N and $70°$N, for (a) January−November, (b) November, (c) January, (d) April, (e) January−April. In panels (a) and (e), the contour interval is 1 m/s, with dashed negative contours and the zero contour omitted; dark shading indicates values greater than 2 m/s. In panels (b)–(d), the contour interval is 2 m/s; shading indicates values greater than 20 m/s. Calculations are based on NCEP Reanalysis data from September 1979 to August 2001.

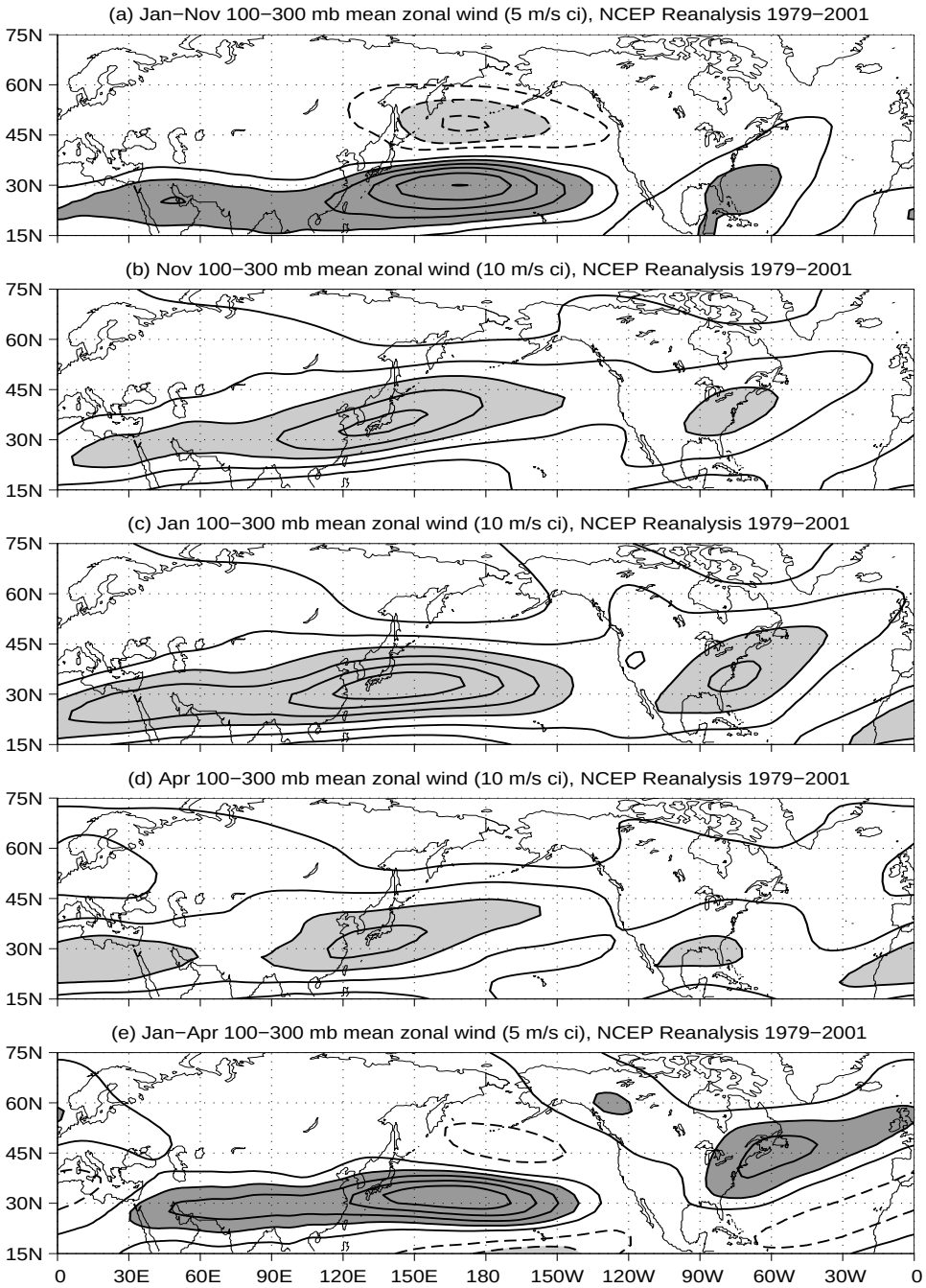

Figure 2.9: Mass-weighted average of mean zonal wind between 100 mb and 300 mb, for (a) January−November, (b) November, (c) January, (d) April, (e) January−April. In panels (a) and (e), the contour interval is 5 m/s, with dashed negative contours and the zero contour omitted; light shading indicates values less than -10 m/s, and dark shading indicates values greater than 10 m/s. In panels (b)–(d), the contour interval is 10 m/s; shading indicates values greater than 30 m/s. Calculations are based on NCEP Reanalysis data from September 1979 to August 2001.

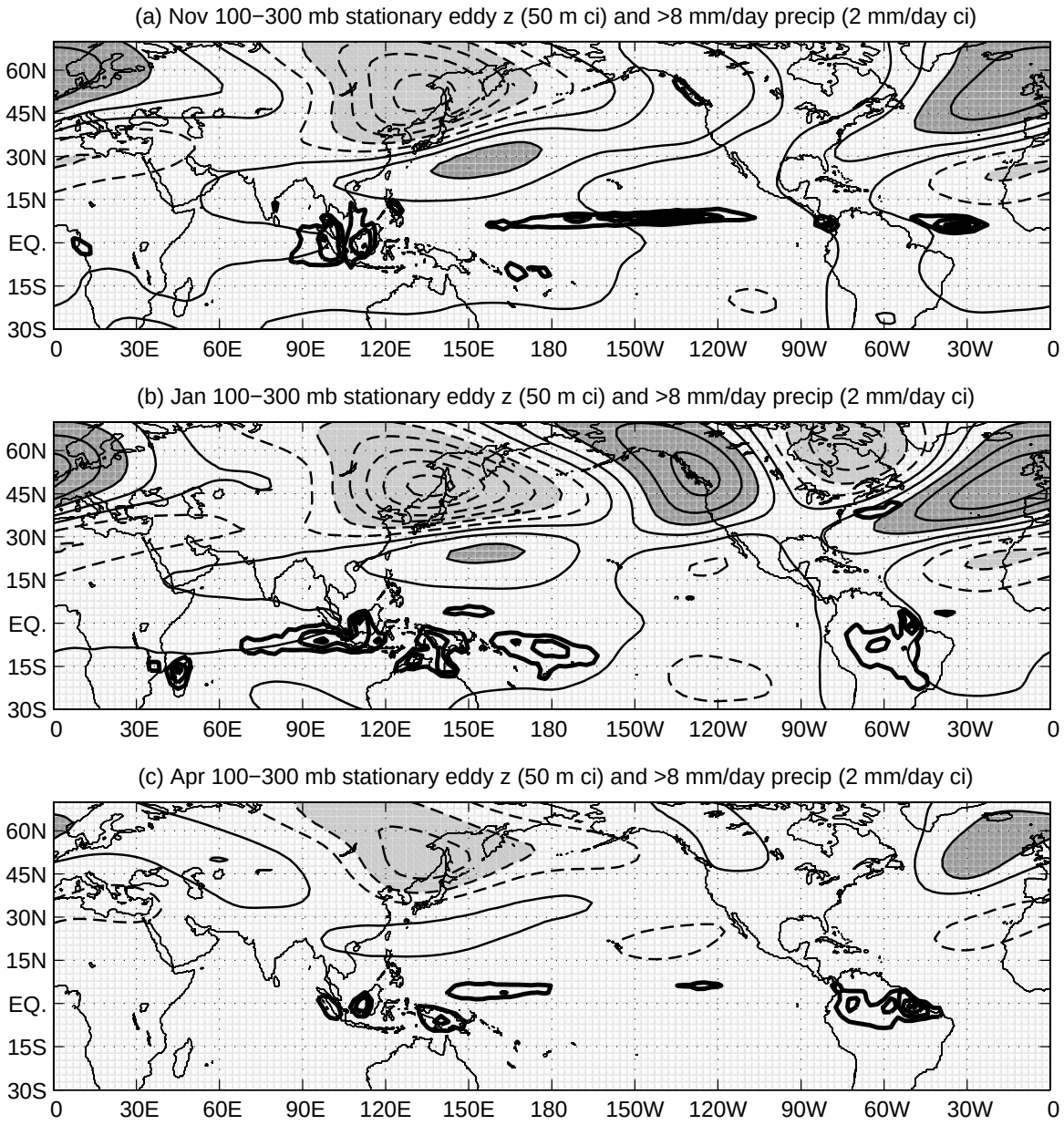

Figure 2.10: Deviations of geopotential height from its zonal mean (thin contours with interval 50 m; light shading indicates values less than -100 m, and dark shading indicates values greater than 100 m), and precipitation (thick contours with interval 2 mm/day for values 8 mm/day or greater) for (a) November, (b) January, (c) April. Geopotential height is calculated from NCEP Reanalysis data for September 1979-August 2001, while precipitation is calculated from the Global Precipitation Climatology Project monthly data for January 1979-December 2000.

changes in tropical convection in the Atlantic sector in midwinter, which allow the Atlantic jet to remain more eddy-driven than subtropical. It is also possible that the changes in the Pacific jet are enhanced by interactions between the jet and the stationary wave forced by the Tibetan Plateau (Nigam and Lindzen 1989).

A more causal link between tropical convection and the strengthening and narrowing of the Pacific jet can be drawn from two perpetual January GCM experiments that we performed with the NCAR Community Climate Model version 3.6 (CCM3.6, Kiehl et al. 1996) at T31x15 resolution (approximately 3.75° latitude by 7.5° longitude). The first experiment, ASIA HIMALAYAS, had as its boundary conditions an aquaplanet surface with prescribed zonally symmetric sea surface temperatures appropriate for January, to which a flat continent with the shape of Asia and a mountain with the elevation of Tibet were added. The 100-300 mb u and tropical precipitation for this experiment are shown in Fig. 2.11a; the Pacific jet is similar in shape to that observed for November (see Fig. 2.9b), relatively broad and tilted northeast-southwest over Japan, with a maximum speed of 63 m/s. The second experiment, ASIA HIMALAYAS WARMPOOL, had exactly the same boundary conditions but with the SSTs from 16.7°S to 16.7°N and from 120°E to the dateline set to values appropriate for the Pacific warm pool in January. This had the effect of adding a strong convective region in the warm pool south of the equator (near 15°S, 120°E), whereas nearly all of the strong convection in experiment ASIA HIMALAYAS was north of the equator. The 100-300 mb u and tropical convection for ASIA HIMALAYAS WARMPOOL are shown in Fig. 2.11b; the Pacific jet is now more similar in shape to that observed for January (see Fig. 2.9c), narrower and more zonally oriented than the jet in experiment ASIA HIMALAYAS, with a stronger maximum speed of 76 m/s. The strengthening and narrowing of the Pacific jet in ASIA HIMALAYAS WARMPOOL relative to that in ASIA HIMALAYAS is almost certainly part of the stationary wave response to the strengthening of convection south of the equator in this sector; the change in the jet could also be viewed as the result of a stronger local Hadley cell with flow into the NH at upper levels.

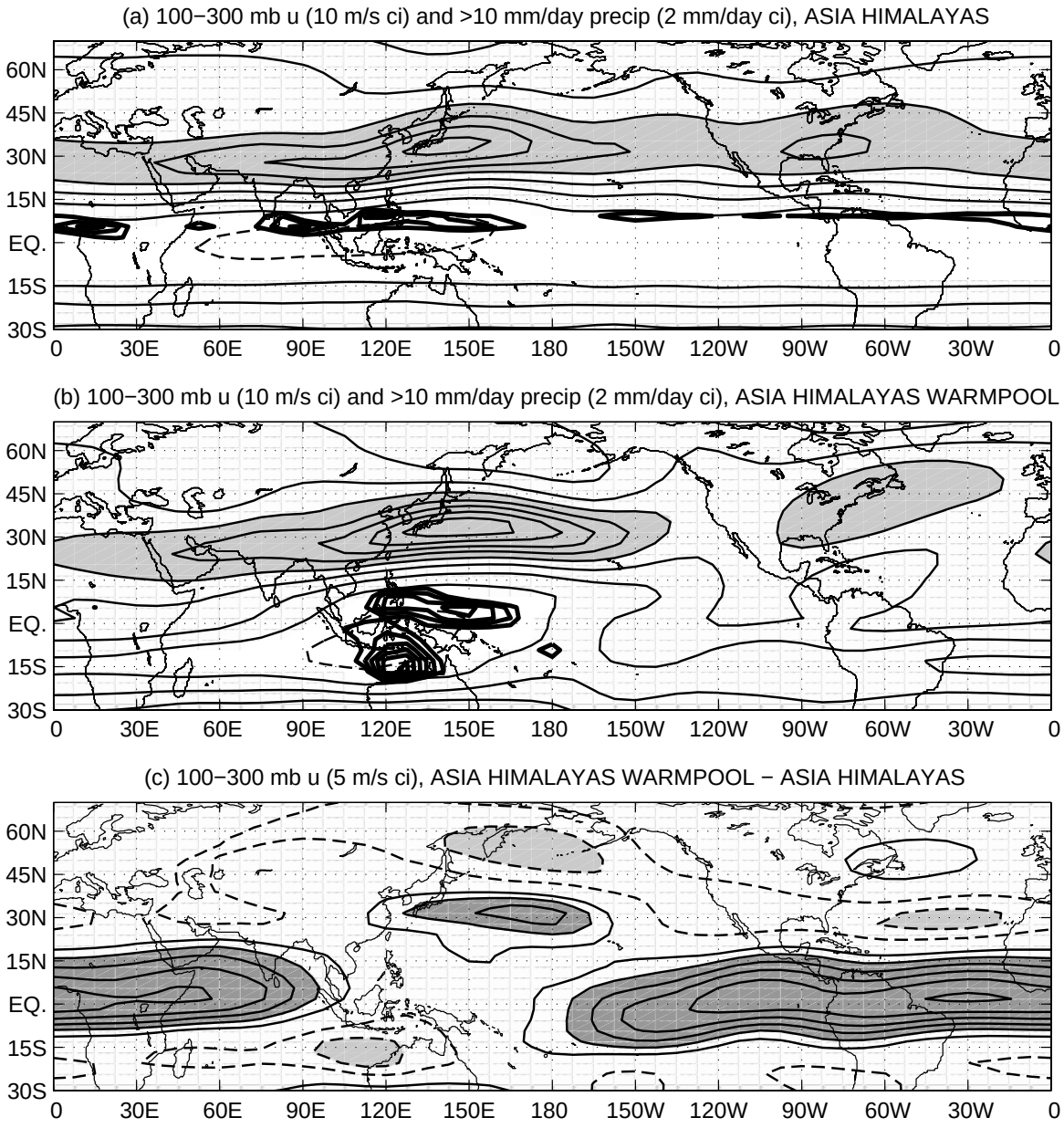

Figure 2.11: Mean zonal wind (thin contours with interval 10 m/s; shading indicates values larger than 30 m/s) and precipitation (thick contours with interval 2 mm/day for values 10 mm/day or greater) for two perpetual January CCM3.6 experiments (see text for details): (a) ASIA HIMALAYAS, (b) ASIA HIMALAYAS WARMPOOL. Panel (c) shows the ASIA HIMALAYAS WARMPOOL−ASIA HIMALAYAS difference in mean zonal wind, with a 5 m/s contour interval; light shading indicates values less than -10 m/s, and dark shading indicates values greater than 10 m/s. Quantities are averaged over the last 1440 days of each 1800-day experiment.

2.4 Static stability

The static stability of the atmosphere is important in the production of eddy energy, because lower static stability allows eddy APE to be converted more efficiently into eddy KE (see Chapter 3) and permits deeper temperature perturbations in baroclinic waves (see Chapter 4). A convenient measure of static stability is the Brunt-Väisälä frequency, N, defined such that:

$$N^2 = \frac{g}{\theta}\frac{\partial \theta}{\partial z} \tag{2.5}$$

where g is the gravitational acceleration and θ is the mean state potential temperature.

Fig. 2.12 shows longitude-pressure cross sections of N averaged from 20°N to 70°N. In general, N is large near the surface over the continents in winter, where the surface cooling produces strong stability; small over the western oceans, where cold continental air blows over the relatively warm ocean surface and produces weak stability; and large above the tropopause in the stably stratified stratosphere. The January $-$ April difference is dominated by enhancement of the strong continental stability/weak oceanic stability pattern near the surface in January, while the January $-$ November difference also has this pattern but with a much smaller magnitude. January also has relatively high static stability between 200 mb and 400 mb, particularly over the western Pacific, and more so relative to April than November; this suggests that there is a lower tropopause in January over the western Pacific.

The spatial pattern of near-surface N, averaged from 700 mb to 1000 mb, is shown in Fig. 2.13. The large near-surface static stability over continents and low near-surface static stability over oceans is evident. Static stability increases from November to January in regions of expanded sea ice, while the January $-$ April difference is primarily due to the greater land-sea contrast in January.

The spatial pattern of tropopause-level N, averaged from 200 mb to 400 mb, is shown in Fig. 2.14. Comparing Fig. 2.14 to Fig. 2.9, strong meridional gradients in 200-400 mb N appear to occur near or just poleward of the Pacific and Atlantic jets; the unusually

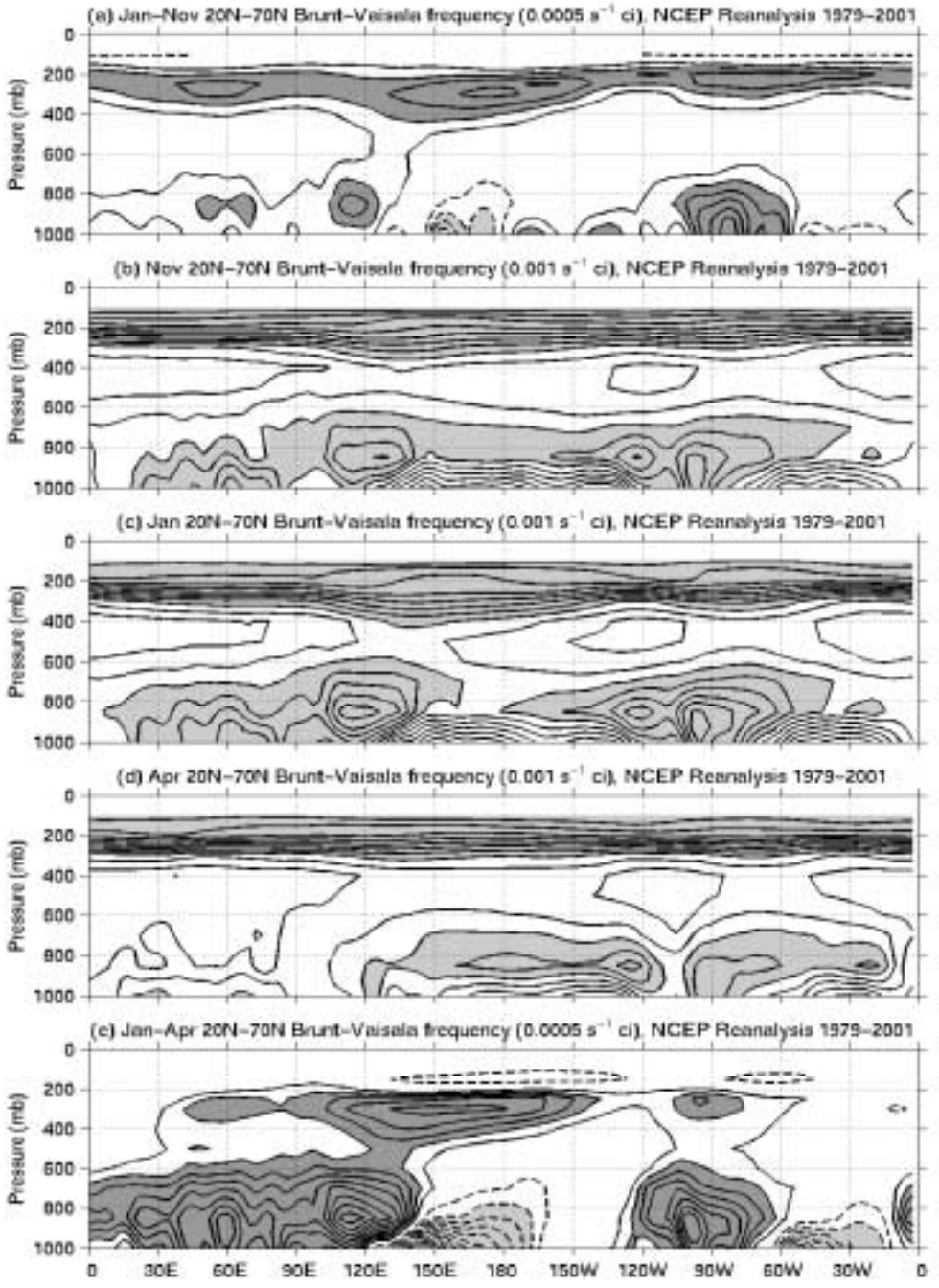

Figure 2.12: Mass-weighted average of the Brunt-Väisälä frequency between $20°$N and $70°$N, for (a) January−November, (b) November, (c) January, (d) April, (e) January−April. In panels (a) and (e), the contour interval is 0.0005 s^{-1}, with dashed negative contours and the zero contour omittedl; light shading indicates values less than -0.001 s^{-1}, and dark shading indicates values greater than 0.001 s^{-1}. In panels (b)–(d), the contour interval is 0.001 s^{-1}; shading indicates values greater than 0.013 s^{-1}. Calculations are based on NCEP Reanalysis data from September 1979 to August 2001.

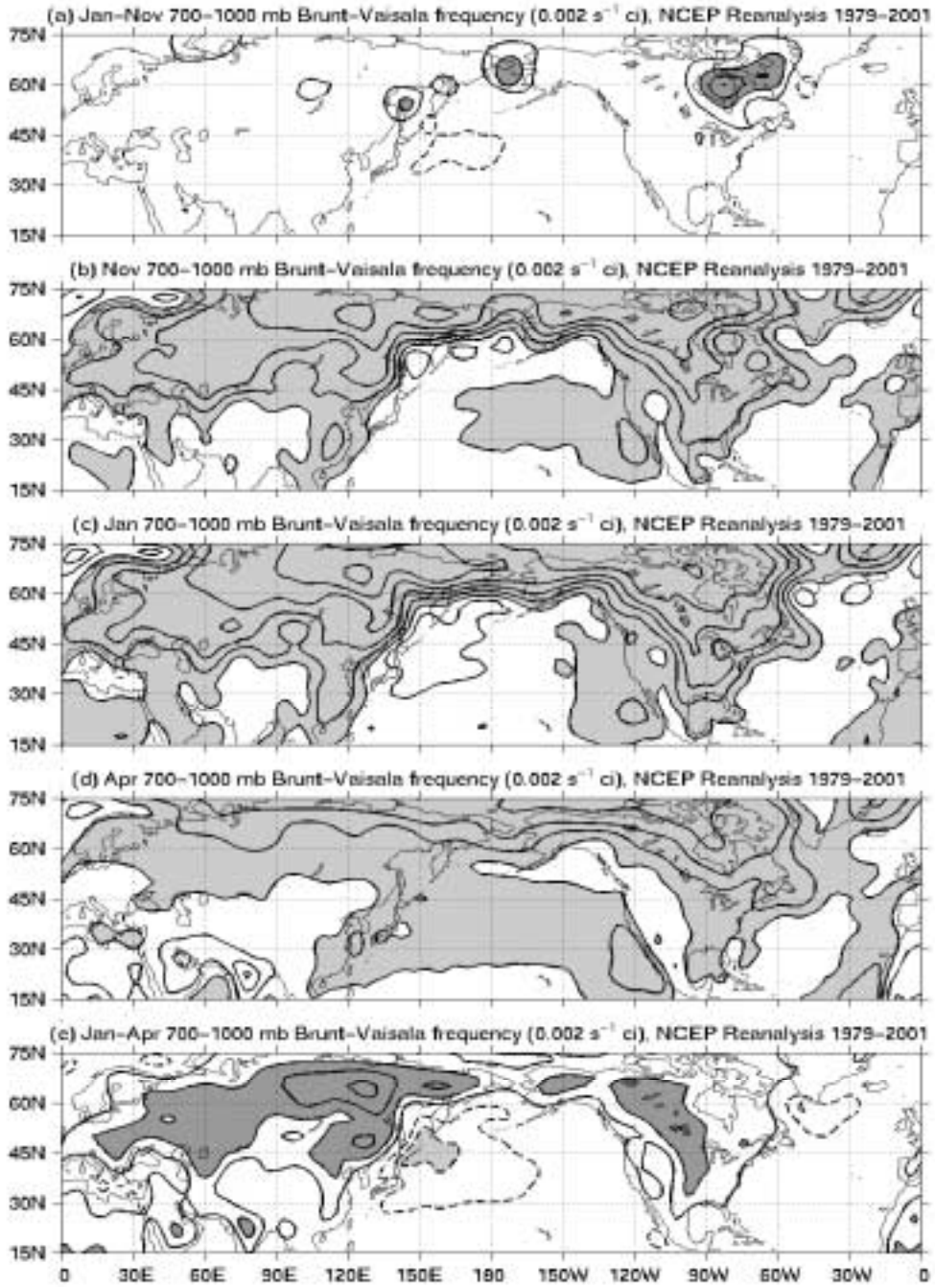

Figure 2.13: Mass-weighted average of the Brunt-Väisälä frequency between 700 mb and 1000 mb, for (a) January−November, (b) November, (c) January, (d) April, (e) January−April. In panels (a) and (e), the contour interval is 0.002 s^{-1}, with dashed negative contours and the zero contour omitted; light shading indicates values less than -0.004 s^{-1}, and dark shading indicates and values greater than 0.004 s^{-1}. In panels (b)–(d), the contour interval is 0.002 s^{-1}; shading indicates values greater than 0.012 s^{-1}. Calculations are based on NCEP Reanalysis data from September 1979 to August 2001.

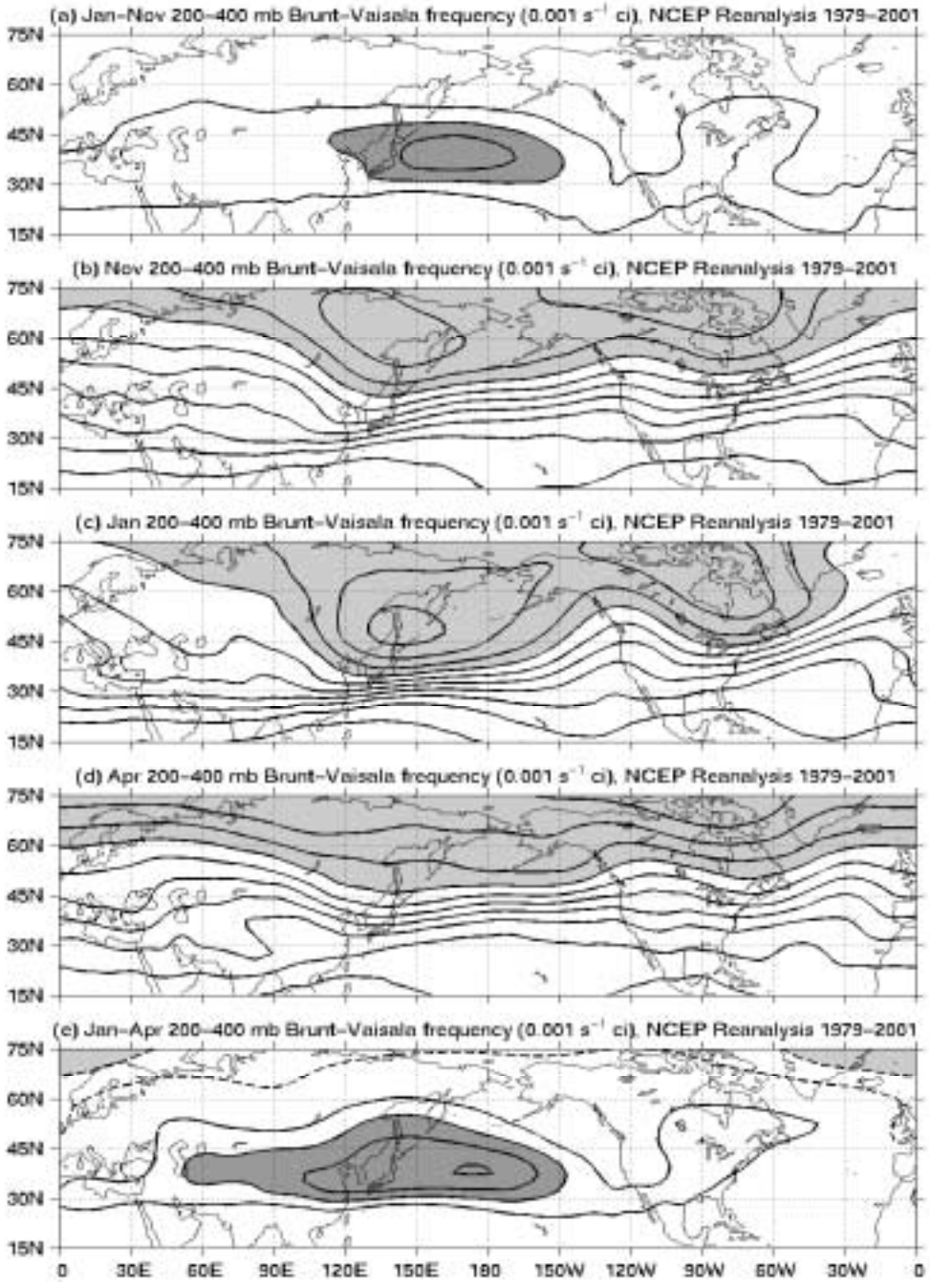

Figure 2.14: Mass-weighted average of the Brunt-Väisälä frequency between 200 mb and 400 mb, for (a) January−November, (b) November, (c) January, (d) April, (e) January−April. In panels (a) and (e), the contour interval is 0.001 s^{-1}, with dashed negative contours and the zero contour omitted; light shading indicates values less than -0.002 s^{-1}, and dark shading indicates and values greater than 0.002 s^{-1}. In panels (b)–(d), the contour interval is 0.001 s^{-1}; shading indicates values greater than 0.016 s^{-1}. Calculations are based on NCEP Reanalysis data from September 1979 to August 2001.

sharp gradient over the Pacific in January indicates that the tropopause slopes steeply with latitude in the strong subtropical jet. The lower tropopause on the poleward side of the Pacific jet is consistent with downward motion forced by cold advection and negative upper level vorticity advection, which becomes stronger as the Pacific jet becomes stronger and narrower in midwinter. The difference plots show that the static stability is larger in January than in November or April over eastern Asia and the western Pacific, centered near $40°$N; the changes in static stability are of the correct sign and occur at latitudes where they could plausibly contribute to the midwinter suppression of the Pacific storm track. We investigate the importance of static stability for the midwinter suppression in Chapters 3 and 4.

2.5 Baroclinicity

We take baroclinicity to mean the capacity for growing baroclinic waves. Baroclinic waves grow through the interaction of existing eddy energy with temperature gradients, or mean state APE. Regions of strong baroclinicity thus tend to have large meridional temperature gradients, which imply large vertical shear of the zonal wind, so baroclinic regions tend to be associated with strong upper-tropospheric jets. Baroclinic waves also grow more efficiently in regions of low static stability, as occur off the east coasts of Asia and North America in winter when cold continental air blows over the relatively warm ocean surface.

A convenient measure of baroclinicity is the maximum Eady growth rate:

$$\sigma = 0.31 \frac{f}{N} \left| \frac{\partial \mathbf{v}}{\partial z} \right| \tag{2.6}$$

where f is the Coriolis parameter and $\mathbf{v}$ is the mean state wind vector. σ was calculated by Lindzen and Farrell (1980) as the growth rate of the fastest-growing mode in the Charney problem for baroclinic instability and found to be applicable to a range of baroclinic instability problems. While it may be inappropriate to think of baroclinic waves in the real atmosphere as growing normal modes, we shall use σ as a measure of the local capacity for growing baroclinic waves.

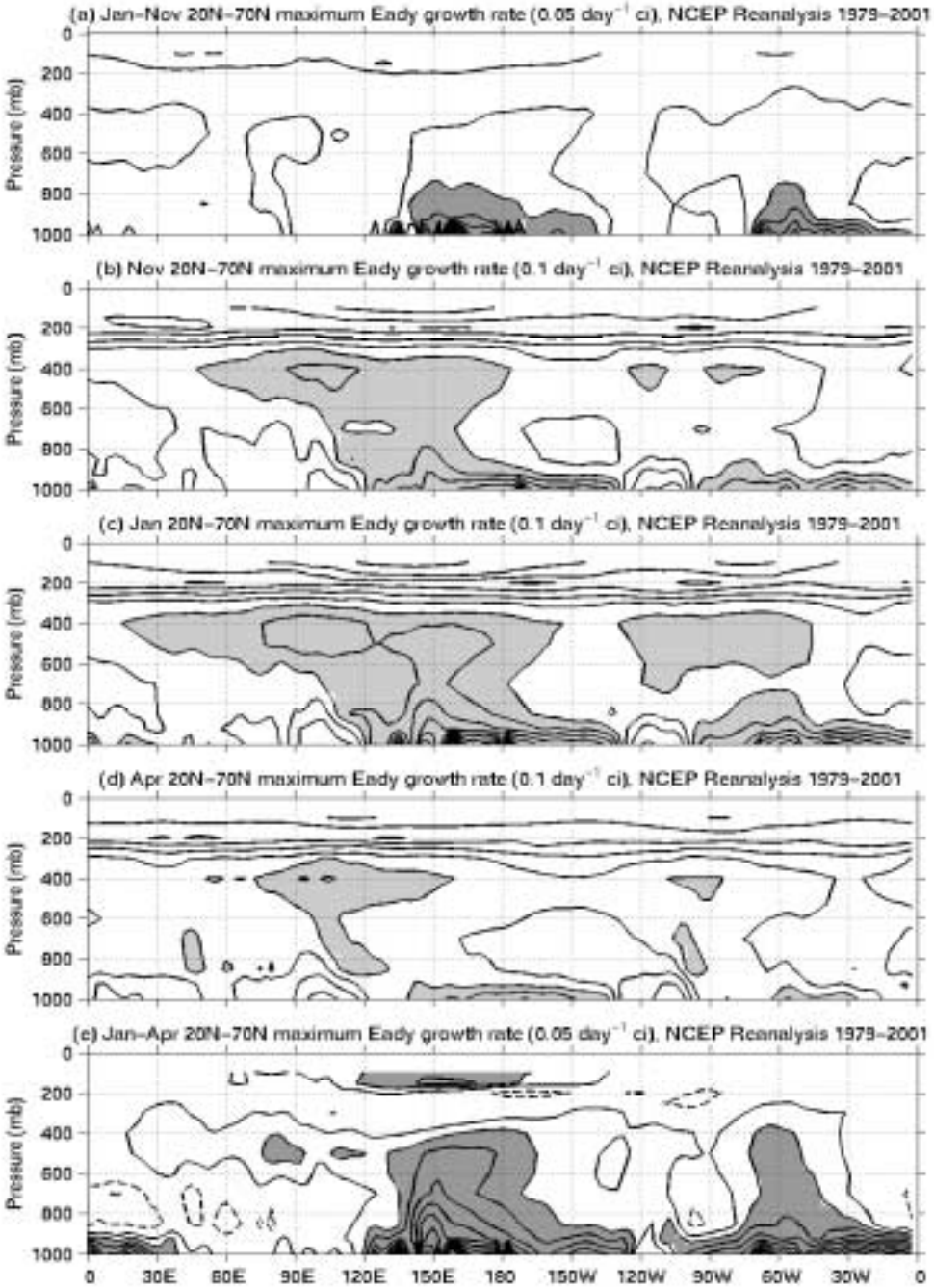

Figure 2.15: Mass-weighted average of the maximum Eady growth rate between $20°$N and $70°$N, for (a) January$-$November, (b) November, (c) January, (d) April, (e) January$-$April. In panels (a) and (e), the contour interval is 0.05 day^{-1}, with dashed negative contours and the zero contour omittedl; dark shading indicates values greater than 0.1 day^{-1}. In panels (b)–(d), the contour interval is 0.1 day^{-1}; shading indicates values greater than 0.5 day^{-1}. Calculations are based on NCEP Reanalysis data from September 1979 to August 2001.

Fig. 2.15 shows longitude-pressure cross sections of σ averaged from $20°$N to $70°$N. The largest values occur near the surface over the western oceans, in regions of small static stability; in January, when local values of N become extremely small, the near-surface σ becomes quite large. σ also becomes large between 300 mb and 600 mb under the Pacific and Atlantic jets (see Fig. 2.8), with σ larger under the jets in January than in November or April because of the stronger January jets. However, between 200 mb and 400 mb in the Pacific jet, σ is actually smaller in January than in November or April because of the large static stability there (see Fig. 2.12). In general, σ is larger in January than in April or, to a lesser degree, November, so we must explain why storm track intensity decreases in the Pacific despite greater baroclinicity in midwinter.

Typically, the value of σ for the layer from 700 mb to 850 mb has been considered representative of the baroclinicity which feeds the midlatitude storm tracks (e.g., Hoskins and Valdes 1990). However, as shown by Fig. 2.15, σ is actually largest in the layer between 850 mb and 1000 mb, and we shall see in Chapter 3 that the largest baroclinic generation of eddy energy occurs in this layer as well, so we take σ for this layer to be representative of the low-level baroclinicity which is important for the growth of baroclinic waves. Fig. 2.16 shows maps of σ calculated between 850 mb and 1000 mb; in winter, it is largest just off the eastern coasts of Asia and North America, where there is weak static stability and a large meridional gradient in sea surface temperature. We also note that the region of maximum low-level baroclinicity in the Pacific shifts only slightly equatorward, by less than $5°$ latitude, in January relative to November and April. This is caused by the equatorward shift in the maximum low-level zonal winds, which is driven by the equatorward shift in upper level momentum flux convergence associated with the storm track. Otherwise, while the relative magnitudes of σ in various regions change from month to month, the locations of large baroclinicity are generally tied to specific locations with large surface temperature gradients.

The upper level baroclinicity, associated with the shear under the Pacific jet, is also important for the baroclinic generation of eddy energy, so in Fig. 2.17 we show maps of σ

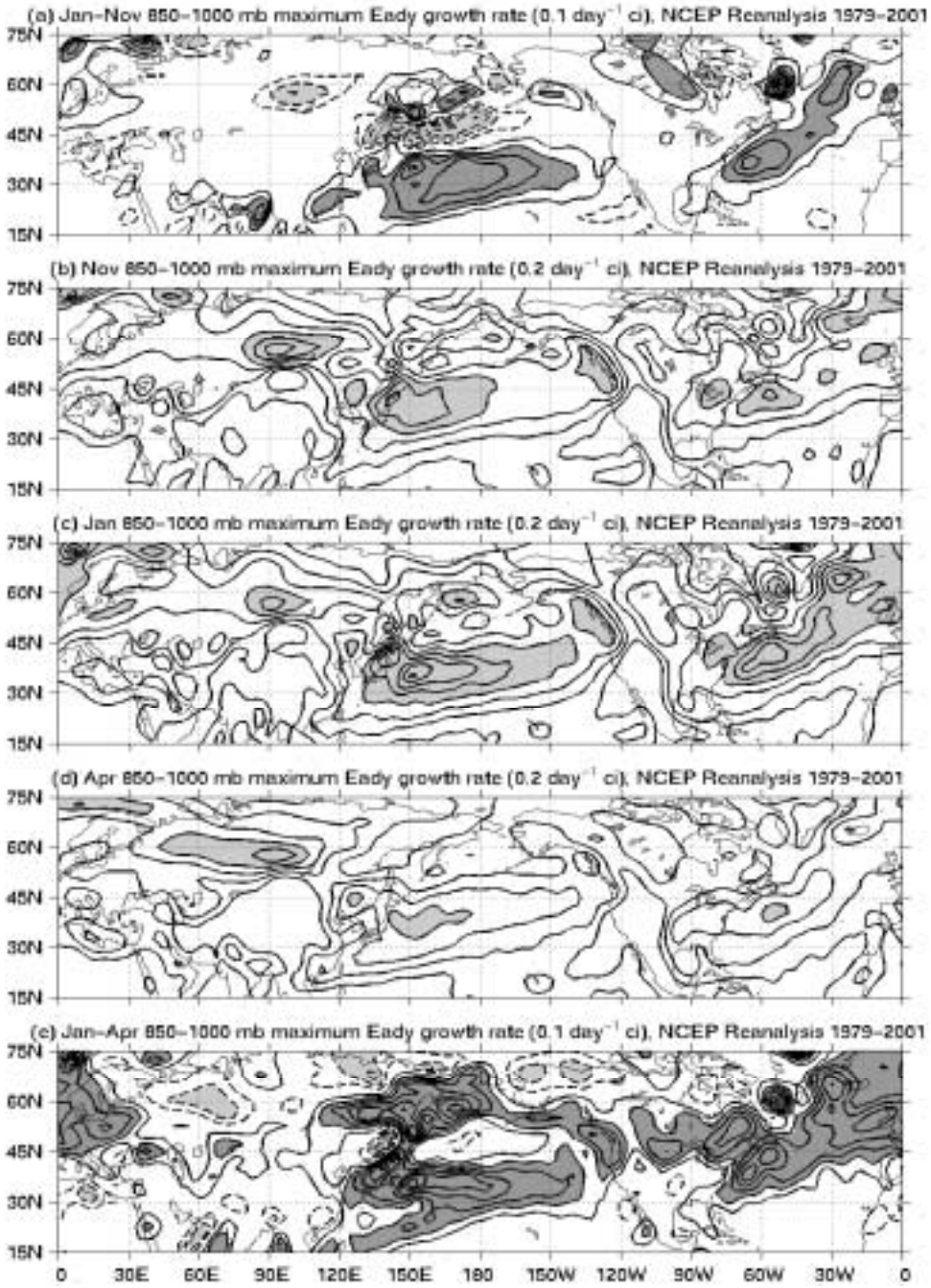

Figure 2.16: Maximum Eady growth rate calculated for the layer between 850 mb and 1000 mb, for (a) January−November, (b) November, (c) January, (d) April, (e) January−April. In panels (a) and (e), the contour interval is 0.1 day^{-1}, with dashed negative contours and the zero contour omitted; light shading indicates values less than -0.2 day^{-1}, and dark shading indicates and values greater than 0.2 day^{-1}. In panels (b)–(d), the contour interval is 0.2 day^{-1}; shading indicates values greater than 0.8 day^{-1}. Calculations are based on NCEP Reanalysis data from September 1979 to August 2001.

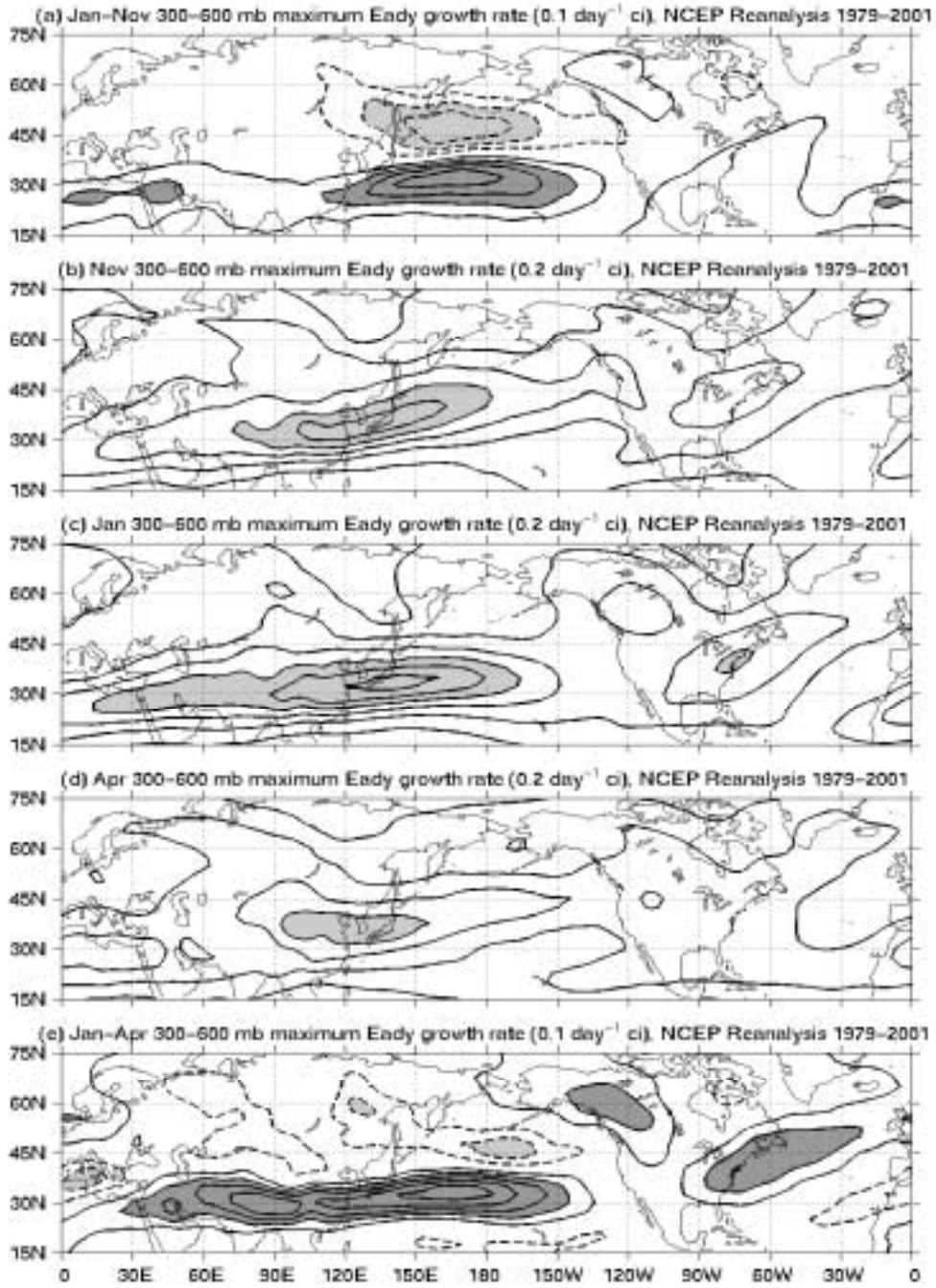

Figure 2.17: Maximum Eady growth rate calculated for the layer between 300 mb and 600 mb, for (a) January−November, (b) November, (c) January, (d) April, (e) January−April. In panels (a) and (e), the contour interval is 0.1 day^{-1}, with dashed negative contours and the zero contour omitted; light shading indicates values less than -0.2 day^{-1}, and dark shading indicates and values greater than 0.2 day^{-1}. In panels (b)–(d), the contour interval is 0.2 day^{-1}; shading indicates values greater than 0.8 day^{-1}. Calculations are based on NCEP Reanalysis data from September 1979 to August 2001.

calculated between 300 mb and 600 mb. The region of maximum upper level baroclinicity moves equatorward with the Pacific jet in midwinter, and, like the Pacific jet, the upper level baroclinic region is narrower in midwinter than in fall or spring. Comparing Figs. 2.17a and e to Figs. 2.4a and e, it appears that the changes in baroclinicity may explain the equatorward shift of the midwinter Pacific storm track, but not the overall decrease in intensity, because the increase in baroclinicity on the equatorward side of the storm track is larger than the decrease on the poleward side, particularly when compared to April. We will need to appeal to a mechanism other than the linear effect of baroclinicity on the growth rate of baroclinic waves to explain the midwinter suppression.

2.6 Summary

In this chapter, we have presented a four-dimensional picture of the midwinter suppression of the Pacific storm track and the accompanying changes in the mean state. The Pacific storm track intensity peaks in November and April, while in January it weakens and shifts equatorward, with the most significant reductions in storm track intensity above 500 mb over eastern Asia and the western Pacific. The equatorward shift in the storm track is accompanied by an equatorward shift of the Pacific jet, and the weakening of the storm track occurs primarily at latitudes where the jet is also weaker, so increased advection is unlikely to drive the observed suppression. There is evidence that the strengthening and narrowing of the Pacific jet in midwinter may be caused by the shift in western Pacific warm pool convection to the south of the equator. The baroclinicity associated with the jet also shifts equatorward in midwinter, but the baroclinicity is actually stronger in January than in November or April, so the midwinter suppression cannot be explained by the change in baroclinicity unless conditions on the poleward flank of the jet are more important than those on the equatorward flank. However, as the Pacific jet becomes more subtropical in midwinter, the tropopause slopes more steeply through the jet and results in large upper level static stabilty on the poleward flank of the jet, which decreases the efficiency of the

conversion of eddy APE to eddy KE (see Chapter 3) and inhibits deep temperature perturbations in baroclinic waves (see Chapter 4). The effects of these changes in the mean state on the midwinter suppression of the Pacific storm track will be investigated in the following chapters.

Chapter 3

EDDY ENERGY BUDGET ANALYSIS

One advantage of measuring the storm track intensity in terms of eddy APE and eddy KE is that we can easily compute the eddy energy budget to determine which terms are driving the changes in eddy energy. It is important to note that a budget analysis is unlikely to allow us to draw conclusions about the mechanisms that cause the midwinter suppression. However, since some mechanisms have particular signatures in the eddy energy budget (for example, suppression due to enhanced diffluence in the jet exit region would manifest as larger negative barotropic conversion in the storm track), we may be able to rule out some mechanisms based on the eddy energy budget analysis. The budget analysis will also provide some motivation for the lag regression analysis of baroclinic wave structure to be presented in Chapter 4.

3.1 Eddy energy budget equations

We follow Orlanski and Katzfey (1991) and Chang (2001) in writing the equations for eddy KE and eddy APE in a form that corresponds to the Lorenz energy cycle (Lorenz 1955). However, we will separate some of the terms in slightly different ways to better illustrate the processes involved. In the equations that follow for 2–10 day eddy statistics, primes denote departures of daily means from 5-day means, while unprimed variables correspond to the total field (eddy plus 5-day mean), and overbars denote time averages over 5-day periods.

First, the eddy APE budget can be written as follows:

$$\frac{\partial P}{\partial t} = -\boldsymbol{\nabla}_3 \cdot \overline{\mathbf{v}_3 P} + \frac{s^2}{(\Theta_p)^2}\left[- \overline{\theta'(\mathbf{v}' \cdot \boldsymbol{\nabla})\overline{\theta}} - \overline{\theta'\omega'\Theta_p} - \overline{\theta'\omega'(\overline{\theta}_p - \Theta_p} + \overline{\theta' Q'}\right] \qquad (3.1)$$

where $\mathbf{v}_3 = (u, v, \omega)$ is the three-dimensional wind, $\boldsymbol{\nabla}_3$ is the three-dimensional gradient operator, $\mathbf{v} = (u, v)$ is the horizontal wind, $\boldsymbol{\nabla}$ is the horizontal gradient operator, the subscript $()_p$ indicates the vertical (pressure) gradient, Q is the diabatic heating, and $\Theta(p)$ is again the potential temperature profile for a standard atmosphere (from appendix E of Holton 1992).

The first term on the right represents convergence of the advective flux of eddy APE, taking into account advection by the total (eddy plus mean) wind. We define this term as $PADV = -\boldsymbol{\nabla}_3 \cdot \overline{\mathbf{v}_3 P}$.

The second term represents the baroclinic generation of APE by horizontal eddy temperature advection. We define this term as $BCGEN_h = -(s^2/\Theta_p^2)\overline{\theta'(\mathbf{v}' \cdot \boldsymbol{\nabla})\overline{\theta}}$.

The sum of the third and fourth terms represents the consumption of APE by vertical motion in baroclinic waves. The third term represents baroclinic conversion from eddy APE to eddy KE, which, with our definition of APE, is proportional to the vertical eddy temperature advection across the vertical potential temperature gradient for the standard atmosphere. In order to define the baroclinic conversion from APE to KE as positive, we define the term $BCCON = (s^2/\Theta_p)\overline{\theta'\omega'}$, which is a simplified equivalent of the negative of the third term in the eddy APE budget. The fourth term is the remainder of the APE change due to vertical motion, which depends on the difference between the mean vertical potential temperature gradient and that for the standard atmosphere. Because this quantity is sometimes considered the vertical component of baroclinic generation, we define the term $BCGEN_v = -(s^2/\Theta_p^2)\overline{\theta'\omega'(\partial[\overline{\theta} - \Theta(p)]/\partial p)}$, with the sign chosen so that $BCGEN_v$ is positive when additional eddy APE is generated by vertical motion. In winter, $BCGEN_v$ is typically negative, indicating that there is more eddy APE consumed than eddy KE produced by vertical motion in the high static stability of winter.

The fifth term represents diabatic generation of eddy APE, which we calculate as a residual in the eddy APE budget because the NCEP Reanalysis does not provide diabatic heating on pressure levels; we define this term as $DIGEN = (s^2/\Theta_p^2)\overline{\theta' Q'}$. The diabatic generation term is generally negative near the surface, where temperature anomalies

are damped by the surface sensible heat flux, and tends to be positive aloft where warm anomalies are reinforced by latent heating. In order to describe these processes separately, we define the sensible heating part as $SHGEN = (s^2/\Theta_p^2)\overline{\theta' Q'}$ from 850 mb down and the latent heating part as $LHGEN = (s^2/\Theta_p^2)\overline{\theta' Q'}$ from 700 mb up.

Next, the eddy KE budget can be written as follows:

$$\frac{\partial K}{\partial t} = -\boldsymbol{\nabla}_3 \cdot \overline{\mathbf{v}_3 K} - \boldsymbol{\nabla} \cdot \overline{\mathbf{v}_a' \phi'} - (\overline{\omega' \phi'})_p + \frac{s^2}{\Theta_p}\overline{\omega' \theta'} - \overline{\mathbf{v}' \cdot (\mathbf{v}_3' \cdot \boldsymbol{\nabla}_3)\overline{\mathbf{v}}} + \overline{\text{Res.}} \qquad (3.2)$$

where $\mathbf{v}_a$ is the horizontal ageostrophic wind and $\phi = gz$ is the geopotential.

The first term on the right represents convergence of the advective flux of eddy KE, again taking into account advection by the total wind. We define this term as $KADV = -\boldsymbol{\nabla}_3 \cdot \overline{\mathbf{v}_3 K}$.

The second and third terms represent the horizontal and vertical convergence of the dispersive flux of eddy KE due to the ageostrophic geopotential flux. As discussed by Orlanski and Katzfey (1991), this flux represents the non-advective propagation of eddy KE. We define the horizontal and vertical convergence of the ageostrophic geopotential flux as $AGEO_h = -\boldsymbol{\nabla} \cdot \overline{\mathbf{v}_a' \phi'}$ and $AGEO_v = -(\overline{\omega' \phi'})_p$, respectively.

The fourth term is $BCCON$, which is the opposite of the third term in the eddy APE budget. This again represents baroclinic conversion from eddy APE to eddy KE.

The fifth term represents the barotropic conversion from mean flow KE to eddy KE. We define this term as $BTCON = -\overline{\mathbf{v}' \cdot (\mathbf{v}_3' \cdot \boldsymbol{\nabla}_3)\overline{\mathbf{v}}}$.

The sixth term is calculated as a residual in the eddy KE budget; it represents friction, nonlinearity, and other physical processes. We define this term as $KERES = \overline{\text{Res.}}$. We assume that the generally negative part of the residual near the surface is due to friction, so we define this part of the term as $FRIC = \overline{\text{Res.}}$ from 850 mb down. We define the part of the residual which is not due to friction as $NFRES = \overline{\text{Res.}}$ from 700 mb up.

3.2 Flow of eddy APE and KE in baroclinic waves

The analysis of the eddy energy budget (presented in section 3.3) and the lag regression analysis (presented in Chapter 4) gives us a relatively clear conceptual picture of the flow of eddy energy in baroclinic waves. We present a series of cartoons illustrating this conceptual picture here so that the reader can more easily understand the eddy energy budget analysis that follows. In these cartoons, the baroclinic wave structure is illustrated using contours from the lag regression analysis (see Chapter 4) in the longitude-pressure plane.

Fig. 3.1 illustrates the generation of eddy APE by the meridional motion in a baroclinic wave. The deeper, westward-tilting structure outlined in black represents a positive v' perturbation in a baroclinic wave, while the shallower, eastward-tilting structure outlined in red represents the accompanying positive θ' perturbation. θ' is produced primarily by eddy temperature advection across the mean meridional temperature gradient ($v'\partial\overline{\theta}/\partial y$), but tilts eastward because of the strong mean zonal wind ($\overline{u}$) at upper levels, which is represented by the arrow labeled $\overline{u}$. All eddy APE is initially generated by $BCGEN_h$, which is dominated by the reinforcement of θ' by the meridional eddy temperature advection ($-\theta'v'\partial\overline{\theta}/\partial y$), so $BCGEN_h$ is positive in the red shaded region where both v' and θ' are positive. While $BCGEN_h$ is often considered to be the generation of eddy APE from mean state APE, we prefer to think of $BCGEN_h$ as the product of interaction between existing eddy energy and the mean state temperature gradient because it would not occur without v' and θ'. Near the surface, the eddy APE produced by $BCGEN_h$ is almost immediately damped by surface sensible heat fluxes, represented by the wavy downward arrows, which result in the consumption of eddy APE by $SHGEN$. Thus, $BCGEN_{eff} = BCGEN_h + SHGEN$ is the rate of eddy APE generation which is actually available to drive vertical motion in baroclinic waves.

Fig. 3.2 illustrates the consumption of eddy APE and production of eddy KE by the vertical motion in a baroclinic wave. The shallow, eastward-tilting structure in red again represents a positive θ' perturbation, while the deep vertical structure in black represents

the accompanying negative ω' perturbation where there is upward motion (indicated by the upward arrow). The consumption of eddy APE by vertical motion will be positive in the blue shaded regions where ω' is negative and θ' is positive. We illustrate here the effect of the lowering of the tropopause in midwinter; the two horizontal lines represent the boundaries of the region where the static stability is higher than that of the reference atmosphere ($\overline{\theta}_p < \Theta_p$) in the region where the tropopause is lower. Because $BCGEN_v$ is negative between the two horizontal lines and zero elsewhere, the consumption of eddy APE by vertical motion is equal to $BCCON - BCGEN_v$ in the upper, dark blue shaded region and just $BCCON$ in the lower, light blue shaded region. In addition, the latent heating in the upward vertical motion, indicated by the "cloud" bounded by the grey dashed line, reduces the amount of eddy APE consumed by vertical motion by $LHGEN$ in the region where the "cloud" intersects the positive θ' perturbation. Thus, the total consumption of eddy APE by vertical motion is $BCCON - BCGEN_v - LHGEN$; this is equal to the effective baroclinic generation of eddy APE, $BCGEN_{eff}$, when averaged over the lifetime of the baroclinic wave. Because $BCCON$ is the amount of eddy KE produced by the vertical motion, the ratio of $BCCON$ to the total eddy APE consumed by the vertical motion,

$$\epsilon_{BCCON} = \frac{BCCON}{BCCON - BCGEN_v - LHGEN}, \tag{3.3}$$

can be thought of as the efficiency of baroclinic conversion from eddy APE to eddy KE, which depends on both the mean stability and the availability of moisture. Higher stability results in more negative $BCGEN_v$, which reduces ϵ_{BCCON}, while more moisture results in more positive $LHGEN$, which increases ϵ_{BCCON}.

Fig. 3.3 illustrates the redistribution of eddy KE by the vertical motion in a baroclinic wave. The solid and dashed westward-tilting structures represent positive and negative ϕ' perturbations, respectively. Because upward motion (indicated by the thin upward arrow) tends to extend from lows ($\phi' < 0$) near the surface to highs ($\phi' > 0$) aloft, the vertical ageostrophic geopotential flux (represented by the thick arrows) is downward ($\omega'\phi' > 0$) near the surface and upward ($\omega'\phi' < 0$) aloft. Thus, $AGEO_v$ transports eddy KE away

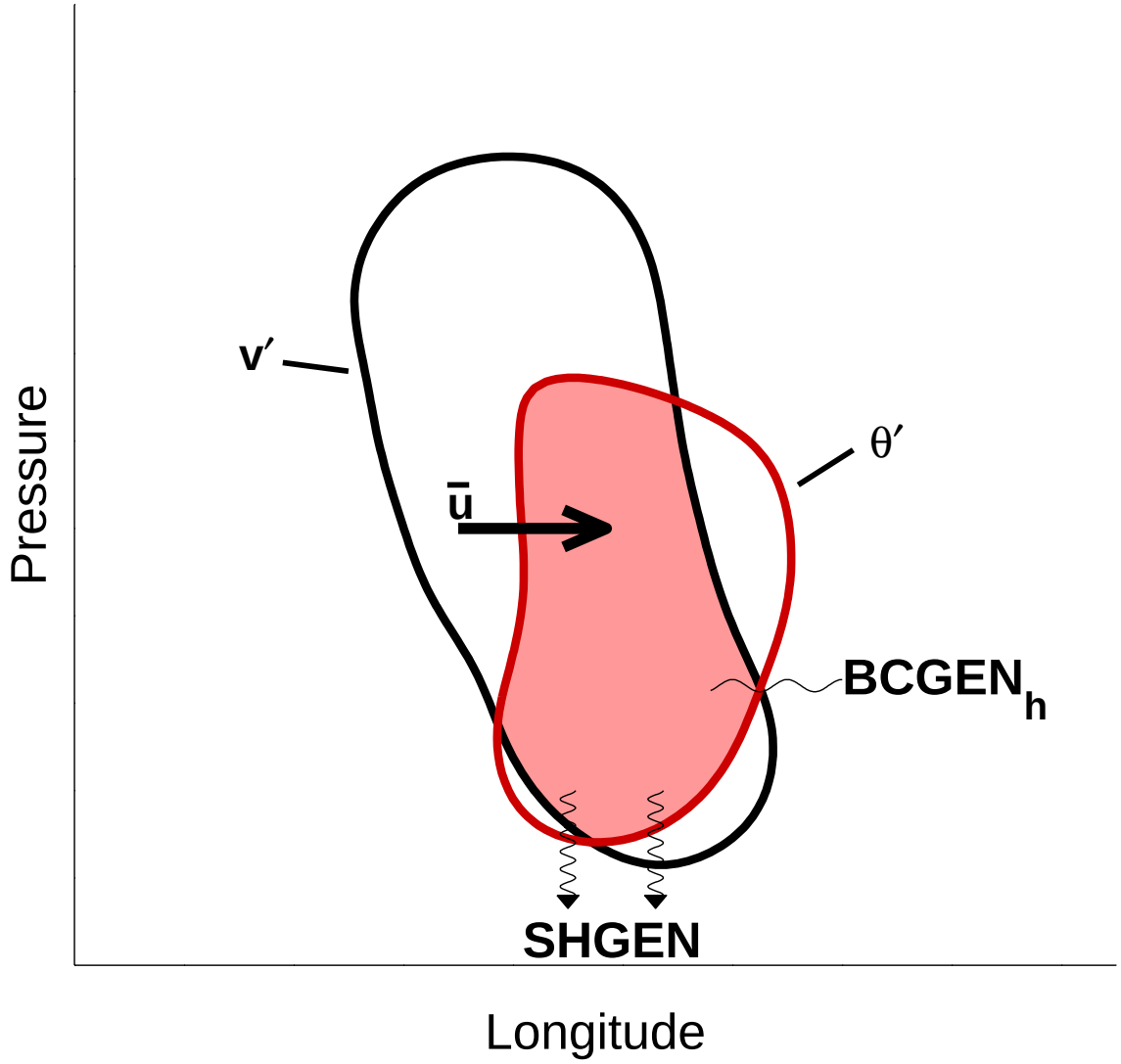

Figure 3.1: Cartoon illustrating the baroclinic generation of eddy APE by meridional motion in a baroclinic wave. Contours used in this cartoon were taken from the day 0 regression on v' at 925 mb, $37.5°$N, $155°$E (see Chapter 4); these contours are viewed in the longitude-pressure plane. The black contour represents a positive v' perturbation, while the red contour represents a positive θ' perturbation. The westerly mean zonal wind is represented by the horizontal arrow labeled $\overline{u}$. $BCGEN_h$ is positive in the red shaded region, where both v' and θ' are positive. $SHGEN$ is negative near the surface where sensible heat fluxes (represented by wavy downward arrows) consume the eddy APE produced by $BCGEN_h$. We define $BCGEN_{eff} = BCGEN_h + SHGEN$ as the rate of eddy APE generation by meridional motion that is available to be consumed by vertical motion in baroclinic waves.

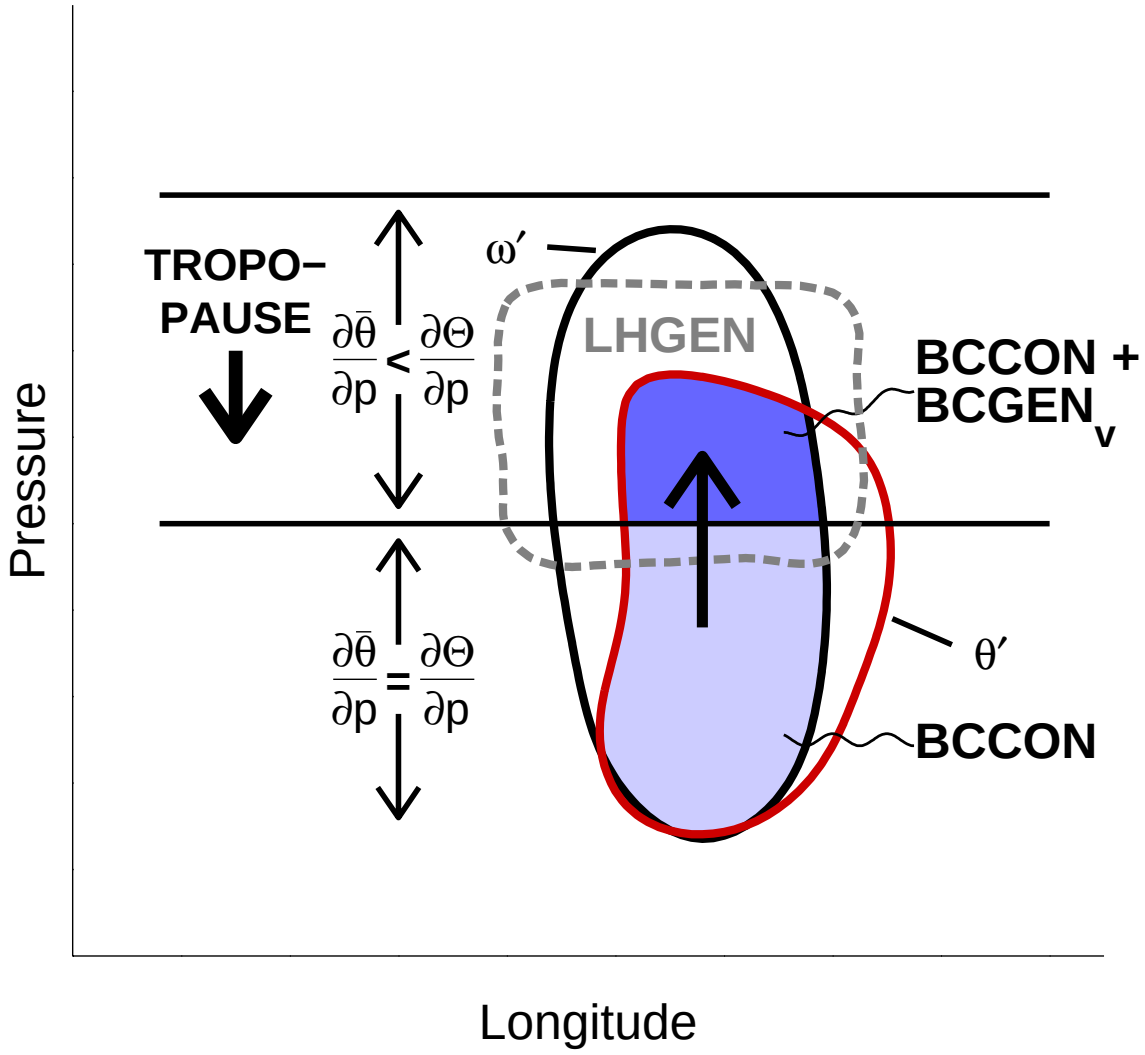

Figure 3.2: Cartoon illustrating the baroclinic conversion of eddy APE to eddy KE by vertical motion in a baroclinic wave. Contours used in this cartoon were taken from the day 0 regression on v' at 925 mb, 37.5°N, 155°E (see Chapter 4); these contours are viewed in the longitude-pressure plane. The black contour and upward arrow represent a negative (upward) ω' perturbation, while the red contour represents a positive θ' perturbation. $BCCON$ is positive in the blue shaded region, where ω' is negative and θ' is positive. The region between the two horizontal lines represents the layer where the static has increased due to the lowering of the tropopause in midwinter. In this region, the static stability is larger than that of the reference atmosphere, so $BCGEN_v$ is negative in the dark blue shaded region, where the total amount of eddy APE consumed adiabatically by the vertical motion is $BCCON - BCGEN_v$. The positive generation of eddy APE by moist heating is represented by the "cloud" bounded by the grey dashed line labeled $LHGEN$; $LHGEN$ is positive where the "cloud" intersects with the positive θ' perturbation. The total amount of eddy KE produced by the vertical motion is $BCCON$, while the total amount of eddy APE consumed by the vertical motion is $BCCON - BCGEN_v - LHGEN$.

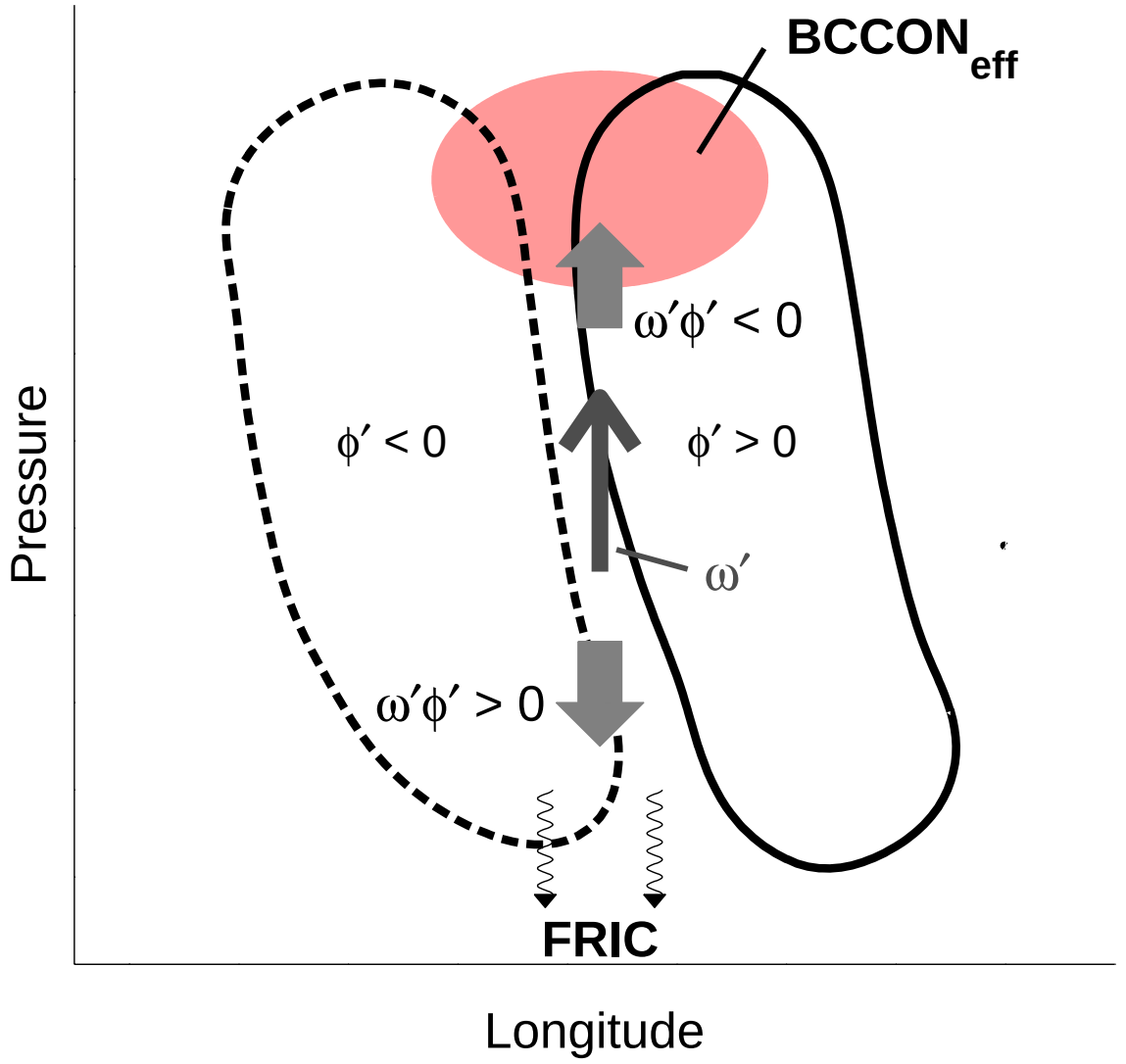

Figure 3.3: Cartoon illustrating the redistribution of eddy KE by vertical motion in a baroclinic wave. Contours used in this cartoon were taken from the day 0 regression on v' at 925 mb, 37.5°N, 155°E (see Chapter 4); these contours are viewed in the longitude-pressure plane. The solid and dashed black contours represent positive and negative ϕ' perturbations, while the thin upward arrow represents a negative (upward) ω' perturbation. The vertical ageostrophic geopotential flux, represented by the thick grey arrows labeled $\omega'\phi'$, tends to be upward at upper levels and downward at low levels, so $AGEO_v$ transports eddy KE from the middle troposphere and deposits it at upper levels and near the surface. The eddy KE deposited near the surface is consumed by friction, represented by the wavy downward arrows, so only the eddy KE deposited at upper levels, which we define as $BCCON_{eff} = BCCON + AGEO_v + FRIC$, persists to be measured by eddy KE statistics.

from the middle troposphere where it is produced by $BCCON$ and deposits eddy KE at upper levels and near the surface. The eddy KE that converges near the surface is almost immediately damped by friction, represented by the wavy downward arrows, which results in the consumption of eddy KE by $FRIC$. Only the eddy KE that converges at upper levels, which we define as $BCCON_{eff} = BCCON + AGEO_v + FRIC$ and represent as the red shaded region at upper levels, persists to be seen in eddy KE statistics. $BCCON_{eff}$ may be considered the effective rate of eddy KE production by vertical motion after all of the effects of vertical motion are taken into account. We define

$$\epsilon_{FRIC} = \frac{\langle BCCON_{eff} \rangle_V}{\langle BCCON \rangle_V} \tag{3.4}$$

as the fraction of eddy KE produced that is *not* consumed by $FRIC$, where $\langle\rangle_V$ represents the mass-weighted average over a volume V; for the purposes of this chapter, we define V as the volume bounded by $100°$E-$180°$, $20°$N-$70°$N, and 100 mb-1000 mb, in which the bulk of the forcing of the midwinter suppression occurs. When $BCCON$ occurs at lower levels, the eddy KE produced is more likely to be transported downward by $AGEO_v$ and consumed by $FRIC$, which results in a smaller value of ϵ_{FRIC}.

In summary: Eddy APE is produced primarily by meridional temperature advection in baroclinic waves, and consumed by vertical motion. Vertical motion also produces eddy KE and transports it upward and downward by ageostrophic geopotential fluxes. The fraction of eddy KE transported downward is almost immediately consumed by friction, so only the fraction of eddy KE transported upward persists. The efficiency of conversion from eddy APE to eddy KE by vertical motion (ϵ_{BCCON}) is determined by the mean stability and moisture availability, and the fraction of eddy KE that persists (ϵ_{FRIC}) depends on the altitude at which it is produced.

3.3 Comparison of eddy energy budget terms for November, January, and April

Based on the results of Chapter 2, we take November, January, and April as representative of the fall maximum, midwinter minimum, and spring maximum in Pacific storm track

intensity. In this section, we compare the eddy APE and eddy KE budget terms for these three months.

3.3.1 Efficiency of baroclinic generation

We begin our examination of the eddy APE budget with $BCGEN_h$, which, as discussed in the previous section, is the initial source of all eddy APE. Fig. 3.4 shows longitude-pressure cross sections of $BCGEN_h$; as in all of the eddy energy budget term figures to follow, the average from $20°N$ to $70°N$ is shown for November, January, and April in the middle three panels, while the top panel shows the January $-$ November difference and the bottom panel shows the January $-$ April difference. In all three months, we see that $BCGEN_h$ is large in the Pacific storm track between $100°$E and $140°$W; the maxima in $BCGEN_h$ that occur $105°$W-$25°$W and $30°$E-$90°$E are associated with the Atlantic and Siberian storm tracks, respectively. In the Pacific storm track, the primary difference between January and November is that $BCGEN_h$ is weaker above 500 mb in January from $100°$E to $180°$; $BCGEN_h$ tends to be stronger in January near the surface, but this difference is less systematic. The January $-$ April difference shows that $BCGEN_h$ is much weaker above 600 mb from $100°$E to $150°$E and slightly weaker near the surface over Asia (west of $120°$E); otherwise, $BCGEN_h$ is stronger in January than in April. Relative to both November and April, the regions of reduced upper level $BCGEN_h$ are located on the upstream end of the regions of reduced January eddy TE shown in Fig. 2.5a and e, *which suggests that the mechanism responsible for the weaker upper level $BCGEN_h$ in January may be causing at least part of the midwinter suppression of the Pacific storm track.*

As our goal is to explain why midwinter suppression occurs despite the greater baroclinicity in midwinter, we now investigate whether $BCGEN_h$ is reduced in January by changes in the efficiency of interactions between eddy APE, eddy KE, and the mean temperature gradient. We will focus on the meridional baroclinic generation, $BCGEN_{hy} = -(s^2/\Theta_p^2)\overline{\theta' v'(\partial\overline{\theta}/\partial y)}$, because this term produces over 90% of $BCGEN_h$ in the Pacific storm track. The longitude-pressure cross section of $BCGEN_{hy}$ for January, calculated

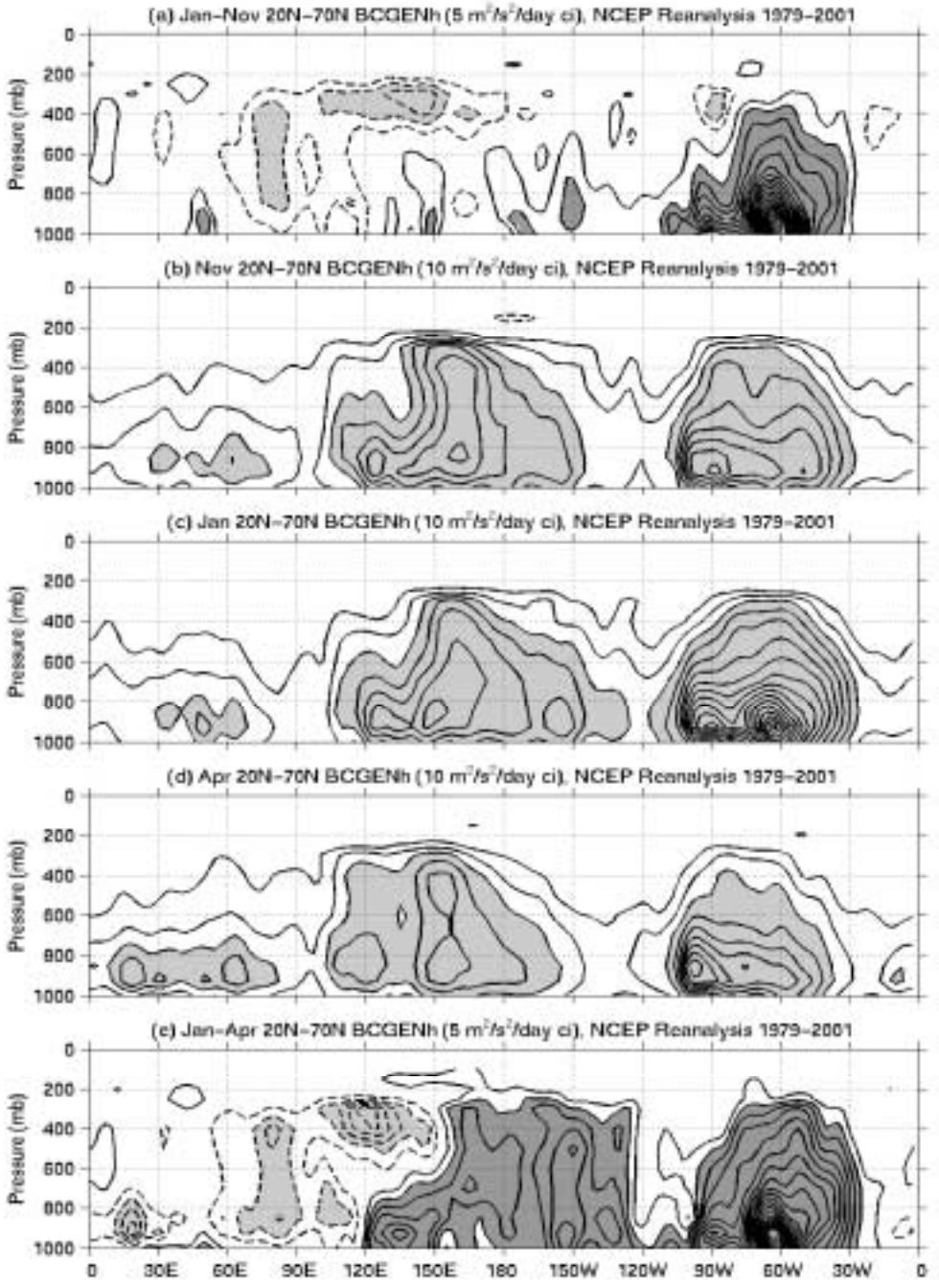

Figure 3.4: Mass-weighted average of $BCGEN_h$ between 20°N and 70°N, for (a) January−November, (b) November, (c) January, (d) April, (e) January−April. In panels (a) and (e), the contour interval is 5 m^2/s^2/day, with dashed negative contours and the zero contour omitted; light shading indicates values less than -10 m^2/s^2/day, and dark shading indicates values greater than 10 m^2/s^2/day. In panels (b)–(d), the contour interval is 10 m^2/s^2/day; shading indicates values greater than 30 m^2/s^2/day. Calculations are based on NCEP Reanalysis data from September 1979 to August 2001.

using the 22-year January mean $\overline{\theta}$, is shown in Fig. 3.5c; this quantity is approximately 10% smaller than $BCGEN_{hy}$ calculated using $\overline{\theta}$ for each 5-day period, because $\theta' v'$ tends to be larger when $\partial\overline{\theta}/\partial y$ is larger. Comparing Figs. 3.4c and 3.5c, however, the structure of $BCGEN_{hy}$ calculated using the overall January $\overline{\theta}$ is still very similar to that of $BCGEN_h$, with only slightly smaller magnitude, so it is not unreasonable to extend the following results for $BCGEN_{hy}$ to the total $BCGEN_h$.

We expect that the magnitude of $BCGEN_{hy}$ will be determined by the magnitudes of and correlations between v', θ', and $\partial\overline{\theta}/\partial y$. v'^2 and eddy APE (P) provide good estimates of the magnitudes of v' and θ'. First, we define

$$G = \frac{s^2}{(\Theta_p)^2}\left(\frac{\partial\overline{\theta}}{\partial y}\right)^2 \tag{3.5}$$

as a measure of the magnitude of $\partial\overline{\theta}/\partial y$, including the s^2/Θ_p^2 factor to give the correct scaling between APE and KE. Consistent with the baroclinicity shown in Fig. 2.15, G (not shown) is larger in January than in November or April. We can now define two parameters which describe the correlations between v', θ', and $\partial\overline{\theta}/\partial y$. The first represents the structure of the eddies:

$$k_{ED} = \frac{\langle (s^2/\Theta_p^2)(\overline{v'\theta'})^2\rangle^{\frac{1}{2}}}{\langle v'^2\rangle^{\frac{1}{2}}\langle P\rangle^{\frac{1}{2}}}, \tag{3.6}$$

where $\langle\rangle$ indicates a meridional average from $20°$N to $70°$N. Larger values of k_{ED} indicate that eddies are more optimally structured to generate eddy APE through $BCGEN_{hy}$ because v' and θ' are more highly correlated in space and time. The second represents the structure of the storm track:

$$k_{ST} = \frac{\langle BCGEN_{hy}\rangle}{\langle (s^2/\Theta_p^2)(\overline{v'\theta'})^2\rangle^{\frac{1}{2}}\langle G\rangle^{\frac{1}{2}}}. \tag{3.7}$$

Larger values of k_{ST} indicate that $v'\theta'$ and $\partial\overline{\theta}/\partial y$ are more optimally aligned to generate eddy APE through $BCGEN_{hy}$. These parameters relate $BCGEN_{hy}$ to the mean temperature gradient and eddy magnitudes as follows:

$$\langle BCGEN_{hy}\rangle = k_{ED} \times k_{ST} \times \langle G\rangle^{\frac{1}{2}}\langle v'^2\rangle^{\frac{1}{2}}\langle P\rangle^{\frac{1}{2}}. \tag{3.8}$$

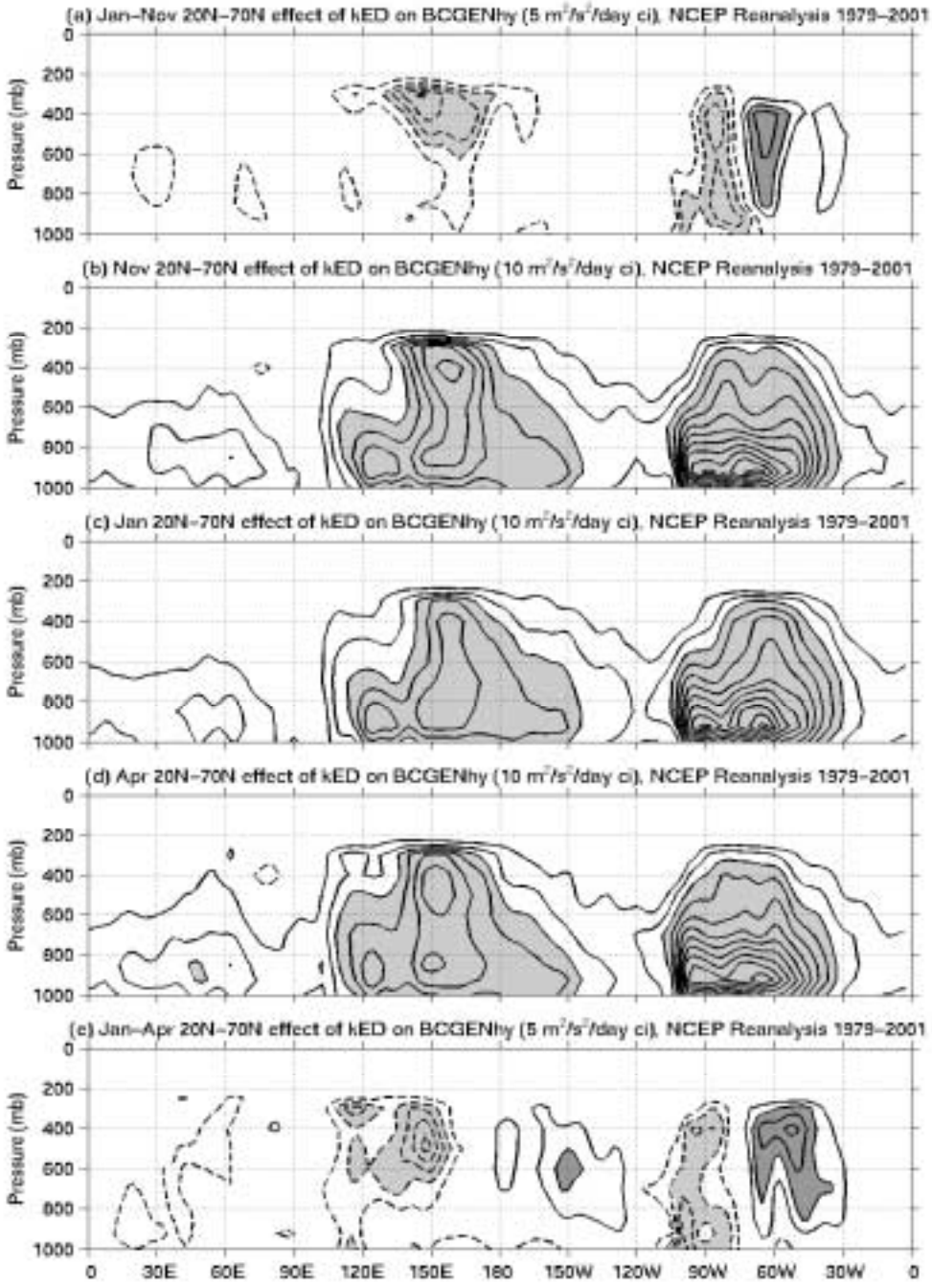

Figure 3.5: Mass-weighted average of $BCGEN_{hy}$ between $20°$N and $70°$N, calculated using eddy structure parameter k_{ED} for (a) January$-$November, (b) November, (c) January, (d) April, (e) January$-$April, and all other parameters set to their January values. In panels (a) and (e), the contour interval is 5 m^2/s^2/day, with dashed negative contours and the zero contour omitted; light shading indicates values less than -10 m^2/s^2/day, and dark shading indicates values greater than 10 m^2/s^2/day. In panels (b)–(d), the contour interval is 10 m^2/s^2/day; shading indicates values greater than 30 m^2/s^2/day. Calculations are based on NCEP Reanalysis data from September 1979 to August 2001.

We now calculate the effects of eddy and storm track structure on $BCGEN_{hy}$ by varying either k_{ED} or k_{ST} by month and setting all other variables in equation (3.8) to their values for January; results are similar when all other variables are set to their values for November or April. The effect of k_{ED} on $BCGEN_{hy}$ is shown in Fig. 3.5. Comparing Fig. 3.5a to Fig. 3.4a, the decrease in the efficiency of baroclinic generation due to eddy structure appears to be more than large enough to explain the January $-$ November decrease in $BCGEN_h$ at upper levels over the western Pacific, particularly between $130°$E and $180°$; in fact, the less optimal eddy structure can explain the decrease in $BCGEN_h$ despite the larger G in January. Comparing Fig. 3.5e to Fig. 3.4e, the less optimal eddy structure also appears to be able to explain much of the January $-$ April reduction in $BCGEN_h$ over the western Pacific, with some left over to compensate for the larger G in January near $150°$E. However, near $120°$E the effect of k_{ED} does not appear to be quite large enough to explain the entire decrease in $BCGEN_h$ in January relative to both November and April.

For comparison, the effect of k_{ST} on $BCGEN_{hy}$ is shown in Fig. 3.6. The storm track structure does not have as large an effect on baroclinic generation efficiency as eddy structure does, although it does supplement the effect of k_{ED} by providing a small negative effect on $BCGEN_{hy}$ at upper levels near $120°$E in January relative to both November and April. Comparing Figs. 3.6a and e to Figs. 3.4a and e, k_{ST} also appears to explain much of the relatively small decrease in $BCGEN_h$ over Asia ($60°$E-$90°$E) in January relative to both November and April.

In order to quantify the effects of k_{ED} and k_{ST} on the midwinter suppression, we calculate the factor by which these parameters reduce the mass-weighted average of $BCGEN_{hy}$ over the volume V in which most of the suppression is forced. k_{ED} reduces January $BCGEN_{hy}$ by factors of 0.86 and 0.84 relative to November and April, respectively, while k_{ST} only reduces $BCGEN_{hy}$ by factors of 0.97 and 0.99 relative to November and April. Thus, *the effects of eddy structure on the efficiency of baroclinic generation appear to cause most of the midwinter reduction in $BCGEN_h$ over the western Pacific*. In addition, this reduction in efficiency may be large enough to explain why $BCGEN_h$ decreases despite the

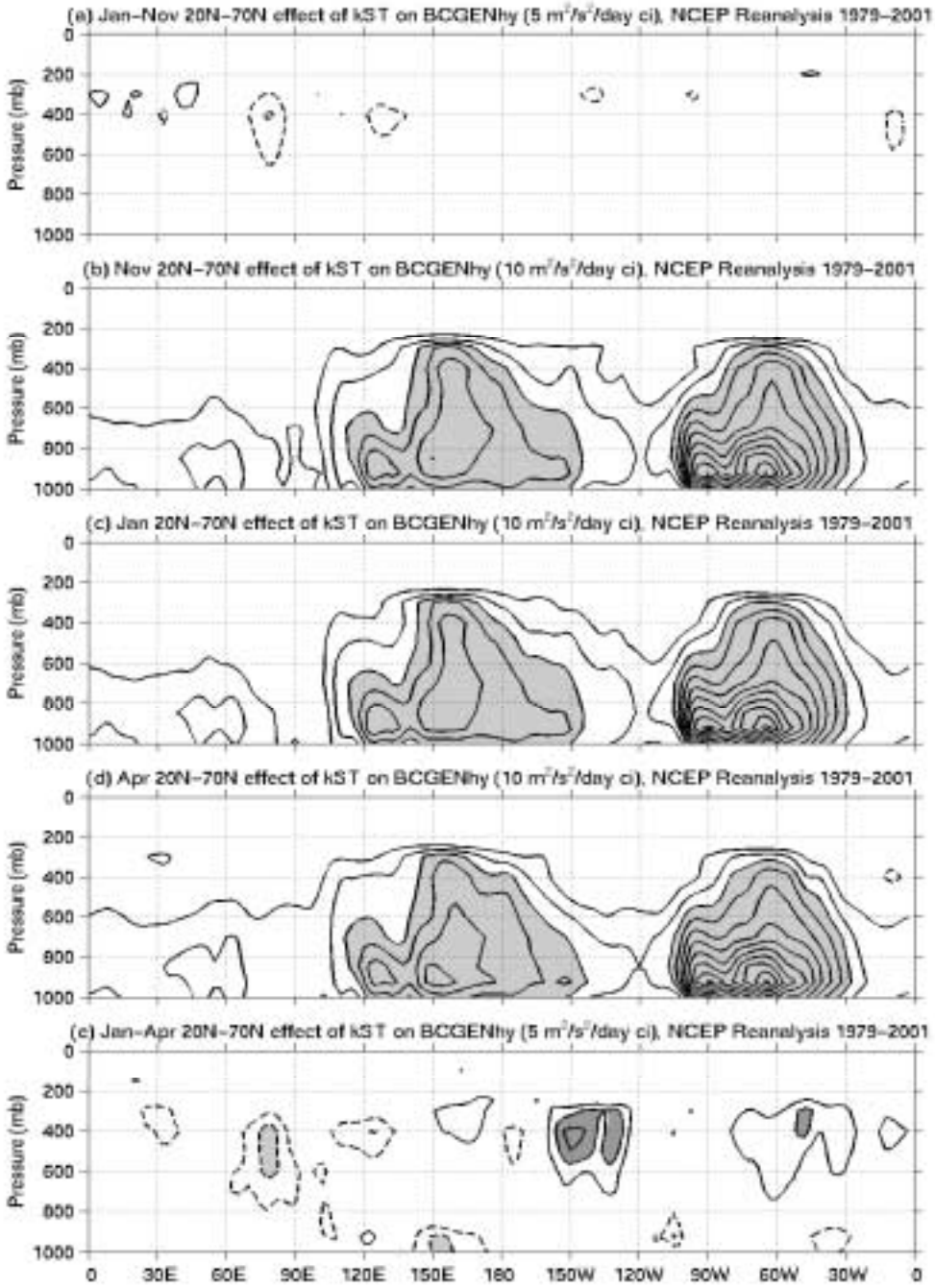

Figure 3.6: Mass-weighted average of $BCGEN_{hy}$ between $20°$N and $70°$N, calculated using storm track structure parameter k_{ST} for (a) January$-$November, (b) November, (c) January, (d) April, (e) January$-$April, and all other parameters set to their January values. In panels (a) and (e), the contour interval is 5 m^2/s^2/day, with dashed negative contours and the zero contour omitted; light shading indicates values less than -10 m^2/s^2/day, and dark shading indicates values greater than 10 m^2/s^2/day. In panels (b)–(d), the contour interval is 10 m^2/s^2/day; shading indicates values greater than 30 m^2/s^2/day. Calculations are based on NCEP Reanalysis data from September 1979 to August 2001.

increase in baroclinicity in midwinter. We investigate the form and cause of the midwinter changes in eddy structure using lag regression analysis in Chapter 4.

3.3.2 Efficiency of baroclinic conversion

As explained in section 3.2, the efficiency of baroclinic conversion from eddy APE to eddy KE by vertical motion (ϵ_{BCCON}) is increased by moisture through $LHGEN$ and decreased by static stability through $BCGEN_v$. We first examine $LHGEN$. Because we could not obtain diabatic terms directly from the NCEP Reanalysis, we estimate $LHGEN$ as equal to the values of $DIGEN$ from 700 mb up. Fig. 3.7 shows longitude-pressure cross sections of $DIGEN$, and illustrates our division of $DIGEN$ into two parts: the negative values from 850 mb down due to $SHGEN$, and the positive values from 700 mb up due to $LHGEN$. We first note that a comparison of Fig. 3.7 to Fig. 3.4 shows that $SHGEN$ is approximately equal to $-BCGEN_h$ near the surface, indicating that $SHGEN$ rapidly damps the eddy APE produced by $BCGEN_h$ near the surface as shown schematically in Fig. 3.1; this reduces the amount of eddy APE available to be converted into eddy KE by vertical motion to $BCGEN_{eff}$.

The division of $DIGEN$ into $SHGEN$ and $LHGEN$ is supported by explicit calculations of the diabatic generation terms for 20 years of a standard control GCM experiment that we performed using the NCAR CCM3.6 (Kiehl et al. 1996) at T42 resolution (approximately 2.8° latitude by 2.8° longitude); these calculations are shown in Fig. 3.8. The top panel shows $DIGEN$ for November of the control experiment, while the lower four panels show the generation of eddy APE by each diabatic term separately. Fig. 3.8 confirms that nearly all of the $DIGEN$ from 850 mb down is due to $SHGEN$, and nearly all of the $DIGEN$ from 700 mb up is due to $LHGEN$, although $DIGEN$ also includes small contributions from longwave and shortwave radiation (note the smaller contour intervals in the lower two panels)

Returning our attention to $LHGEN$, Fig. 3.7 shows that the maximum in $LHGEN$ occurs closest to Asia in April, and farthest downstream over the Pacific in January. Fig. 3.7a

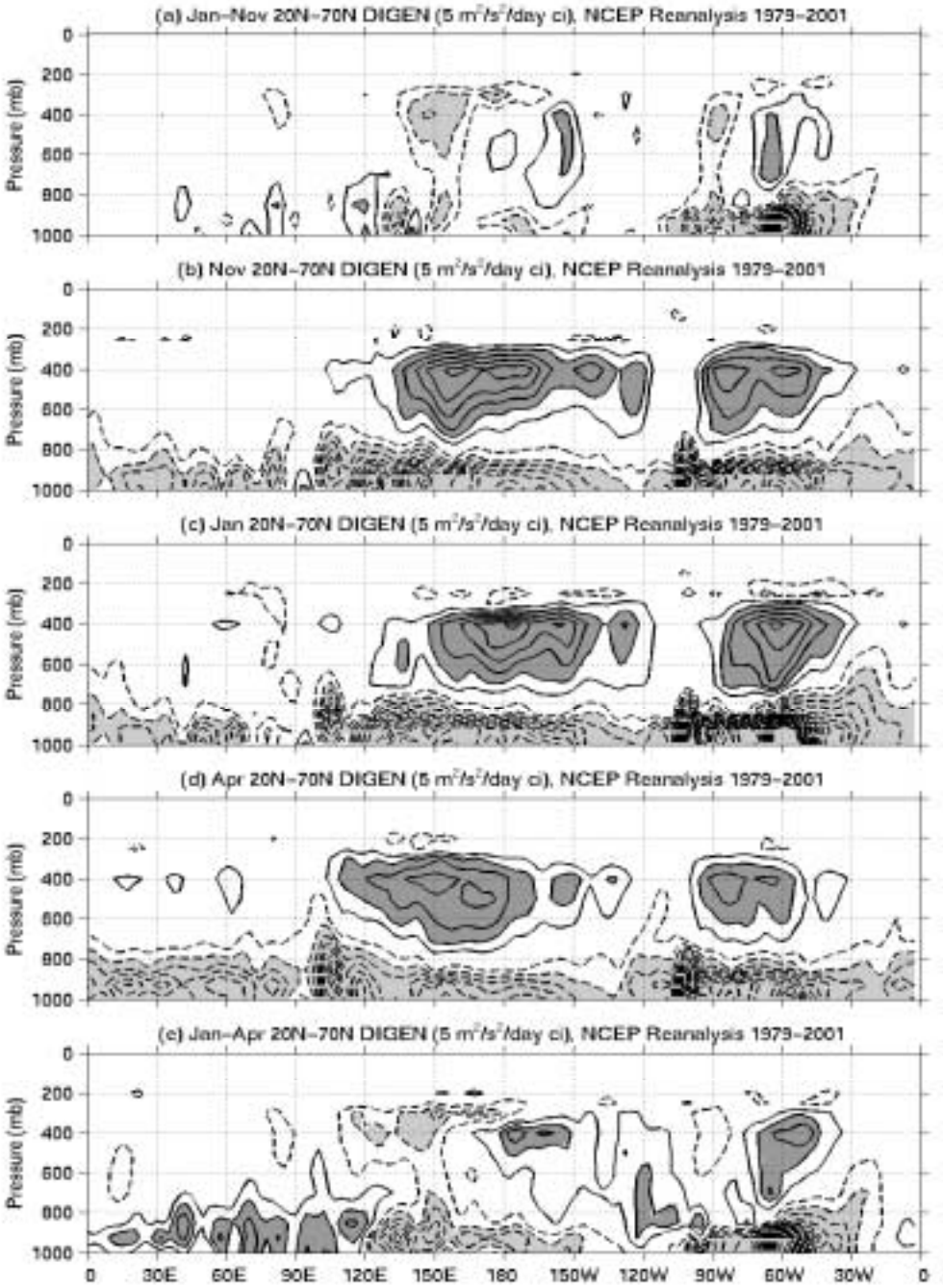

Figure 3.7: Mass-weighted average of $DIGEN$ between $20°$N and $70°$N, for (a) January$-$November, (b) November, (c) January, (d) April, (e) January$-$April. In all panels, the contour interval is 5 m^2/s^2/day, with dashed negative contours and the zero contour omitted; light shading indicates values less than -10 m^2/s^2/day, and dark shading indicates values greater than 10 m^2/s^2/day. $DIGEN$ is calculated as a residual in the eddy APE budget, based on NCEP Reanalysis data from September 1979 to August 2001.

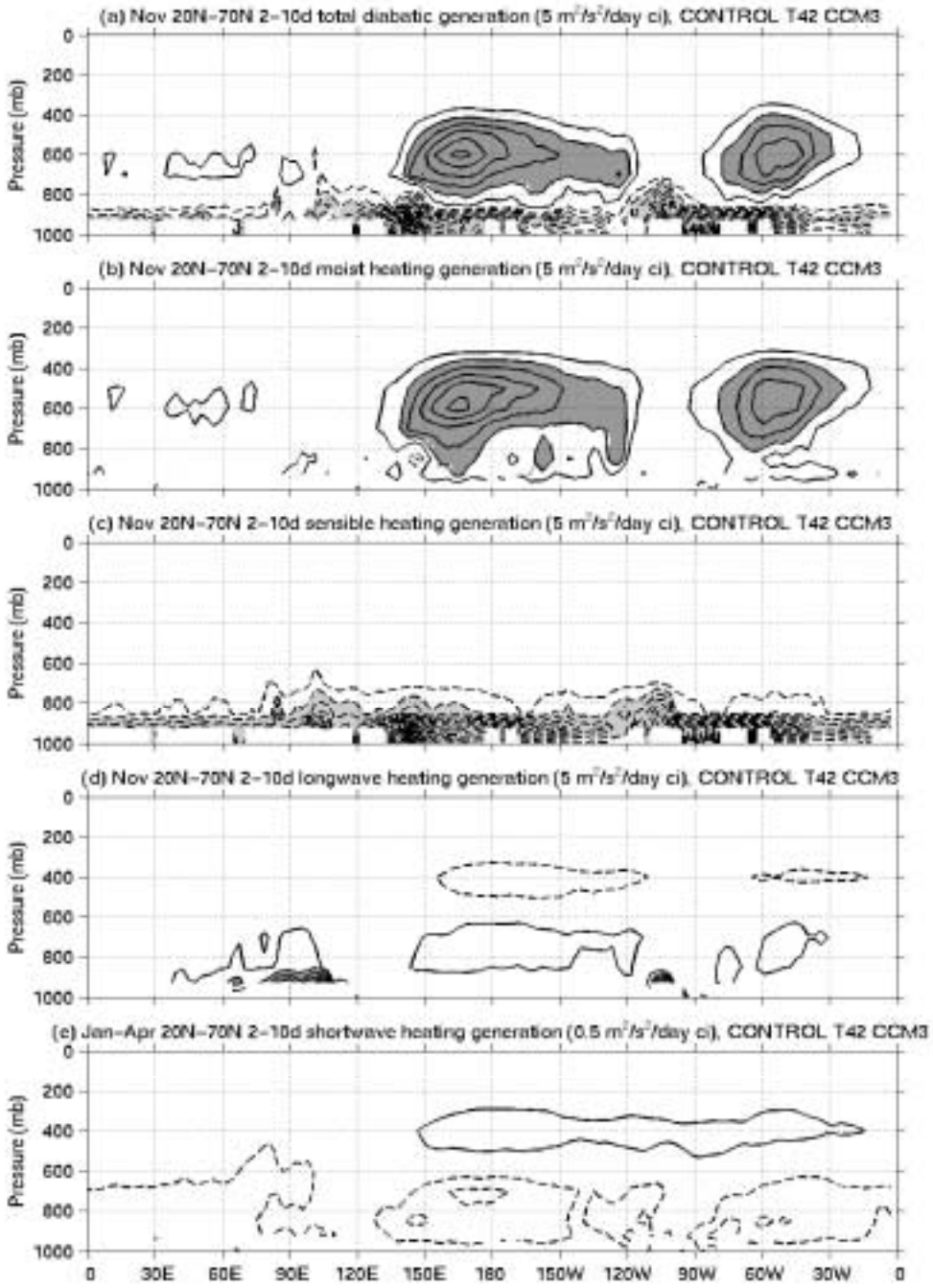

Figure 3.8: Mass-weighted average of components of $DIGEN$ between 20°N and 70°N for November of a control GCM experiment using the NCAR CCM3.6: (a) total diabatic generation, (b) moist heating, (c) sensible heating, (d) longwave heating, (e) shortwave heating. In panels (a)–(d), the contour interval is 5 m^2/s^2/day, with dashed negative contours and the zero contour omitted; light shading indicates values less than -10 m^2/s^2/day, and dark shading indicates values greater than 10 m^2/s^2/day. In panel (e), the contour interval is 0.5 m^2/s^2/day for the much smaller shortwave heating term, again with dashed negative contours and the zero contour omitted. The total and components of $DIGEN$ are calculated directly from the diabatic heating terms and averaged over the last 20 years of a 35-year control experiment of the NCAR CCM3.6.

indicates that $LHGEN$ is smaller in January than in November throughout the middle troposphere from $135°$E to $165°$E, while it appears to shift to a slightly lower altitude in January between $165°$E and $165°$W. Fig. 3.7e shows that $LHGEN$ is also smaller in January than in April between $110°$E and $160°$E, while it appears to shift to a slightly lower level in January between $160°$E and $170°$W.

Fig. 3.9 shows longitude-pressure cross sections of $BCGEN_v$. We note that $BCGEN_v$ is dominated by negative values between the surface and 500 mb, because the relatively cold surface temperatures in winter increase the stability over that of the standard atmosphere. At $120°$E near the Asian coast, the low-level stability is considerably larger in January and November than in April, when the continent has been warmed by spring insolation, so ϵ_{BCCON} will be smaller near the Asian coast in January and November. This could explain at least part of the reduction in eddy KE over the Asian coast in January and November relative to April. Near $150°$E, however, the cold continental air blowing over the relatively warm ocean surface actually decreases the stability at low levels in January relative to April and, to a lesser degree, November, so ϵ_{BCCON} will be larger in January near the surface in this region. Since $BCCON$ at upper levels is more effective at producing persistent eddy KE, the negative values of $BCGEN_v$ near 400 mb over the Pacific in January are of the greatest interest. These negative values result from the increased stability in the region where the tropopause is lower in January relative to April and, to a lesser degree, relative to November. As a result, ϵ_{BCCON} is smaller at upper levels over the Pacific in January than in April or November, which could explain at least part of the midwinter suppression over the central Pacific. Comparing Fig. 3.9a to Fig. 3.7a, $BCGEN_v$ appears to have a smaller effect than $LHGEN$ on the difference in ϵ_{BCCON} between November and January. Fig. 3.9e and Fig. 3.7e show that these terms appear to have approximately equal influence on the difference in ϵ_{BCCON} between January and April, at least at upper levels where $BCCON$ is more likely to produce persistent eddy KE.

Fig. 3.10 shows $BCCON$, the amount of eddy KE produced by vertical motion. Because $BCGEN_v$ tends to reduce ϵ_{BCCON} at low levels, while $LHGEN$ tends to increase

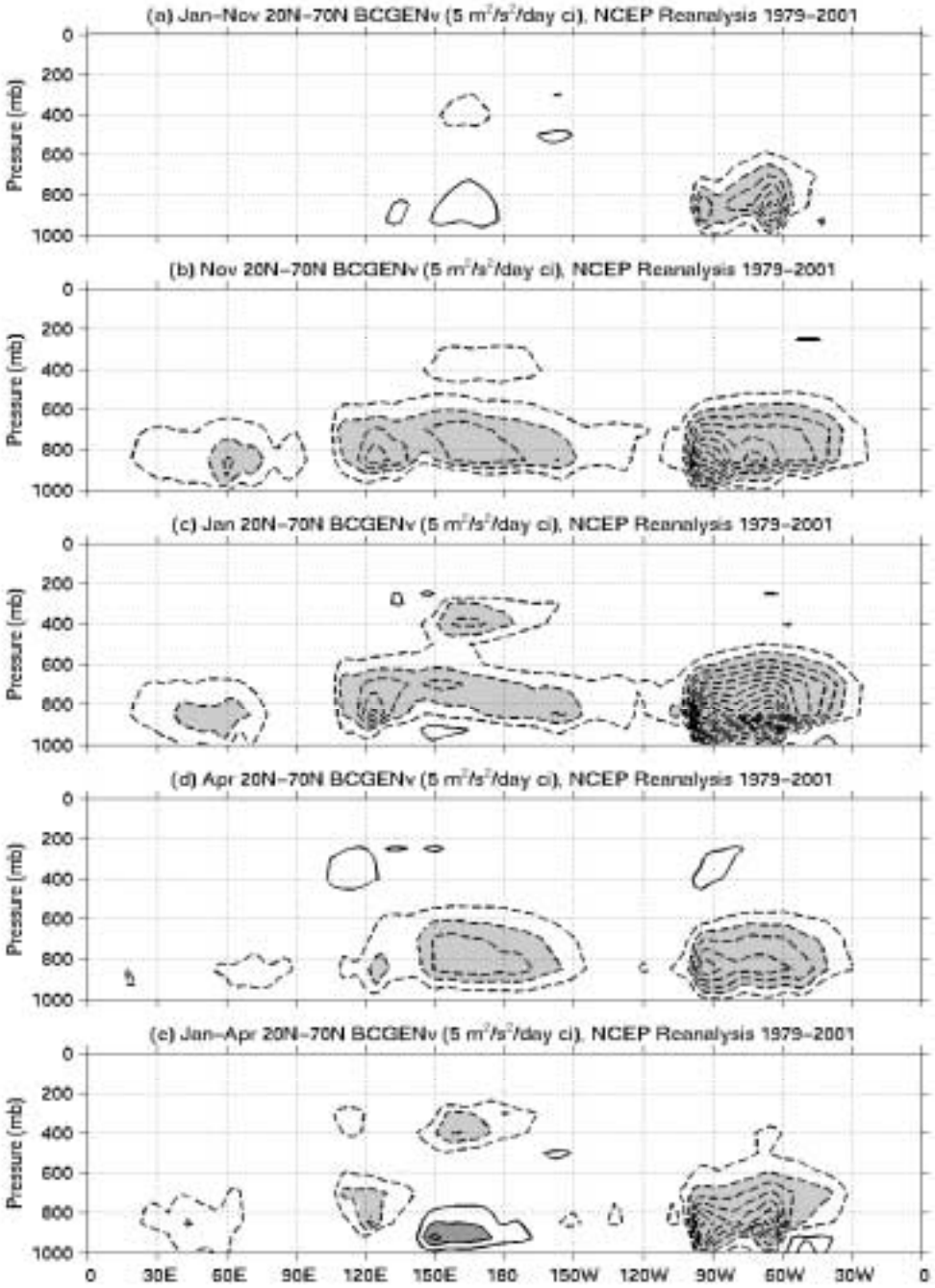

Figure 3.9: Mass-weighted average of $BCGEN_v$ between $20°$N and $70°$N, for (a) January$-$November, (b) November, (c) January, (d) April, (e) January$-$April. In all panels, the contour interval is 5 m^2/s^2/day, with dashed negative contours and the zero contour omitted; light shading indicates values less than -10 m^2/s^2/day, and dark shading indicates values greater than 10 m^2/s^2/day. Calculations are based on NCEP Reanalysis data from September 1979 to August 2001.

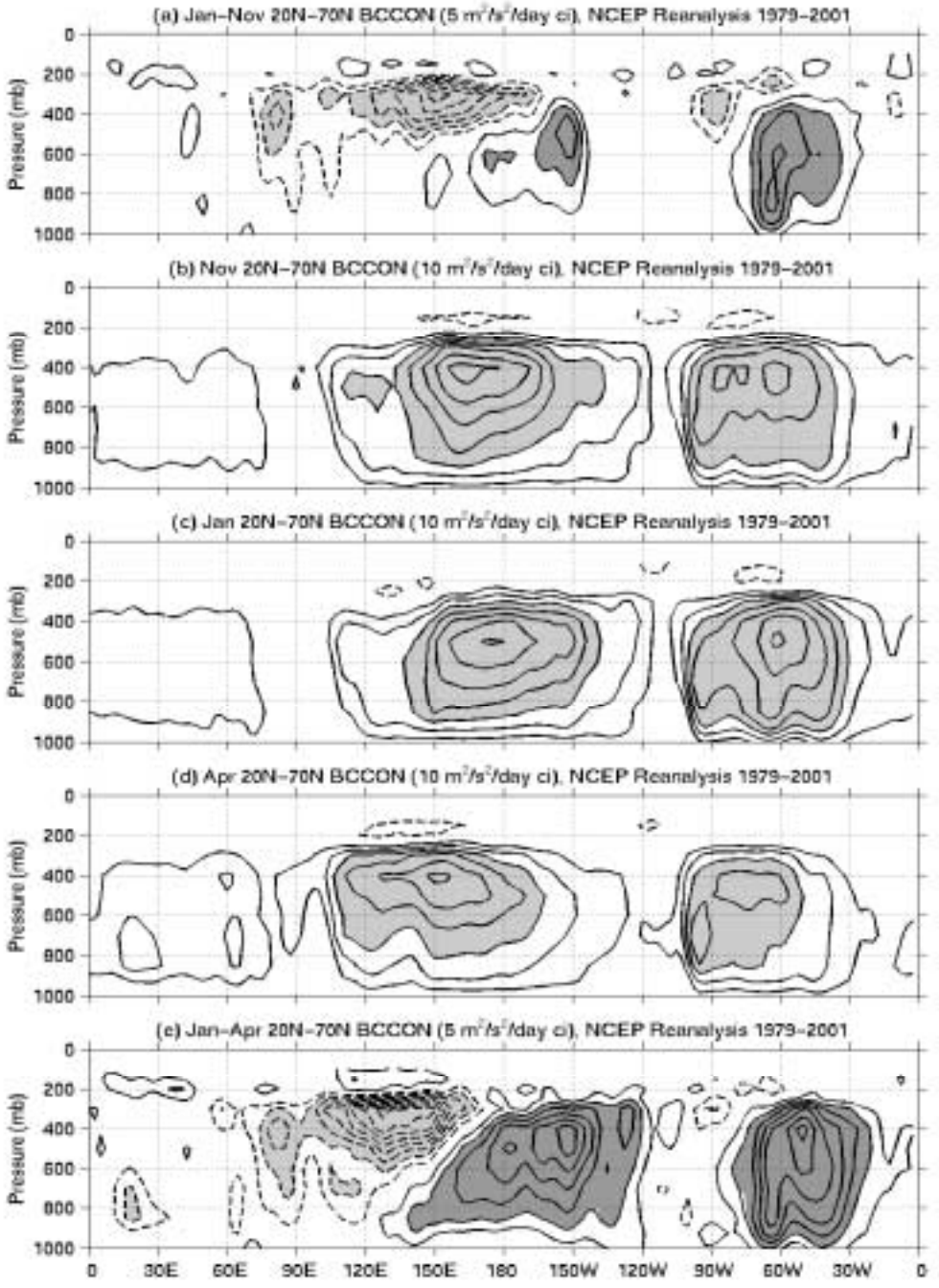

Figure 3.10: Mass-weighted average of $BCCON$ between $20°$N and $70°$N, for (a) January$-$November, (b) November, (c) January, (d) April, (e) January$-$April. In panels (a) and (e), the contour interval is 5 m^2/s^2/day, with dashed negative contours and the zero contour omitted; light shading indicates values less than -10 m^2/s^2/day, and dark shading indicates values greater than 10 m^2/s^2/day. In panels (b)–(d), the contour interval is 10 m^2/s^2/day; shading indicates values greater than 30 m^2/s^2/day. Calculations are based on NCEP Reanalysis data from September 1979 to August 2001.

ϵ_{BCCON} at upper levels, $BCCON$ tends to occur at higher levels than $BCGEN_{eff}$. Comparing Figs. 3.10a and e to Figs. 3.4a and e, the reduced ϵ_{BCCON} at upper levels in January magnifies the deficiencies in the rate of APE production by $BCGEN_{eff}$ in January to produce even larger deficiencies in the rate of eddy KE production by $BCCON$ that are shifted $10 - 20^{\circ}$ longitude downstream. This suggests that $LHGEN$ and $BCGEN_v$ are contributing to the midwinter suppression by decreasing ϵ_{BCCON} at upper levels.

In order to quantify the overall effect of $LHGEN$ and $BCGEN_v$ on the efficiency of baroclinic conversion, we need to know how much more or less eddy KE is produced by $BCCON$ because of these terms. We will assume that, if eddy APE were not consumed by negative values of $BCGEN_v$, it would be available to produce eddy KE through $BCCON$, so $BCGEN_v$ reduces the amount of eddy KE produced by a factor of

$$f_{BCGENv} = \frac{\langle BCCON \rangle_V}{\langle BCCON - BCGEN_v \rangle_V}, \tag{3.9}$$

where V is again the volume where most of the midwinter suppression is forced; f_{BCGENv} has values of 0.82, 0.82, and 0.88 for November, January, and April, respectively. This indicates that $BCGEN_v$ has essentially no effect on the January $-$ November difference in ϵ_{BCCON}, while $BCGEN_v$ decreases ϵ_{BCCON} by a factor of $0.82/0.88 = 0.93$ in January relative to April. We also assume that, if $LHGEN$ did not produce eddy APE to offset some of the eddy APE consumed by vertical motion, the eddy APE produced by $LHGEN$ would not be available to be converted to eddy KE through $BCCON$, so $LHGEN$ increases the amount of eddy KE produced by a factor of

$$f_{LHGEN} = \frac{\langle BCCON \rangle_V}{\langle BCCON - LHGEN \rangle_V}. \tag{3.10}$$

f_{LHGEN} has values of 1.25, 1.19, and 1.28 for November, January, and April, respectively. As expected, $LHGEN$ increases ϵ_{BCCON} by the smallest amount in January; the changes in $LHGEN$ reduce ϵ_{BCCON} in January by a factor of 0.95 relative to November and 0.93 relative to April. This confirms the result that midwinter changes in $LHGEN$ and $BCGEN_v$ are of roughly equal importance in reducing ϵ_{BCCON} relative to April, while only $LHGEN$ is important in reducing ϵ_{BCCON} relative to November.

3.3.3 Vertical redistribution of eddy KE

The vertical motion that converts eddy APE to eddy KE through $BCCON$ (see Fig. 3.10) also transports eddy KE by $AGEO_v$, which is shown in Fig. 3.11. As shown schematically in Fig. 3.3, $AGEO_v$ transports eddy KE from the middle troposphere, where it is produced by $BCCON$, to the upper and lower bounds of the vertical motion. In the Pacific storm track, the altitude of the upper level $AGEO_v$ maximum is lower in January (250-300 mb near the Asian coast, 250 mb over the Pacific) than in November (250 mb near the Asian coast, 200-250 mb over the Pacific) or April (200-250 mb over both the Asian coast and the Pacific), indicating that the upward transport by $AGEO_v$ deposits eddy KE at lower levels in January. This is evident in the dipole between 200 mb and 400 mb in January $-$ November $AGEO_v$ (Fig. 3.10a, $100°$E-$180°$) and January $-$ April $AGEO_v$ (Fig. 3.10e, $100°$E-$165°$E). The ratio of eddy KE converged at upper levels to eddy KE converged at lower levels is smallest in January and largest in April, illustrating the greater tendency for eddy KE to be transported downward when it is produced at lower levels.

Fig. 3.12 shows longitude-pressure cross sections of $KERES$. We divide $KERES$ into two parts: the large negative values from 850 mb down due to $FRIC$, and the smaller, but still mostly negative values from 700 mb up designated as $NFRES$. Turning first to $FRIC$, it appears that the negative values near the surface in Fig. 3.12 approximately cancel the positive $AGEO_v$ near the surface in Fig. 3.11, except in the vicinity of mountains ($90°$E-$120°$E, $120°$W-$90°$W). As illustrated in Fig. 3.3, the eddy KE converged near the surface due to $AGEO_v$ is almost immediately consumed by $FRIC$, while we may assume that much of the eddy KE produced by $BCCON$ in the vicinity of mountains is also consumed by $FRIC$.

We define the amount of eddy KE that persists after being produced and transported by vertical motion as $BCCON_{eff}$, shown in Fig. 3.13. $BCCON_{eff}$ is large only above 500 mb in the storm tracks, and is clearly smaller in the western half of the Pacific storm track in January than in November or April. Figs. 3.13a and e show that the amount of eddy

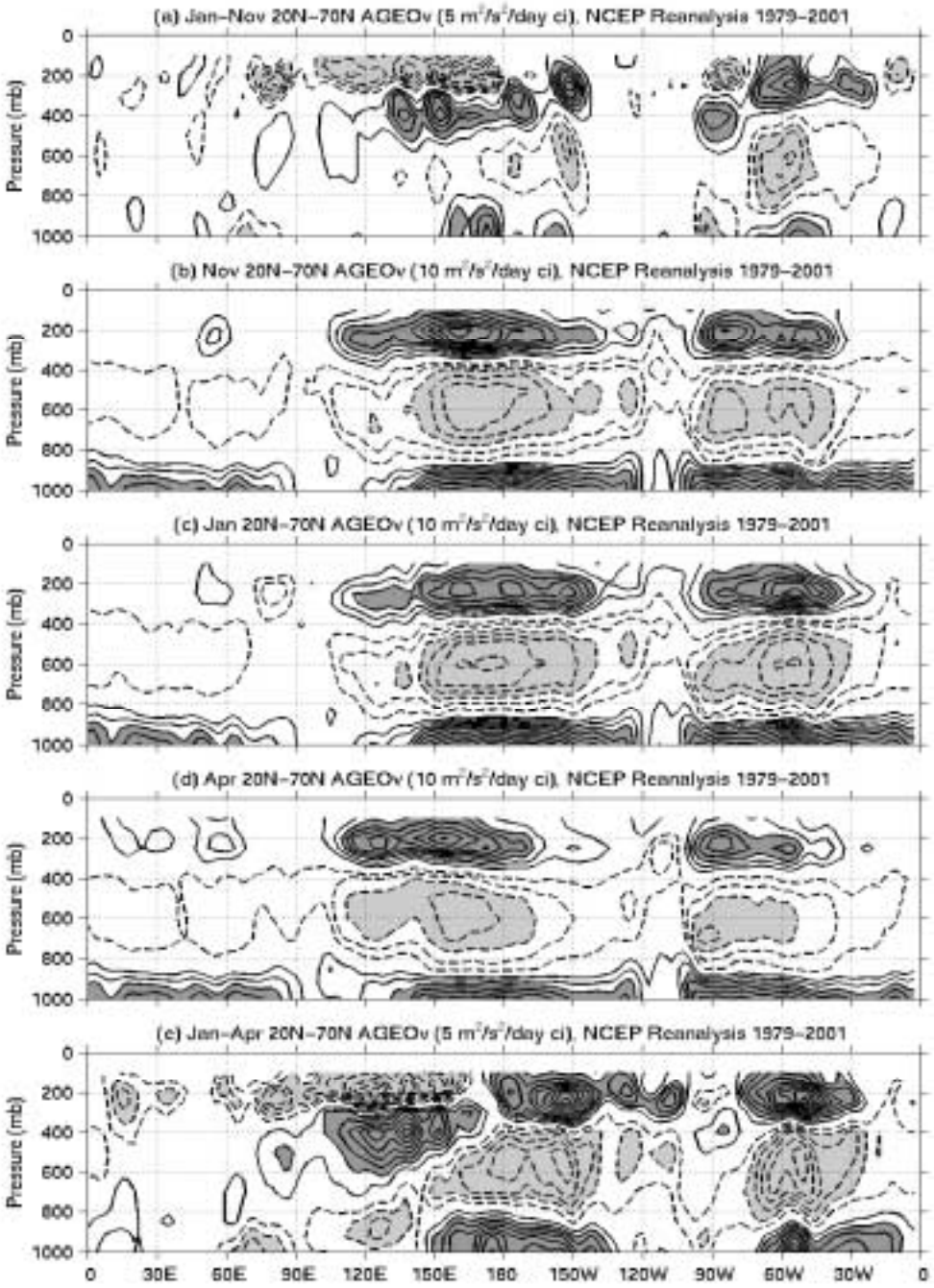

Figure 3.11: Mass-weighted average of $AGEO_v$ between $20°$N and $70°$N, for (a) January$-$November, (b) November, (c) January, (d) April, (e) January$-$April. In panels (a) and (e), the contour interval is 5 m^2/s^2/day, with dashed negative contours and the zero contour omitted; light shading indicates values less than -10 m^2/s^2/day, and dark shading indicates values greater than 10 m^2/s^2/day. In panels (b)–(d), the contour interval is 10 m^2/s^2/day, with dashed negative contours and the zero contour omitted; light shading indicates values less than -30 m^2/s^2/day, and dark shading indicates values greater than 30 m^2/s^2/day. Calculations are based on NCEP Reanalysis data from September 1979 to August 2001.

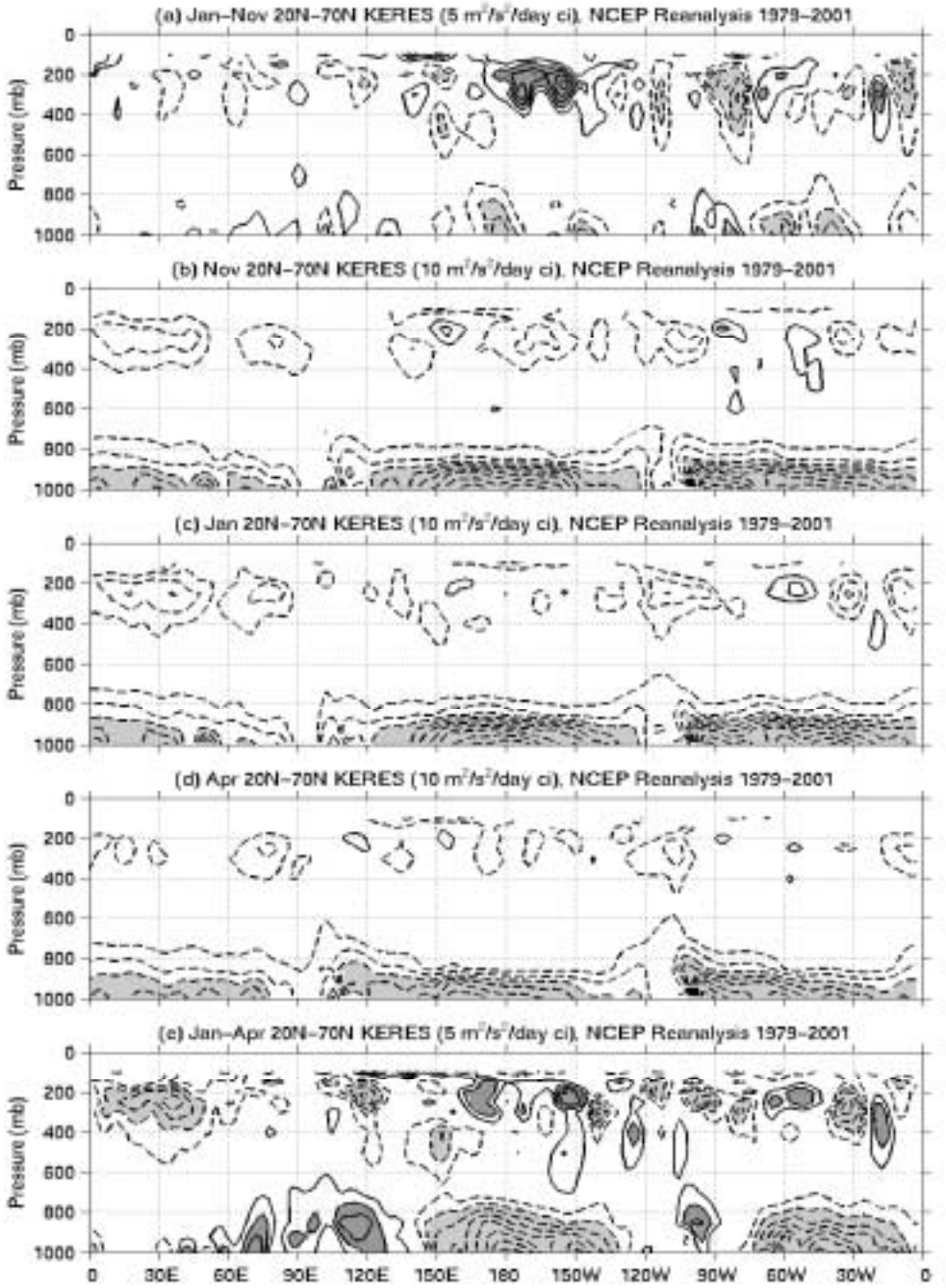

Figure 3.12: Mass-weighted average of $KERES$ between $20°$N and $70°$N, for (a) January−November, (b) November, (c) January, (d) April, (e) January−April. In panels (a) and (e), the contour interval is 5 m^2/s^2/day, with dashed negative contours and the zero contour omitted; light shading indicates values less than -10 m^2/s^2/day, and dark shading indicates values greater than 10 m^2/s^2/day. In panels (b)–(d), the contour interval is 10 m^2/s^2/day, with dashed negative contours and the zero contour omitted; light shading indicates values less than -30 m^2/s^2/day. $KERES$ is calculated as a residual in the eddy KE budget, based on NCEP Reanalysis data from September 1979 to August 2001.

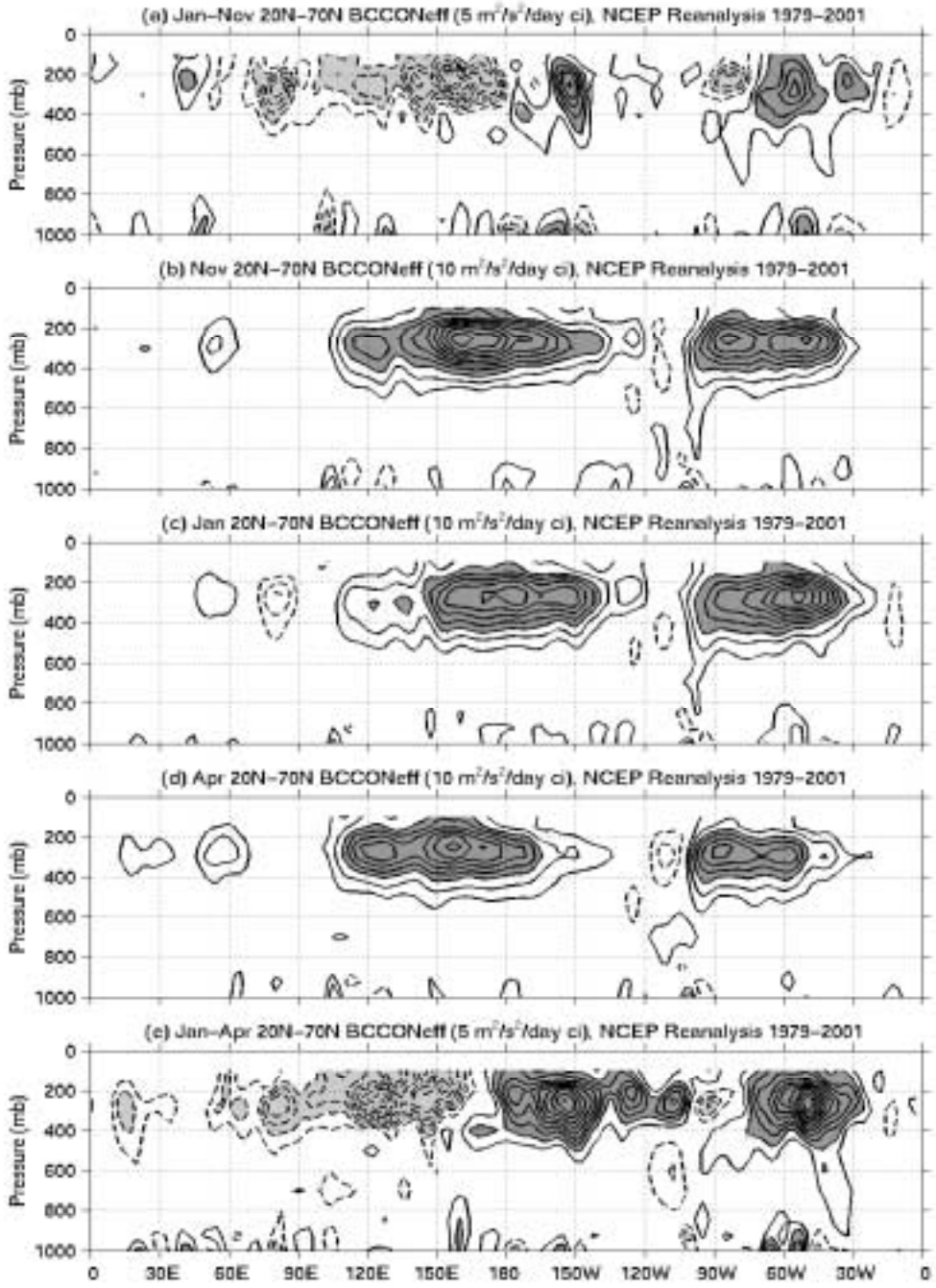

Figure 3.13: Mass-weighted average of $BCCON_{eff}$ between $20°$N and $70°$N, for (a) January−November, (b) November, (c) January, (d) April, (e) January−April. In panels (a) and (e), the contour interval is 5 m^2/s^2/day, with dashed negative contours and the zero contour omitted; light shading indicates values less than -10 m^2/s^2/day, and dark shading indicates values greater than 10 m^2/s^2/day. In panels (b)–(d), the contour interval is 10 m^2/s^2/day, with dashed negative contours and the zero contour omitted; dark shading indicates values greater than 30 m^2/s^2/day. Calculations are based on NCEP Reanalysis data from September 1979 to August 2001.

KE delivered to upper levels in January is less than that in November between $140°$E and $180°$, and less than that in April between $110°$E and $165°$E. A comparison of Figs. 3.13a and e to Figs. 3.10a and e shows that the effects of $AGEO_v$ and $FRIC$ tend to vertically integrate the differences in $BCCON$ and concentrate them near 250 mb, with a greater weight placed on eddy KE produced by $BCCON$ at higher levels. This illustrates that decreases in $BCCON$ at higher levels are more effective at causing the midwinter suppression of the Pacific storm track than increases in $BCCON$ at lower levels are at counteracting it.

In order to assess the combined effect of $AGEO_v$ and $FRIC$ on the efficiency of eddy KE delivery to upper levels, we calculate ϵ_{FRIC}, the factor by which $FRIC$ reduces the amount of eddy KE that persists. Averaging over the volume V where the midwinter suppression is forced, ϵ_{FRIC} has values of 0.68, 0.61, and 0.70 for November, January, and April, respectively. Thus, the fraction of eddy KE that persists in January is reduced by a factor of 0.89 relative to November and 0.86 relative to January, indicating that the processes that cause $BCGEN_h$ and $BCCON$ to be shallower in January have an important impact on the midwinter suppression of the Pacific storm track.

3.3.4 Remaining energy budget terms

We have examined the remaining eddy energy budget terms ($PADV$, $KADV$, $AGEO_h$, $BTCON$, and $NFRES$) and found little evidence that any of these terms enhances the midwinter suppression of the Pacific storm track. $PADV$ (not shown) and $NFRES$ (upper levels of Fig. 3.12) are relatively small and have no systematic difference between November, January, and April. January $-$ November and January $-$ April differences in $KADV$ and $AGEO_h$ (not shown) tend to be positive over the western Pacific and negative farther downstream, indicating that they carry the negative eddy KE anomalies downstream, but do not play a primary role in forcing the suppression. $BTCON$ (not shown) is more positive over the western Pacific in January than in November or April, because the eddies there are propagating up a larger zonal wind gradient, so $BTCON$ plays an active role in counteracting, rather than forcing, the midwinter suppression. Thus, the processes that act

Table 3.1: Summary of factors that reduce the efficiency of eddy energy production and delivery to upper levels. The first column shows the January/November ratio of the efficiency, and the second column shows the January/April ratio of the efficiency. The first row shows the effect of eddy structure on baroclinic generation efficiency, the second shows the effect of moist heating on baroclinic conversion efficiency, the third shows the effect of static stability on baroclinic conversion efficiency, and the fourth shows the effect of the shallowing of $BCGEN_h$ and $BCCON$ on the fraction of eddy KE that persists.

Factor	Jan/Nov	Jan/Apr
Eddy structure	0.86	0.84
Moist heating	0.95	0.93
Static stability	1.00	0.93
Shallowing	0.89	0.86

on eddy KE and APE after they reach upper levels do not appear to force the midwinter suppression of the Pacific storm track.

3.3.5 Quantification of changes in eddy energy budget

We have shown that midwinter changes in eddy structure, moist heating, static stability, and the depth of baroclinic generation and conversion all act to reduce the efficiency with which eddy energy is produced and delivered to upper levels. The effects of these four factors are summarized in Table 3.1.

Because these four factors act in series on the flow of eddy energy, from the production of eddy APE by $BCGEN_h$ through the delivery of eddy KE to upper levels by $AGEO_v$, a reduction in efficiency of 0.9 in any one factor will have a comparable effect on the total efficiency to a reduction in efficiency of 0.9 in any other factor. Table 3.1 shows that changes in eddy structure and the shallowing of $BCGEN_h$ and $BCCON$ play approximately equal roles in reducing the efficiency of eddy KE production relative to both November and April. The combined effects of moist heating and static stability have a comparable effect to ei-

ther of the two other factors in the reduction in eddy energy production efficiency relative to April, while they are less important to the reduction in efficiency relative to November. We note that the reductions in efficiency are generally larger when compared to April, reflecting the larger increases in baroclinicity and barotropic conversion that must be overcome to produce the suppression.

3.4 Summary

Our eddy energy budget analysis has shown that changes in the efficiency of eddy energy production appear to be largely responsible for the midwinter suppression of the Pacific storm track, while advection and other processes that affect eddy KE after it arrives at upper levels are unlikely to force the suppression. The factors which produce the midwinter suppression of the Pacific storm track are as follows: Changes in baroclinic wave structure decrease the efficiency of baroclinic generation of eddy APE; increased static stability and reduced moisture decrease the efficiency of baroclinic conversion from eddy APE to eddy KE; and a greater fraction of eddy KE is produced at lower levels and quickly destroyed by friction. While our eddy energy budget analysis has shown us where the midwinter suppression is being forced in the eddy energy cycle, the cause and form of the changes in eddy structure which cause a large part of the suppression are still unclear. We shall use lag regression analysis in Chapter 4 to investigate these changes in eddy structure.

Chapter 4

LAG REGRESSION ANALYSIS OF BAROCLINIC WAVE STRUCTURE

To this point, we have calculated the statistics of 2–10 day transient eddies in bulk, as if eddy energy can be thought of as growing, propagating, and decaying in infinitesimal parcels without any particular structure. However, the 2–10 day transient eddy statistics are dominated by baroclinic waves, which typically have structures extending from the surface into the lower stratosphere, and are organized into eastward-propagating wave packets (e.g., Chang 1993) which typically span 90° or more of longitude, so the statistics of these baroclinic waves will undoubtedly be influenced by this structure. In this chapter, we use lag regression analysis to study how and why the structure of baroclinic waves changes in January relative to November and April, and how these changes in structure may reduce the efficiency of eddy energy production to drive the midwinter suppression of the Pacific storm track.

4.1 Technique for lag regression analysis

As in previous chapters, the data used are NCEP Reanalysis daily averages from September 1979 to August 2001. Regressions were calculated separately for each 30-day "month" (e.g., "November" is Nov 2-Dec 1, "January" is Jan 1-Jan 30, and "April" is Apr 1-Apr 30), using essentially the technique of Lim and Wallace (1991): The regression coefficient $b(i)$ for a particular variable at a particular pressure level, latitude, and longitude is calculated

as

$$b(i) = \frac{\sum_{t=1}^{N} y'_t(i)x'_t}{\left(\sum_{t=1}^{N} x'^2_t\right)^{\frac{1}{2}}} \tag{4.1}$$

where $y_t(i)$ is the time series of the variable at the specified pressure level, latitude, and longitude; x_t is the reference time series; primes denote departures from 30-day period means; and N is the total number of daily averages available for the 30-day "month". As explained by Chang (1993), temporal filtering can produce "ringing" in the time domain and obscure the downstream development of baroclinic waves, so we use unfiltered data for both the reference time series and the time series of the variables regressed on the reference time series. In this chapter, we use meridional wind (v') at 925 mb in the baroclinic regions of the Pacific storm track as our reference time series x'_t for the regressions, as we have found that regressions on 925 mb v' effectively capture developing baroclinic waves. Lag regressions from day -5 to day +5 are calculated by shifting the time series $y'_t(i)$ by up to 5 days in the appropriate direction.

4.2 Effects of baroclinic wave structure on baroclinic generation efficiency

We start by looking at growing baroclinic waves in longitude-pressure cross sections of lag regressions based on 925 mb v' at $42.5°$N, $120°$E near the Asian coast (point A) and $37.5°$N, $155°$E in the strong SST gradient of the Kuroshio (point K). Both points are near local maxima in low-level baroclinicity in November, January, and April (see Fig. 2.16). Regressions on point A capture the life cycles of baroclinic waves across the western part of the Pacific storm track ($100°$E-$180°$), where changes in the baroclinic generation of eddy APE (see Fig. 3.4), baroclinic conversion of eddy APE to eddy KE (see Fig. 3.10), and delivery of eddy KE to upper levels (see Fig. 3.13) are important in forcing the midwinter suppression; regressions on point K capture baroclinic waves growing in the region of strong baroclinicity in the western Pacific and propagating away from the region of suppression. Fig. 4.1

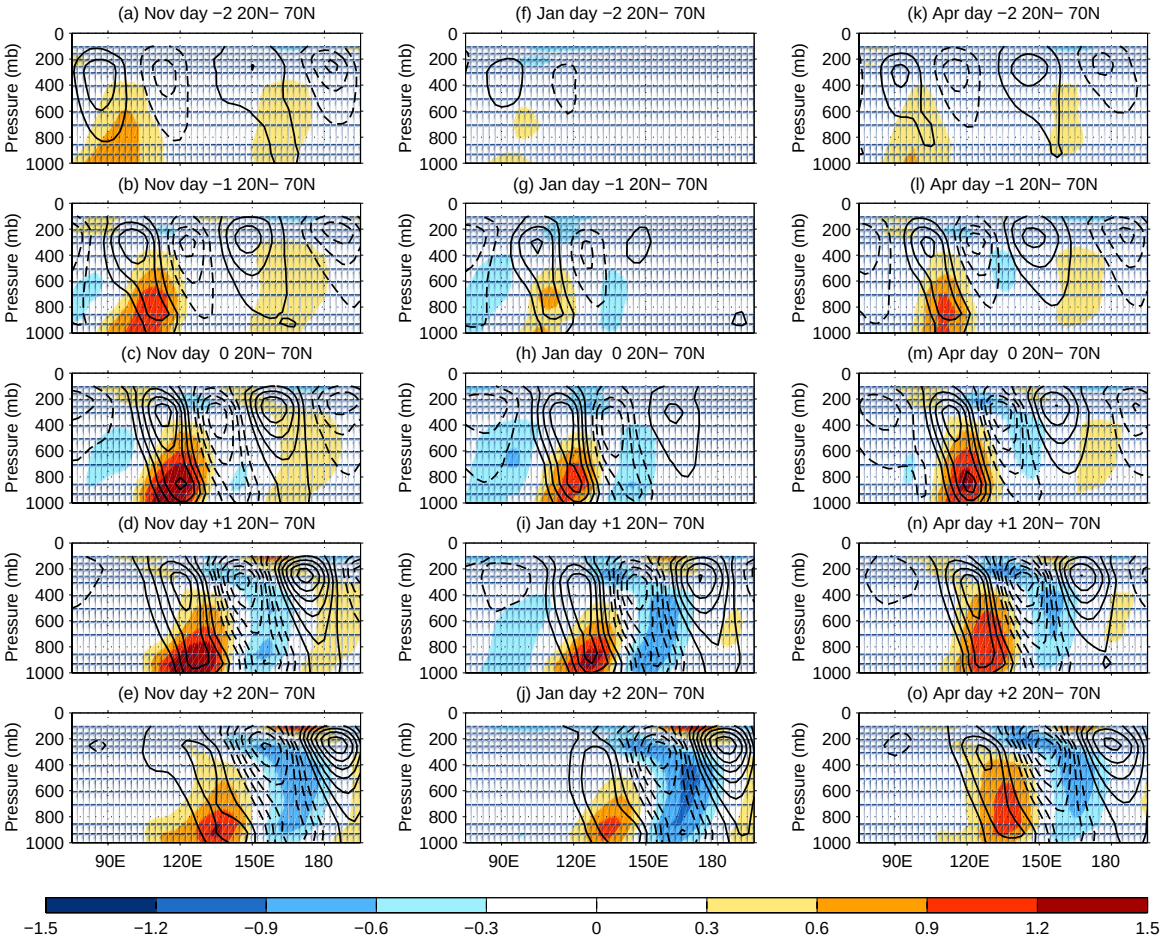

Figure 4.1: Regressions of θ' (color) and v' (contours) on 925 mb v' at $120°$E, $42.5°$N. Quantities shown are mass-weighted averages between $20°$N and $70°$N at lags day -2 through day +2, for (a)–(e) November, (f)–(j) January, (k)–(o) April. The contour interval for v' is 0.5 m/s, while the color contour interval for θ' is 0.3 K. Calculations are based on NCEP Reanalysis data from September 1979 to August 2001.

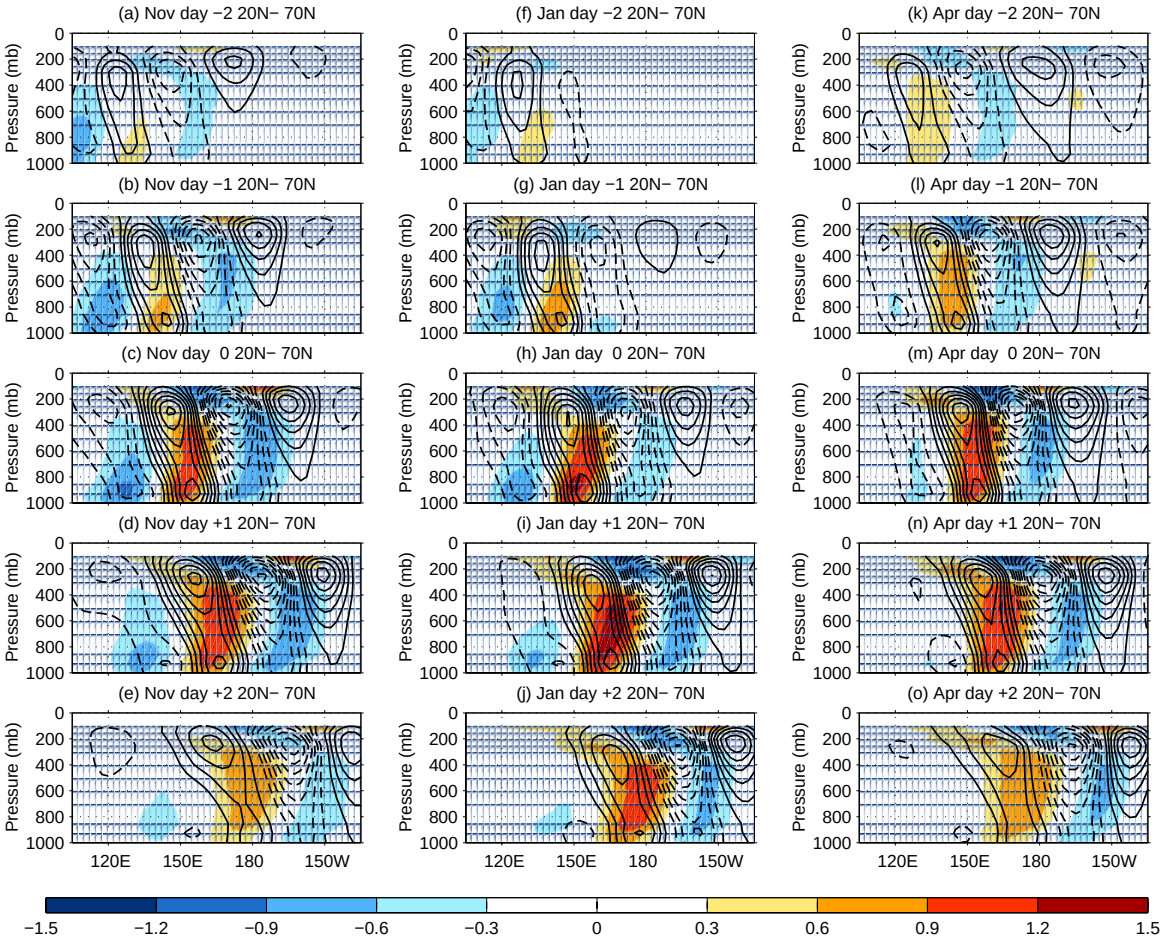

Figure 4.2: Regressions of θ' (color) and v' (contours) on 925 mb v' at $155°$E, $37.5°$N. Quantities shown are mass-weighted averages between $20°$N and $70°$N at lags day -2 through day +2, for (a)–(e) November, (f)–(j) January, (k)–(o) April. The contour interval for v' is 0.5 m/s, while the color contour interval for θ' is 0.3 K. Calculations are based on NCEP Reanalysis data from September 1979 to August 2001.

shows longitude-pressure cross sections of v' (in contours) and potential temperature (θ', in color) regressed on v' at point A for lags from day -2 to day +2, averaged from $20°$N to $70°$N; Fig. 4.2 shows the same for regressions based on point K. The baroclinic wave structure shown in Fig. 4.2 fits the classic picture of baroclinic waves: v' tilts westward with height, and increases with height where θ' is positive, while θ' is forced by v', but tilts eastward with height because of the greater influence of advection by the mean zonal wind ($\overline{u}$) at higher levels. v' and θ' in Fig. 4.2 resemble the baroclinic wave structure found by Lim and Wallace (1991) and Chang (1993), but with slightly larger amplitudes at lower levels because our reference time series is 925 mb v', rather than 500 mb geopotential height (z') or 300 mb v' as in the previous studies. We will find that the baroclinic wave structure shown for November and January differs from the classic picture of baroclinic waves in ways that are related to the midwinter suppression.

We note two major differences among the baroclinic wave structures for November, January, and April. First, in Fig. 4.1, θ' is much shallower in January than in November or April, with little amplitude above 500 mb until day +1 east of $150°$E. In Fig. 4.2, θ' also appears to be shallower in January than in November or April as far east as the date line, but to a lesser degree. In both Figs. 4.1 and 4.2, θ' appears to be shallower in November than in April between $120°$E and $150°$E as well, but to a much lesser degree than January. Second, θ' has a larger eastward tilt with height in November and January than in April; this is more evident in Fig. 4.1, but is also present in Fig. 4.2. We note that v' has a greater westward tilt with height where θ' is strong, because positive v' must be located to the west of the positive z' which grows on top of positive θ', so v' has a larger tilt where θ' influences z'; this is particularly clear in Fig. 4.2. Hence, a larger eastward tilt of θ' does not necessarily mean that it is less correlated with v'. We are particularly interested in the depth and tilt of θ' with respect to v' because the correlation of v' with θ', represented by the parameter k_{ED} in section 3.3.1, affects the efficiency of the baroclinic generation of eddy APE ($BCGEN_h$). We now examine the relative structures of v' and θ' shown in Figs. 4.1 and 4.2 to explain the effects of k_{ED} on $BCGEN_{hy}$, the dominant meridional term in $BCGEN_h$.

We first look to explain the effect of the January $-$ November difference in k_{ED} on $BCGEN_{hy}$, shown in Fig. 3.5a. The reduction in $BCGEN_{hy}$ is largest above 400 mb, centered near $150°$E; west of $150°$E, the reduction is almost all above 400 mb, while it expands down to the surface east of $150°$E. We note that, in Figs. 4.1 and 4.2, θ' does not have significant amplitude above 400 mb in January west of $150°$E, so the smaller correlation of v' and θ' west of $150°$E must be due to the shallower θ'; this reduced correlation is explained by the small values and reversal in the sign of θ' above the primary θ' perturbation extending from the surface. Between $150°$E and $180°$, θ' still has little amplitude above 300 mb in January, so the upper level reduction in $BCGEN_{hy}$ due to k_{ED} at these longitudes must also be due to the shallower θ'. However, the regressions from day 0 to day +2 in Fig. 4.2 show that θ' does appear to have a larger eastward tilt in January than in November between $150°$E and $180°$, so the reduction in $BCGEN_{hy}$ due to k_{ED} below 400 mb is likely due to the greater relative tilt between v' and θ'. Since changes in $BCGEN_{hy}$ at higher levels are more likely to produce changes in eddy KE, and the largest changes in $BCGEN_{hy}$ are above 400 mb, changes in the depth of θ' are probably more important for causing the midwinter suppression than changes in the tilt of θ', but both depth and tilt appear to have a noticeable effect on $BCGEN_{hy}$.

We now examine the effect of the November $-$ April difference in k_{ED} on $BCGEN_{hy}$, shown in Fig. 4.3. We first note that the reduction in $BCGEN_{hy}$ is smaller and shallower than for the January $-$ November difference in k_{ED}, and, in fact, $BCGEN_{hy}$ is larger due to the November k_{ED} east of $150°$E. The reason for the increase in $BCGEN_{hy}$ east of $150°$E is not clear, but it may be because the stronger temperature gradient in November ties θ' more closely to v' than in April. The reason for the reduction in $BCGEN_{hy}$ in the middle troposphere from $110°$E to $150°$E is most clearly illustrated by the regressions for day +1 and day +2 in Fig. 4.1: the positive θ' has a much larger eastward tilt in November than in April, while the tilt of v' is approximately the same. We expect the large difference in tilt between January and April to have the same effect, which explains the large vertical extent of the reduction in $BCGEN_{hy}$ due to the January $-$ April difference in k_{ED} (see Fig. 3.5e);

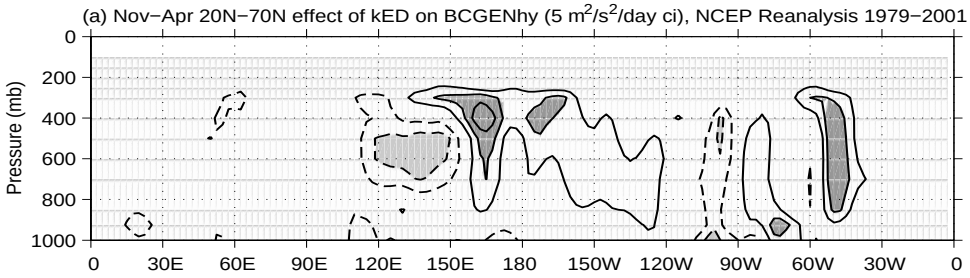

Figure 4.3: November−April difference in mass-weighted average of $BCGEN_{hy}$ between $20°$N and $70°$N, calculated using eddy structure parameter k_{ED} for November or April and all other parameters set to their January values. The contour interval is 5 m^2/s^2/day, with dashed negative contours and the zero contour omitted; light shading indicates values less than -10 m^2/s^2/day, and dark shading indicates values greater than 10 m^2/s^2/day. Calculations are based on NCEP Reanalysis data from September 1979 to August 2001.

we assume that the differences below 400 mb are primarily due to the tilt of θ', while the differences above 400 mb are primarily due to the depth of θ'. Although the depth and tilt have approximately equal effects on the January − April difference in $BCGEN_h$, the depth of θ' is probably still more important for forcing the midwinter suppression relative to spring because of the greater importance of eddy energy generated at upper levels.

4.3 Causes of temperature perturbation structure changes

There are a number of possible explanations for the differences in the depth and tilt of θ' between November, January, and April. In this section, we investigate the changes in the structure of θ' using the eddy temperature budget:

$$\frac{\partial\theta'}{\partial t} = -(\overline{u}+u')\frac{\partial\theta'}{\partial x} - u'\frac{\partial\overline{\theta}}{\partial x} - (\overline{v}+v')\frac{\partial\theta'}{\partial y} - v'\frac{\partial\overline{\theta}}{\partial y} - (\overline{\omega}+\omega')\frac{\partial\theta'}{\partial p} - \omega'\frac{\partial\overline{\theta}}{\partial p} + Q', \quad (4.2)$$

where primes denote values from our lag regressions, overbars indicate monthly means averaged from 1979 to 2001, and the eddy diabatic heating Q' is estimated as a residual. The dominant terms in the eddy temperature budget are $-\overline{u}(\partial\theta'/\partial x)$, $-v'(\partial\overline{\theta}/\partial y)$, $-\omega'(\partial\overline{\theta}/\partial p)$, and Q'. We choose to show each of these terms for the day +1 lag regressions

based on point A, because the differences in θ' between November, January, and April are particularly large at that lag (see Fig. 4.1), but the conclusions based on the figures that we show explain the θ' structure in all of the regressions that we have examined for the Pacific storm track. We first consider the reason for the shallower θ' in January.

We saw in Chapter 2 that during midwinter the upper level baroclinic region (see Fig. 2.17) shifts equatorward relative to the stationary near-surface baroclinic regions (see Fig. 2.16), while we demonstrate in Chapter 5 that baroclinic waves tilt poleward with height. Because θ' is primarily forced by $-v'(\partial\overline{\theta}/\partial y)$, it is possible that the misalignment of v' with $\partial\overline{\theta}/\partial y$ at upper levels causes θ' to be shallower in January. Fig. 4.4 shows a latitude-pressure cross section of v' in contours with $-\partial\overline{\theta}/\partial y$ in color, both averaged over the phase of the baroclinic wave where v' is positive. While $-\partial\overline{\theta}/\partial y$ is smaller poleward of $45°$N in January than in November or April, and the poleward tilt places much of the positive v' poleward of $45°$N, it appears that v' blows across considerably larger $-\partial\overline{\theta}/\partial y$ equatorward of $40°$N in January. Fig. 4.5 confirms this by showing that the temperature forcing by $-v'(\partial\overline{\theta}/\partial y)$ is much larger at upper levels in January than in April, and slightly larger than in November. The larger $-\partial\overline{\theta}/\partial y$ outweighs the slightly smaller spatial correlation between v' and $-\partial\overline{\theta}/\partial y$, so changes in $-v'(\partial\overline{\theta}/\partial y)$ cannot be causing θ' to be shallower in January.

Before examining the effect of vertical temperature advection, we show the regressions of ω' and θ' on v' at point A in Fig. 4.6. The most interesting feature of this figure is that the vertical extent of ω' is constant, from the surface to 200 mb, regardless of the vertical extent of θ'. ω' is also largest in January, despite the small θ' in January, because it is largely driven by $-v'(\partial\overline{\theta}/\partial y)$. We therefore expect that cooling by vertical advection will be large in the vicinity of the tropopause, regardless of the structure of θ'.

Fig. 4.7 shows the temperature forcing by $-\omega'(\partial\overline{\theta}/\partial p)$ for the day +1 lag regressions on point A. As expected, $-\omega'(\partial\overline{\theta}/\partial p)$ is large and negative near the tropopause above positive θ', and it is more negative in January because of the descent of the tropopause. In Figs. 4.7a and e, $-\omega'(\partial\overline{\theta}/\partial p)$ is anomalously negative where θ' is anomalously cold relative

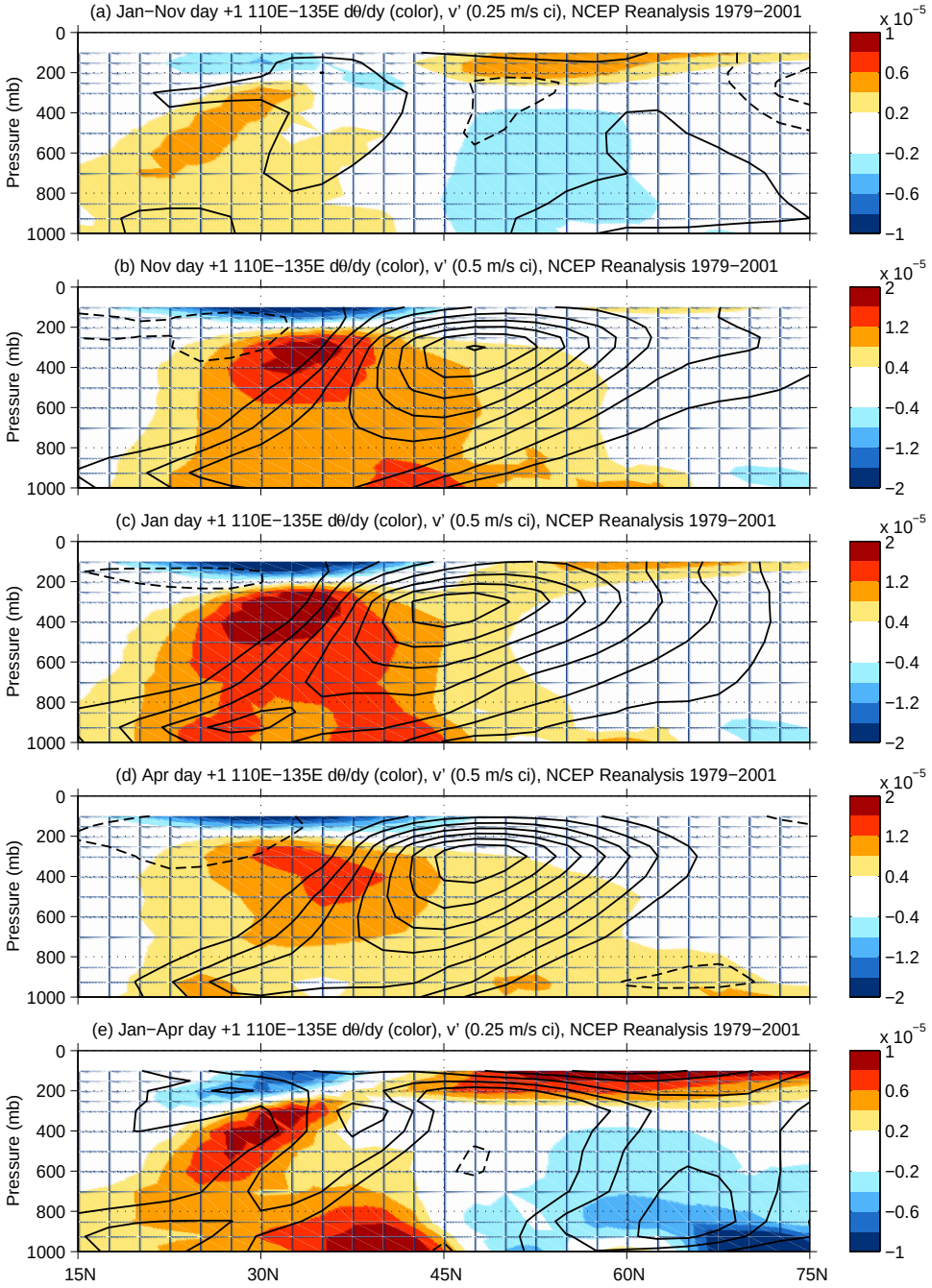

Figure 4.4: $-\partial\overline{\theta}/\partial y$ (color) and regression of v' (contours) on 925 mb v' at $120°$E, $42.5°$N. Quantities shown are mass-weighted averages between $110°$E and $135°$E at day +1 for (a) January$-$November, (b) November, (c) January, (d) April, (e) January$-$April. In panels (a) and (e), the contour interval for v' is 0.25 m/s, while the color contour interval for $-\partial\overline{\theta}/\partial y$ is 2×10^{-6} K/m. In panels (b)-(d), the contour interval for v' is 0.5 m/s, while the color contour interval for $-\partial\overline{\theta}/\partial y$ is 4×10^{-6} K/m. Calculations are based on NCEP Reanalysis data from September 1979 to August 2001.

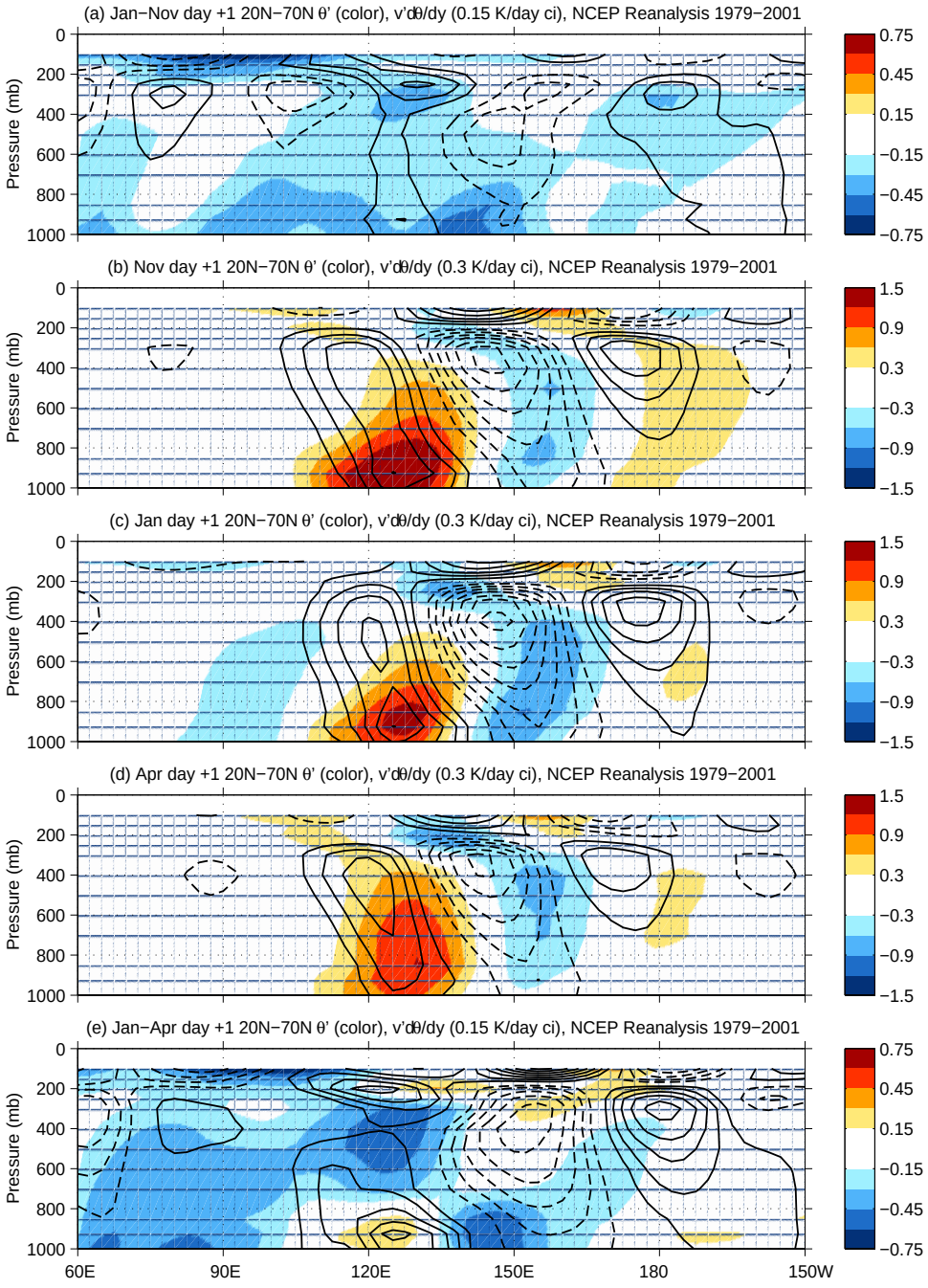

Figure 4.5: Regressions of θ' (color) and $-v'(\partial\overline{\theta}/\partial y)$ (contours) on 925 mb v' at $120°$E, $42.5°$N. Quantities shown are mass-weighted averages between $20°$N and $70°$N at day +1 for (a) January−November, (b) November, (c) January, (d) April, (e) January−April. In panels (a) and (e), the contour interval for $-v'(\partial\overline{\theta}/\partial y)$ is 0.15 K/day, while the color contour interval for θ' is 0.15 K. In panels (b)–(d), the contour interval for $-v'(\partial\overline{\theta}/\partial y)$ is 0.3 K/day, while the color contour interval for θ' is 0.3 K. Calculations are based on NCEP Reanalysis data from September 1979 to August 2001.

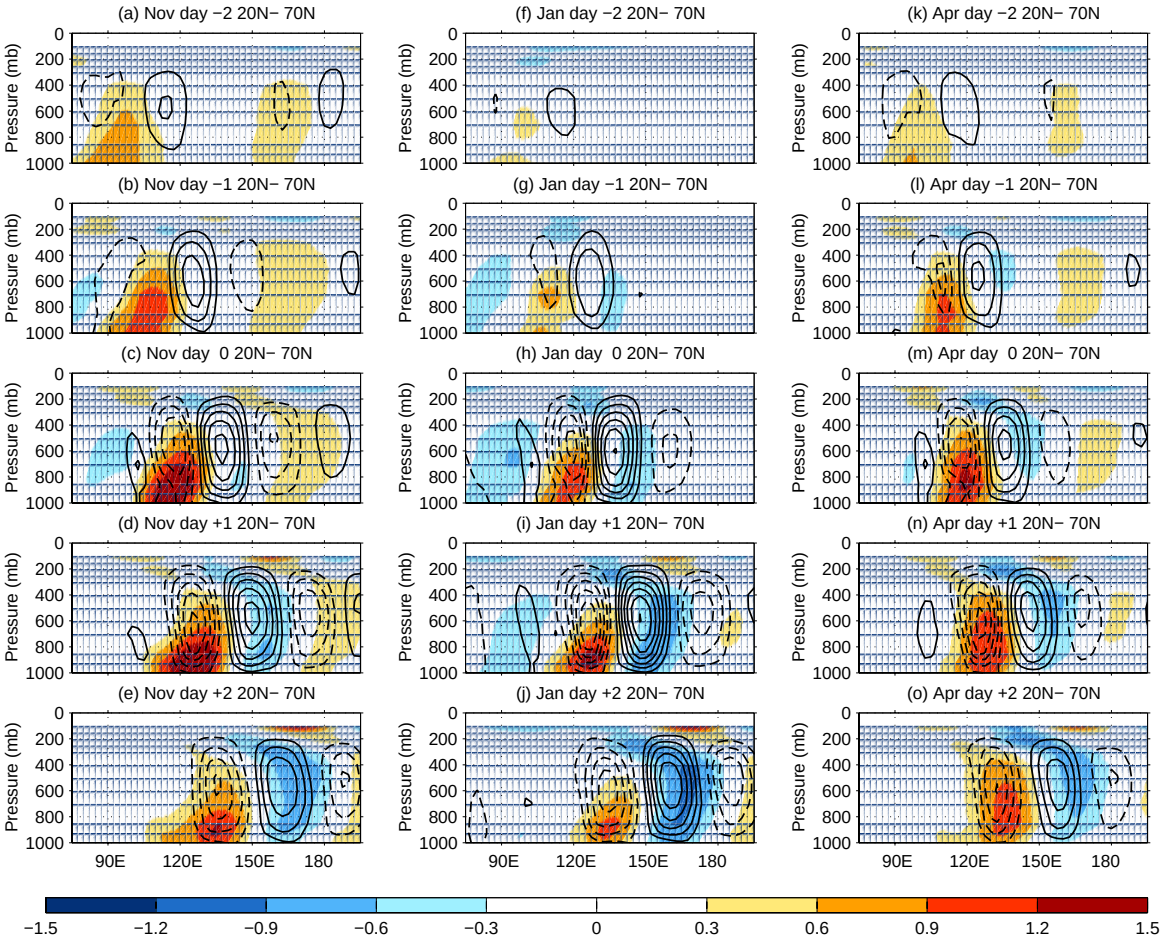

Figure 4.6: Regressions of θ' (color) and ω' (contours) on 925 mb v' at $120°$E, $42.5°$N. Quantities shown are mass-weighted averages between $20°$N and $70°$N at lags day -2 through day +2, for (a)–(e) November, (f)–(j) January, (k)–(o) April. The contour interval for ω' is 0.005 Pa/s, while the color contour interval for θ' is 0.3 K. Calculations are based on NCEP Reanalysis data from September 1979 to August 2001.

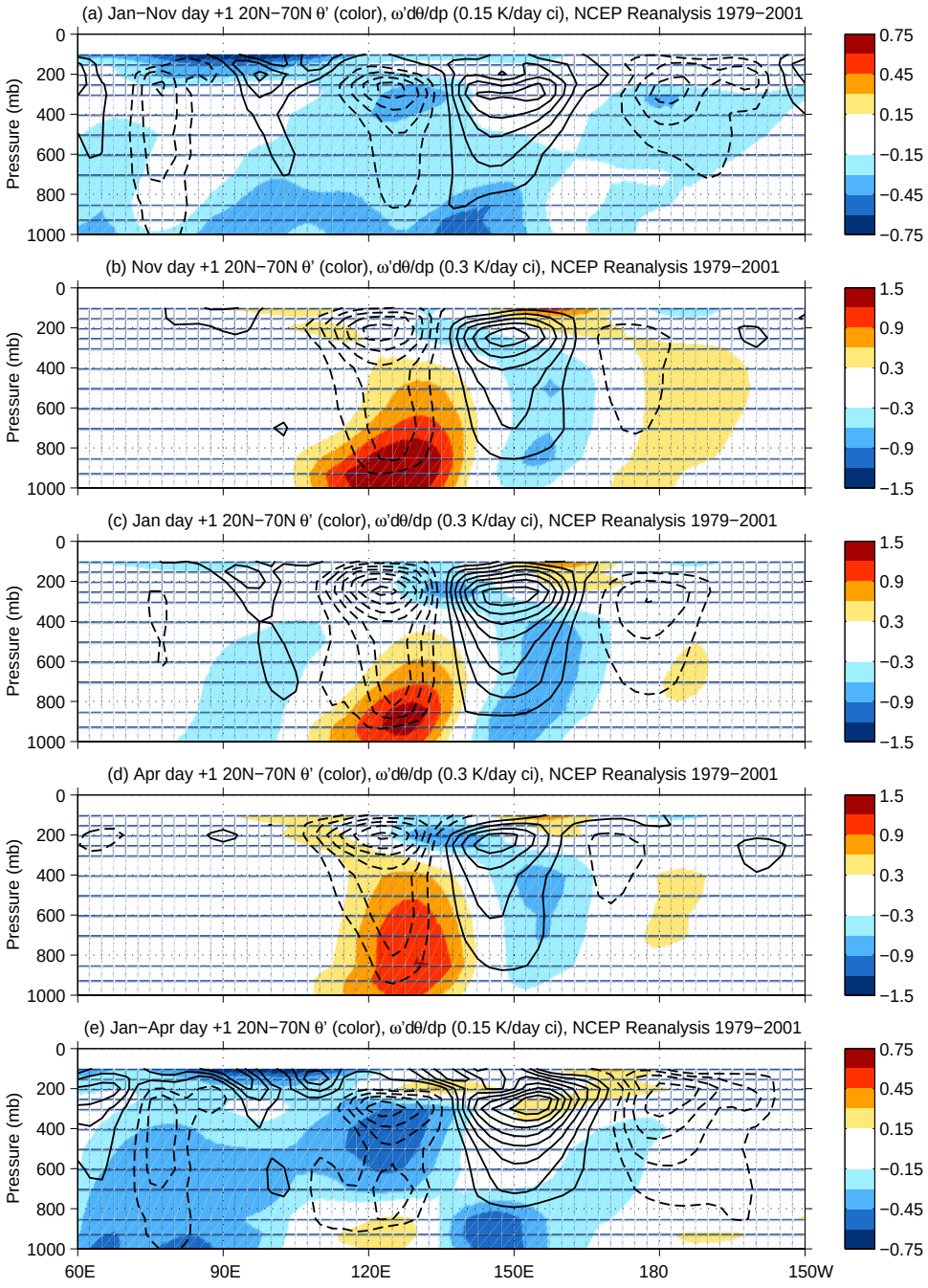

Figure 4.7: Regressions of θ' (color) and $-\omega'(\partial\overline{\theta}/\partial p)$ (contours) on 925 mb v' at $120°$E, $42.5°$N. Quantities shown are mass-weighted averages between $20°$N and $70°$N at day +1 for (a) January$-$November, (b) November, (c) January, (d) April, (e) January$-$April. In panels (a) and (e), the contour interval for $-\omega'(\partial\overline{\theta}/\partial p)$ is 0.15 K/day, while the color contour interval for θ' is 0.15 K. In panels (b)–(d), the contour interval for $-\omega'(\partial\overline{\theta}/\partial p)$ is 0.3 K/day, while the color contour interval for θ' is 0.3 K. Calculations are based on NCEP Reanalysis data from September 1979 to August 2001.

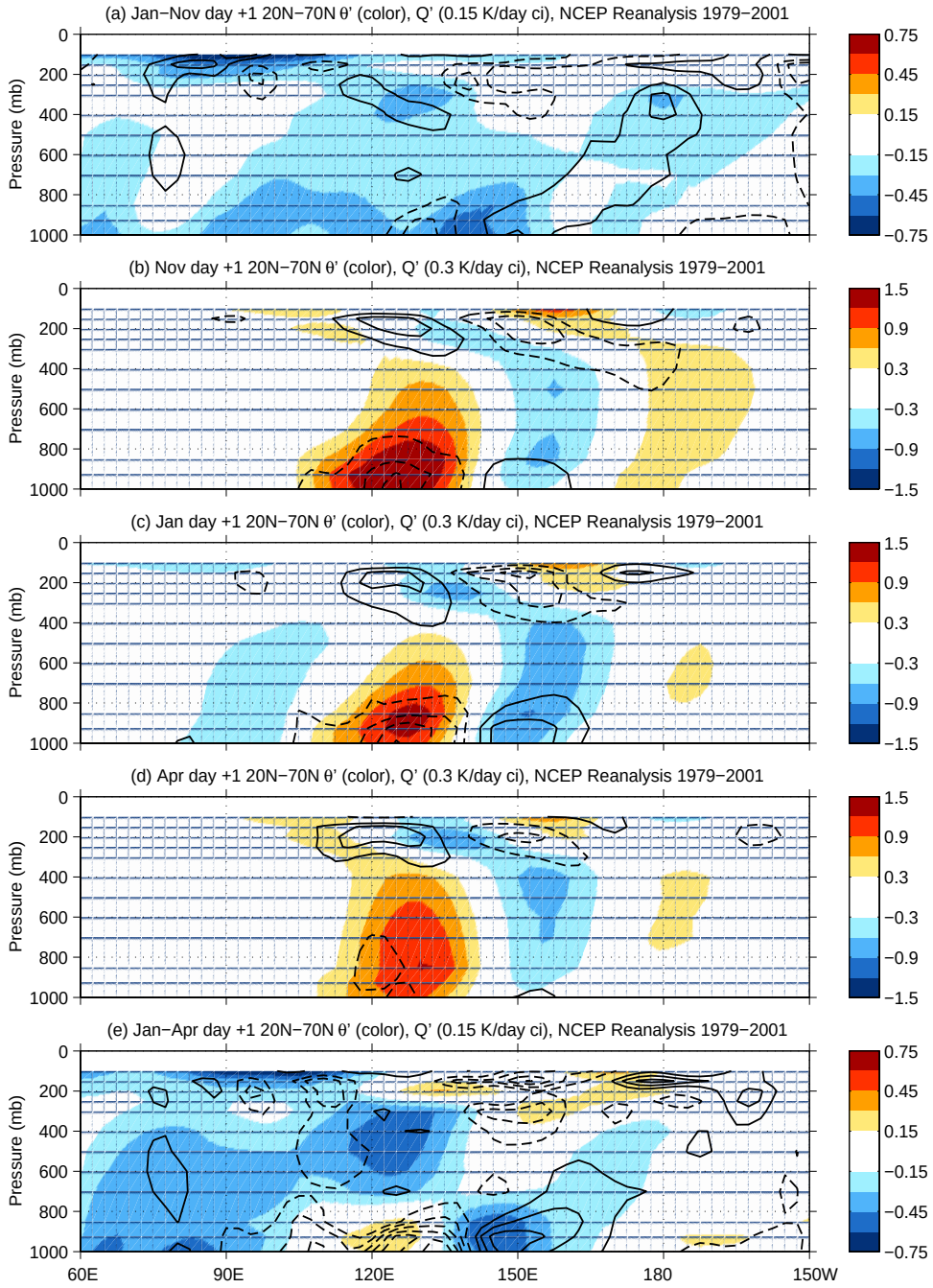

Figure 4.8: Regressions of θ' (color) and Q' (contours) on 925 mb v' at $120°$E, $42.5°$N. Quantities shown are mass-weighted averages between $20°$N and $70°$N at day +1 for (a) January$-$November, (b) November, (c) January, (d) April, (e) January$-$April. In panels (a) and (e), the contour interval for Q' is 0.15 K/day, while the color contour interval for θ' is 0.15 K. In panels (b)–(d), the contour interval for Q' is 0.3 K/day, while the color contour interval for θ' is 0.3 K. Q' is calculated as a residual in the eddy temperature budget, based on daily mean NCEP Reanalysis data from September 1979 to August 2001.

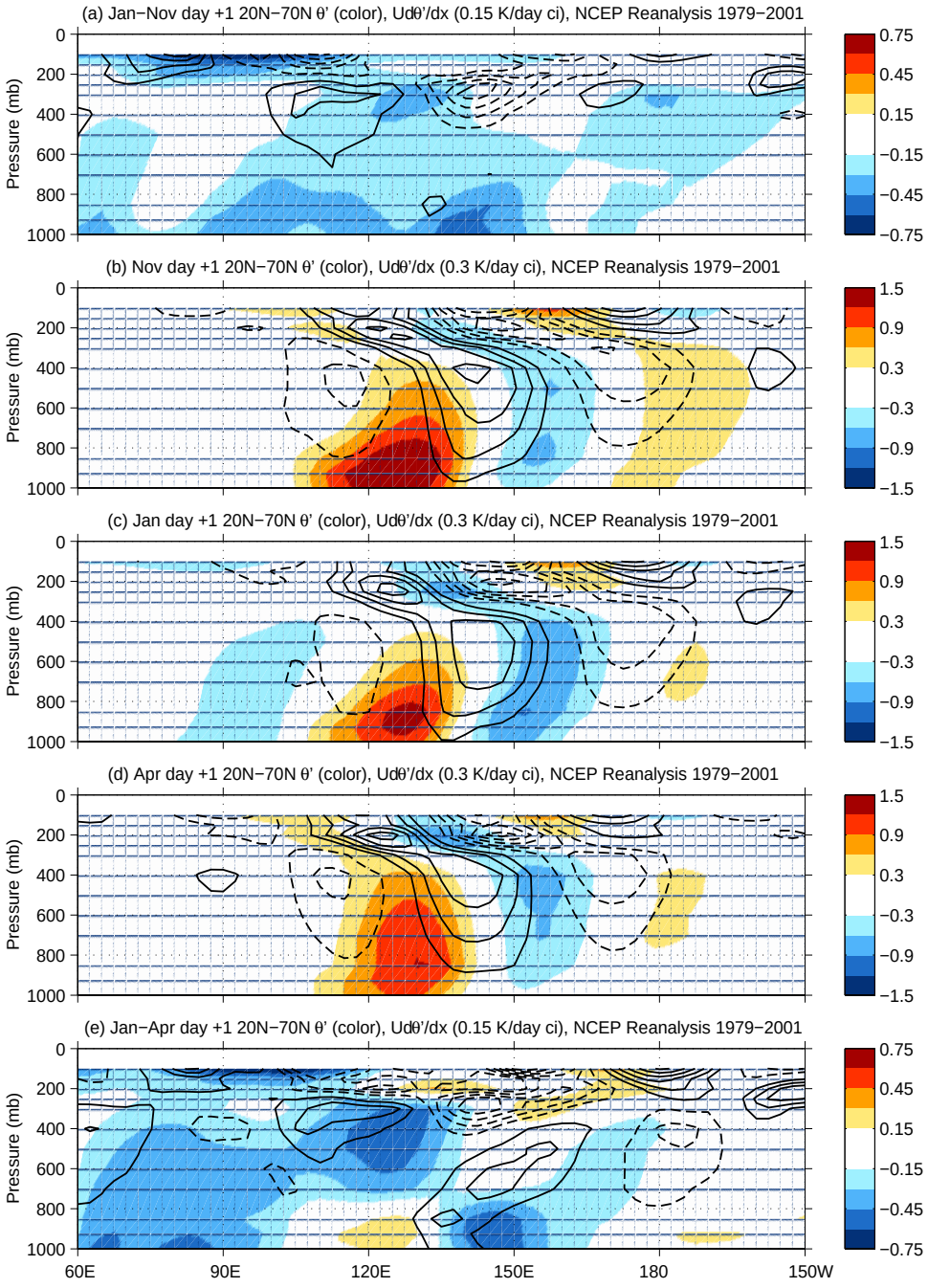

Figure 4.9: Regressions of θ' (color) and $-\overline{u}(\partial\theta'/\partial x)$ (contours) on 925 mb v' at $120°$E, $42.5°$N. Quantities shown are mass-weighted averages between $20°$N and $70°$N at day +1 for (a) January−November, (b) November, (c) January, (d) April, (e) January−April. In panels (a) and (e), the contour interval for $-\overline{u}(\partial\theta'/\partial x)$ is 0.15 K/day, while the color contour interval for θ' is 0.15 K. In panels (b)–(d), the contour interval for $-\overline{u}(\partial\theta'/\partial x)$ is 0.3 K/day, while the color contour interval for θ' is 0.3 K. Calculations are based on NCEP Reanalysis data from September 1979 to August 2001.

to November and April. This shows that the descent of the tropopause in January increases the damping of θ' at upper levels and causes θ' to be shallower than in November or April.

Reduced latent heating could also explain the shallower θ' in January; Fig. 4.8 shows the diabatic heating, Q', calculated as a residual from the day +1 lag regressions on point A. The damping of θ' by sensible heat fluxes is seen near the surface, but one surprising feature is that nearly all of the Q' associated with latent heating occurs above 400 mb. This explains why $LHGEN$ is centered near the highest level reached by θ': it is only at this level that Q' and θ' are positively correlated so that Q' reinforces θ'. The reason for the high altitude of the Q' from moist heating is unclear, but it is possible that the heat from condensation is deposited at the highest point reached by the vertical motion, or that the only part of the moist heating that is correlated with v' occurs at levels above the bulk of the mean moist heating. In any case, Figs. 4.8a and e show that the changes in Q' are too small and of the wrong sign to explain the shallow θ' in January.

The larger $\overline{u}$ in January could also explain the shallowing of θ' if it reduces the upper level $\partial\theta'/\partial x$ in order to maintain balance with the other terms in the eddy temperature budget. Fig. 4.9 shows the temperature forcing by $-\overline{u}(\partial\theta'/\partial x)$ for the day +1 lag regressions on point A. The larger $\overline{u}$ experienced by θ' in November relative to April does appear to be smoothing the upper level θ' field, as $-\overline{u}(\partial\theta'/\partial x)$ remains nearly the same (or slightly larger) while $\partial\theta'/\partial x$ is clearly smaller in November than in April. θ' is advected by a larger $\overline{u}$ in November despite the similar mean $\overline{u}$ between November and April (see Fig. 2.8) because the Pacific jet is shifted poleward in November relative to April (see Fig. 2.9) and is thus closer to the location of the storm track (see Fig. 2.4). In fact, the mean $\overline{u}$ experienced by θ' (not shown) in November and January is quite similar, because the stronger January jet is displaced equatorward, indicating that $\overline{u}$ is unlikely to be responsible for the shallowing of θ' in January relative to November. The smaller $-\overline{u}(\partial\theta'/\partial x)$ in January relative to November and April is additional evidence that $\overline{u}$ does not play a primary role in causing θ' to be shallower in January.

Not surprisingly, the larger $\overline{u}$ in November and January does appear to be responsible

for most of the increase in the eastward tilt of θ' relative to April. The $-\omega'(\partial\overline{\theta}/\partial p)$ in Fig. 4.7 also appears to be positioned correctly to force some of the additional eastward tilt of θ' in January. However, there is little difference in $-\omega'(\partial\overline{\theta}/\partial p)$ between November and April, and θ' has nearly the same tilt in November and January, so we must assume that most of the increased eastward tilt in November and January is due to $\overline{u}$ rather than $-\omega'(\partial\overline{\theta}/\partial p)$.

4.4 Summary

We conclude that the increase in $\overline{u}$ causes most of the increased midwinter tilt of θ', which is responsible for approximately half of the January $-$ April decrease in the efficiency of baroclinic generation due to baroclinic wave structure, and somewhat less than half of the January $-$ November decrease in this efficiency. The increase in static stability in the region where the tropopause is lower causes most of the shallowing of θ', which is responsible for the remaining half or more of the midwinter decrease in the efficiency of baroclinic generation due to baroclinic wave structure. The shallowing of θ' must also be responsible for the shallower baroclinic generation and baroclinic conversion in midwinter, so the lowering of the tropopause in midwinter causes a larger fraction of eddy KE to be consumed by friction as well. In addition, the lowering of the tropopause is responsible for most of the reduced efficiency of baroclinic conversion due to increased static stability (see Fig. 3.9). Since at least half of the effect of eddy structure, most of the effect of static stability, and essentially all of the effect of shallowing on the efficiency of eddy energy production can be attributed to the lowering of the tropopause in midwinter, the values in Table 3.1 indicate that the lowering of the tropopause is responsible for over half of the reduction in efficiency of eddy energy production that drives the midwinter suppression of the Pacific storm track. Reduced moisture and stronger jets appear to play small supporting roles in enhancing the suppression.

We note that the poleward tilt with height of baroclinic waves, illustrated in Fig. 4.4,

explains why the maximum in upper level eddy energy is located on the poleward side of the jet, as the baroclinic waves tilt poleward from the near-surface baroclinic region. This shift, in turn, enables the increased static stability near the lower tropopause on the poleward side of the Pacific jet to more effectively suppress the storm track in midwinter. We devote the following chapter to demonstrating and explaining the poleward tilt with height of baroclinic waves.

Chapter 5

WHY DO BAROCLINIC WAVES TILT POLEWARD WITH HEIGHT?

5.1 Introduction

Most previous studies of the observed structure of baroclinic waves have focused on their structure in the longitude-latitude plane (e.g., Blackmon et al. 1984) or the longitude-height plane (e.g., Lim and Wallace 1991, Chang 1993). It is well-known that baroclinic waves tilt westward with height. However, little attention has been paid to the structure of baroclinic waves in the latitude-height plane. While the regression analysis of Chang (2001, Figs. 5 and 8) suggests that meridional wind perturbations in observed baroclinic waves tilt poleward with height by approximately 10° latitude between 850 mb and 250 mb, no mention of this feature was made in the paper.

A close inspection of the literature on baroclinic life cycles reveals evidence that, at least during early stages of their life cycle, simulated baroclinic waves tend to tilt poleward with height. The clearest illustration of this tilt comes from Gall (1977), who shows that the amplitudes of geopotential height and zonal wind perturbations, as well as some eddy fluxes, tilt poleward with height in a baroclinic wave simulated with a primitive equation model. He also points out that this poleward tilt with height is not observed in simulations using a quasigeostrophic model. Snyder et al. (1991) also note a poleward tilt with height of the most unstable mode in a primitive equation simulation of a baroclinic wave that is not present in the most unstable mode of a semi-geostrophic simulation. A number of other published simulations of baroclinic waves *show* evidence of a poleward tilt with height, through the latitude-height profiles of eddy heat flux (Simmons and Hoskins 1976,

Fig. 15a), eddy KE (Simmons and Hoskins 1978, Fig. 6a), and Eliassen-Palm (EP) flux convergence (Thorncroft et al. 1993, Fig. 15a) of the most unstable baroclinic mode in a primitive equation model, *although none of these studies mention this poleward tilt*. In the above-mentioned figures, the typical poleward tilt with height is approximately 10° latitude from the surface to the 300 mb level.

To our knowledge, the only published explanation for the poleward tilt with height of baroclinic waves is given by Hoskins (1975), who shows that perturbations of geopotential height, geostrophic velocities, and potential temperature in baroclinic waves should tilt poleward with height with a slope that is parallel to the absolute vorticity vector, while total (geostrophic plus ageostrophic) perturbations of meridional wind should have twice this slope. The poleward component of the absolute vorticity vector is approximately equal to the vertical shear of the mean zonal wind $\partial\overline{u}/\partial z$, while the vertical component is approximately equal to the Coriolis parameter f. Hoskins (1975) estimates the slope of the absolute vorticity vector as $U/Hf \approx 30$ using a typical zonal wind speed $U \approx 30$ m/s, a height scale $H \approx 10$ km, and $f \approx 10^{-4}$ s^{-1}. Thus, he estimates that geopotential height perturbations should tilt poleward by about 300 km, or 3° latitude, from the surface to the tropopause, and meridional wind perturbations should tilt poleward by twice as much.

Hoskins (1975) notes that the horizontal ageostrophic wind is implicitly accounted for by the transformation to the tilted vertical coordinate (parallel to the absolute vorticity vector) used in his semi-geostrophic equations. In this chapter, we demonstrate that the temperature advection by the ageostrophic wind produces the poleward tilt with height of baroclinic waves. We also expand on the work of Lim et al. (1991) and Kwon and Lim (1999) to further explain the structure of the ageostrophic wind field in baroclinic waves.

5.2 Data and analysis techniques

As in previous chapters, the data used are NCEP Reanalysis daily averages from September 1979 to August 2001, which were obtained from the NOAA-CIRES Climate Diagnostics

Center website at http://www.cdc.noaa.gov. Regressions were calculated separately for each 30-day "month" (e.g., "November" is Nov 2-Dec 1, "January" is Jan 1-Jan 30, and "April" is Apr 1-Apr 30), using essentially the technique of Lim and Wallace (1991): The regression coefficient $b(i)$ for a particular variable at a particular pressure level, latitude, and longitude is calculated as

$$b(i) = \frac{\sum_{t=1}^{N} y'_t(i) x'_t}{\left(\sum_{t=1}^{N} x'^2_t \right)^{\frac{1}{2}}} \tag{5.1}$$

where $y_t(i)$ is the time series of the variable at the specified pressure level, latitude, and longitude; x_t is the reference time series; primes denote departures from 30-day period means; and N is the total number of daily averages available for the 30-day "month". As explained by Chang (1993), temporal filtering can produce "ringing" in the time domain and obscure the downstream development of baroclinic waves, so we use unfiltered data for both the reference time series and the time series of the variables regressed on the reference time series. In this chapter, we choose meridional wind (v') at 925 mb and $37.5°$N, $155°$E (in the region of strongest baroclinic growth in the Pacific storm track) as our reference time series x'_t, since we have found that regressions on 925 mb v' effectively capture developing baroclinic waves. We also calculate lag regressions from day -5 to day +5 by shifting the time series $y'_t(i)$ by up to 5 days in the appropriate direction. In this chapter, we choose to show figures only for November, which should be more representative of "typical" baroclinic waves than those found in the suppressed Pacific storm track in January or the more weakly forced storm track in April. As we saw in Chapter 4, the structure of baroclinic waves over the Pacific is not very different between November, January, and April, and the tilt of the waves is similar in all three months. For brevity, we also show only the day 0 regressions, which are representative of the regressions at other lags, although the structure of the baroclinic wave begins to change more rapidly in the decay phase of its life cycle during day +1 and day +2.

5.3 Observed structure of baroclinic waves

We begin our examination of the observed structure of baroclinic waves with Fig. 5.1, which shows longitude-height profiles of v', geopotential height (z'), and potential temperature (θ') regressed on our reference time series of 925 mb v' for November and meridionally averaged from $20°$N to $70°$N. These are comparable to Figs. 3 and 7 from Lim and Wallace (1991) and Fig. 7 from Chang (1993), although our regressions have larger amplitude at lower levels because our reference time series is 925 mb v', rather than 500 mb z' or 300 mb v' as in the other studies, respectively. In Fig 5.1, as in previous studies, we see the characteristic westward tilt with height of v' and z', while θ' tilts eastward with height, at least at lower levels, and reverses sign above 300 mb. These perturbations are consistent with each other: v' is approximately proportional to $\partial z'/\partial x$, z' increases with height where θ' is positive, and θ' tends to be positive where v' blows poleward across the meridional temperature gradient $\partial\overline{\theta}/\partial y$ (but reverses sign where $\partial\overline{\theta}/\partial y$ reverses sign above the jet), with some downstream displacement aloft where advection by the mean jet is strong.

Each panel of Fig. 5.1 also has vectors showing the direction of the ageostrophic wind (u'_a,ω') in the meridional plane; the vectors in each panel are the same. We can see that ω' tends to be upward where there is positive meridional temperature advection by positive v'; since θ' essentially arises from meridional temperature advection, this is also where θ' is positive. u'_a is westerly at upper levels where z' is positive and easterly where z' is negative, which results in the downstream propagation of eddy energy through the ageostrophic geopotential flux; u'_a tends to blow from high to low pressure near the surface. The ageostrophic wind forms cells of alternating clockwise and counterclockwise circulation in the longitude-pressure plane. We note that these cells maintain a constant phase relationship with v' and z', but appear to become out of sync with θ' away from the central, positive θ' perturbation.

To examine the poleward tilt with height of baroclinic waves, we show latitude-pressure profiles of v', z', and θ' in Fig. 5.2, each averaged over the half-wavelength of the wave

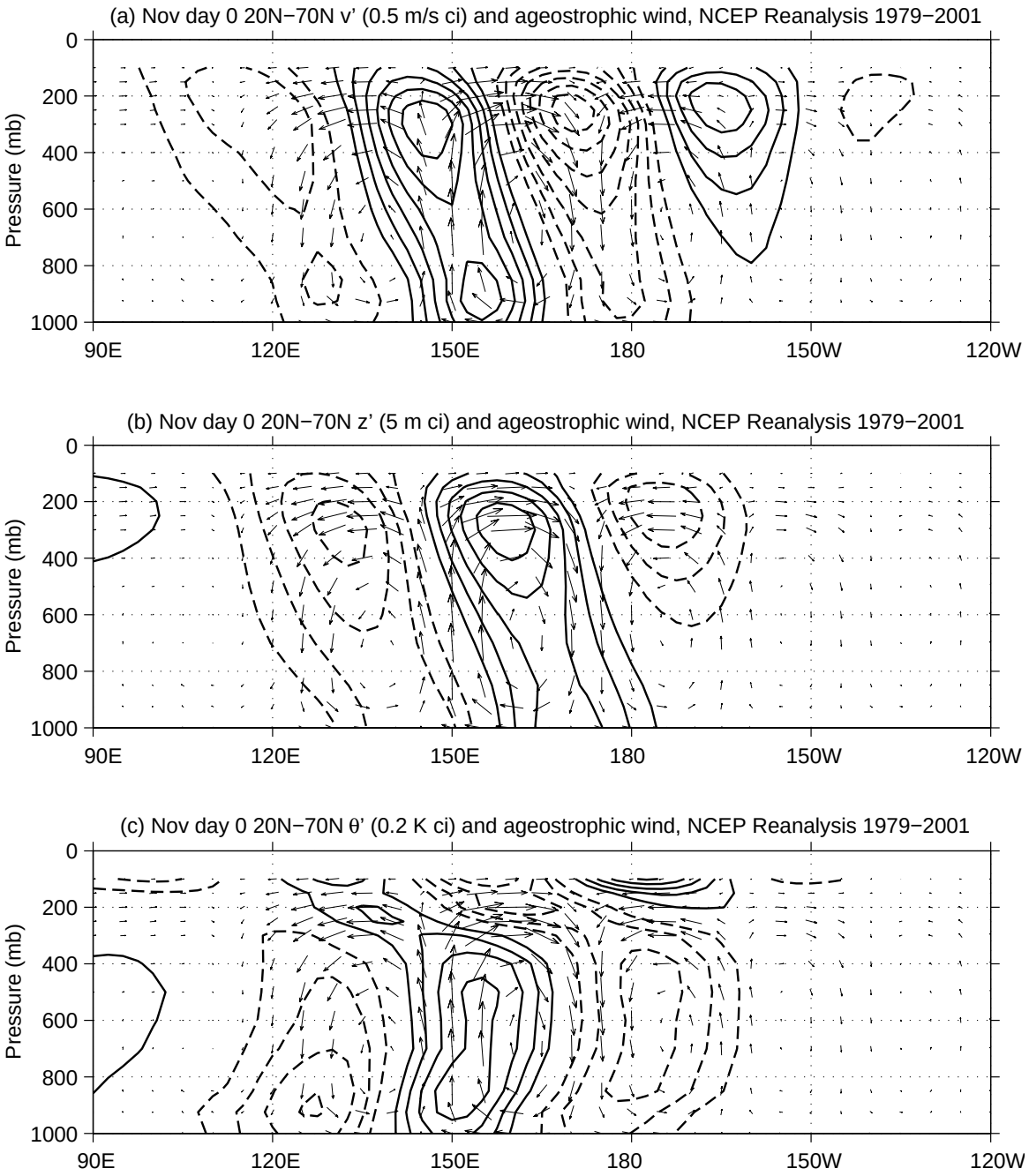

Figure 5.1: Regressions of (a) v' (contour interval 0.5 m/s), (b) z' (contour interval 5 m), (c) θ' (contour interval 0.2 K) on 925 mb v' at $155°$E, $37.5°$N; negative contours are dashed, and the zero contour omitted. Ageostrophic wind vectors (u'_a,ω') regressed on the same point are added to each panel. Quantities shown are mass-weighted averages between $20°$N and $70°$N at day 0 for November, based on NCEP Reanalysis data from September 1979 to August 2001.

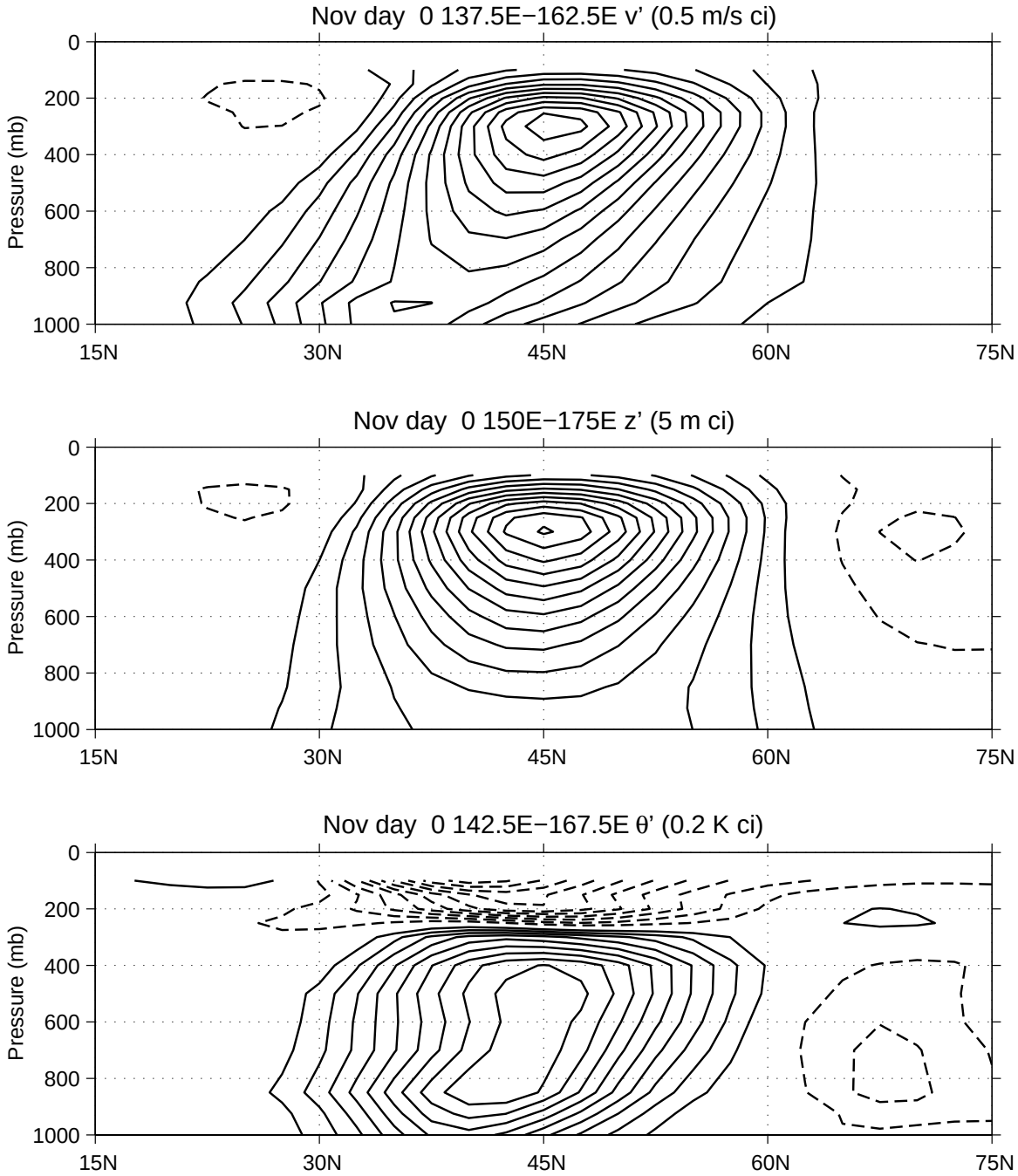

Figure 5.2: Zonal means of (a) v' (contour interval 0.5 m/s, averaged $137.5°$E-$162.5°$E), (b) z' (contour interval 5 m, averaged $150°$E-$175°$E), (c) θ' (contour interval 0.2 K, averaged $142.5°$E-$167.5°$E) regressed on 925 mb v' at $155°$E, $37.5°$N; negative contours are dashed, and the zero contour omitted. Each variable has been averaged over the half-wavelength where it is positive; the regressions shown are for day 0 in November, based on NCEP Reanalysis data from September 1979 to August 2001.

where the perturbation of that particular variable is positive. As predicted by Hoskins (1975), perturbations of all three variables tilt poleward with height, but v' tilts about twice as much (over 10° latitude from the surface to 300 mb) as z' and θ' (approximately 5° latitude from the surface to 300 mb). This raises two questions:

(1) If θ' is produced by v' blowing across the meridional temperature gradient, why does θ' tilt less than v'?

(2) If the wind in baroclinic waves is mostly geostrophic, why does v' tilt more than z'?

To answer the first question, we must consider the structure of both v' and $\partial\overline{\theta}/\partial y$, which act together to produce the temperature tendency due to $-v'(\partial\overline{\theta}/\partial y)$. Fig. 5.3 shows latitude-pressure profiles of v', $-v'(\partial\overline{\theta}/\partial y)$, and $-\partial\overline{\theta}/\partial y$ averaged over the half-wavelength of the wave where v' is poleward. Comparing Fig. 5.3b to Fig. 5.2b-c, $-v'(\partial\overline{\theta}/\partial y)$ has a poleward tilt similar to that of θ' and z' despite the much larger poleward tilt of v'. This is because the maximum of $-\partial\overline{\theta}/\partial y$ is oriented vertically directly under the jet, so the temperature tendency $-v'(\partial\overline{\theta}/\partial y)$ will tend to be more centered under the jet than v' alone, and will thus have a smaller poleward tilt with height than v'. As long as there is a concentrated temperature gradient under the jet with a latitude scale smaller than the poleward tilt of v' with height, the temperature perturbation induced by $-v'(\partial\overline{\theta}/\partial y)$ will have a smaller tilt with height than v'.

To answer the second question, we must examine the geostrophic (v'_g) and ageostrophic (v'_a) components of v' separately. Fig. 5.4 shows latitude-pressure profiles of v', v'_g, and v'_a averaged over the half-wavelength of the wave where v' is poleward. Comparing Fig. 5.4b with Fig. 5.2b, we see that, as expected, v'_g has approximately the same tilt with height as z'. In addition, v'_g is larger in amplitude than v'_a by at least a factor of 5. However, the ageostrophic wind is dominated by convergence at low levels and divergence aloft, with larger magnitudes on the equatorward flank of the wave for reasons to be discussed in the following section. Thus, on the equatorward flank of the baroclinic wave, v'_a is positive near the surface and negative at upper levels. When this v'_a structure is added to v'_g, the resulting total meridional wind v' has a considerably larger tilt than v'_g or z'. In this way,

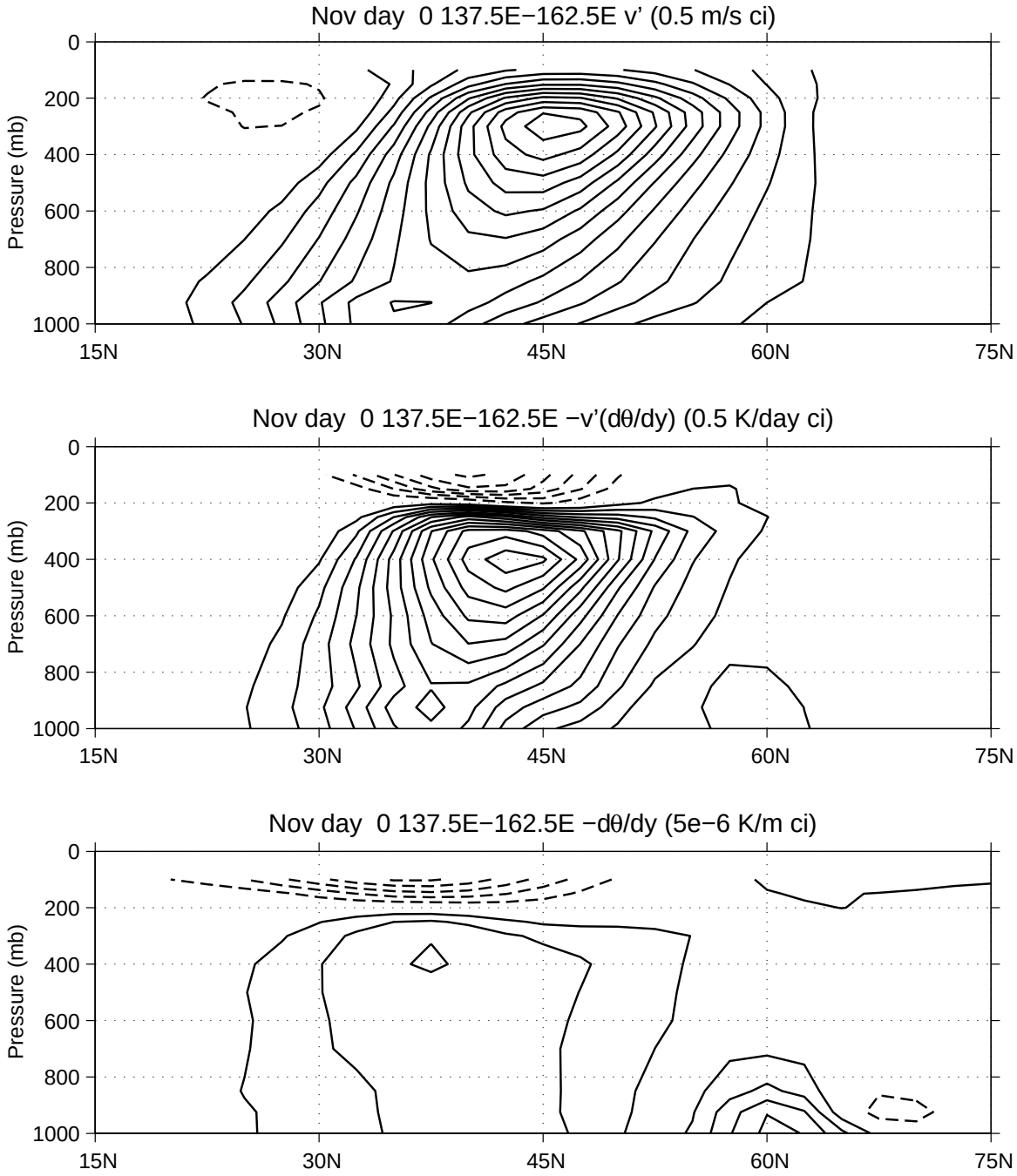

Figure 5.3: Zonal means of (a) v' (contour interval 0.5 m/s), (b) $-v'(\partial\overline{\theta}/\partial y)$ (contour interval 0.5 K/day), (c) $-\partial\overline{\theta}/\partial y$ (contour interval 5×10^{-6} K/m), based on regressions of v' on 925 mb v' at $155°$E, $37.5°$N and averaged from $137.5°$E to $162.5°$E; negative contours are dashed, and the zero contour omitted. The regressions shown are for day 0 in November, based on NCEP Reanalysis data from September 1979 to August 2001.

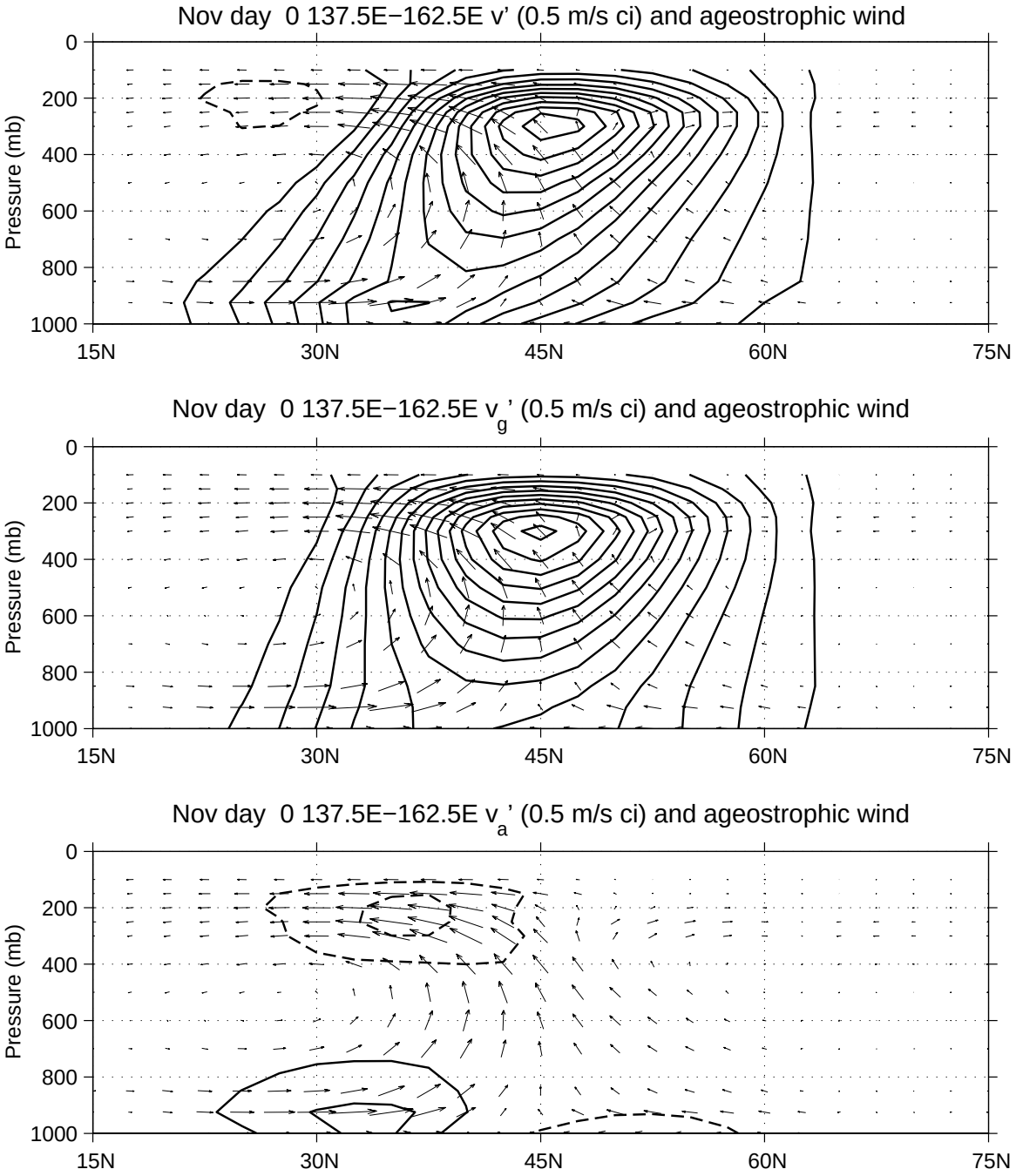

Figure 5.4: Zonal means of (a) v', (b) v'_g, (c) v'_a, based on regressions of v' on 925 mb v' at $155°$E, $37.5°$N and averaged from $137.5°$E to $162.5°$E. The contour interval is 0.5 m/s, negative contours are dashed, and the zero contour is omitted. Ageostrophic wind vectors (v'_a,ω') regressed on the same point are added to each panel. The regressions shown are for day 0 in November, based on NCEP Reanalysis data from September 1979 to August 2001.

the ageostrophic wind increases the poleward tilt with height of v' despite the fact that the geostrophic wind is much larger in magnitude than the ageostrophic wind.

Because θ' is generated by $-v'(\partial\overline{\theta}/\partial y)$, and v'_a enhances the poleward tilt with height of v', the ageostrophic temperature advection $-v'_a(\partial\overline{\theta}/\partial y)$ is instrumental in causing baroclinic waves to tilt poleward with height. The lack of a poleward tilt with height of baroclinic waves in quasigeostrophic models (e.g., Gall 1977) or the semigeostrophic model of Snyder et al. (1991), neither of which includes advection by the ageostrophic wind, provides further evidence that $-v'_a(\partial\overline{\theta}/\partial y)$ is responsible for the poleward tilt. In the following section, we investigate why the ageostrophic wind, and in particular its meridional component, has the structure that enhances the poleward tilt with height of baroclinic waves.

5.4 Theoretical explanation of the ageostrophic wind structure

An elegant explanation of the basic structure of the ageostrophic wind in baroclinic waves, with dominance of the zonal component at upper levels and dominance of the meridional component at lower levels, is given by Lim et al. (1991). Starting from the horizontal equation of motion

$$\frac{D\mathbf{v}}{Dt} + f\mathbf{k}\times\mathbf{v} = -\boldsymbol{\nabla}\Phi + \mathbf{F}_r \tag{5.2}$$

where

$$\frac{D}{Dt} = \frac{\partial}{\partial t} + \mathbf{v}\cdot\boldsymbol{\nabla} + \omega\frac{\partial}{\partial p}, \tag{5.3}$$

$\mathbf{v}$ is the total horizontal wind, f the Coriolis parameter, Φ the geopotential, and $\mathbf{F}_r$ the force due to friction, they neglect friction and note that the ageostrophic wind can be written as

$$\mathbf{v}_a \equiv \mathbf{v} - \mathbf{v}_g = \frac{\mathbf{k}}{f}\times\frac{D\mathbf{v}}{Dt} \tag{5.4}$$

where $\mathbf{v}_a$ is the variable f ageostrophic wind and $\mathbf{v}_g$ the geostrophic wind. Assuming a steady wave propagating zonally with phase speed c, they make use of the approximation

$$\frac{\partial}{\partial t} \approx -c\frac{\partial}{\partial x} \tag{5.5}$$

and, via plausible scaling arguments, arrive at the following estimates for the components of the ageostrophic wind in a baroclinic wave:

$$u'_{a1} \approx -\frac{1}{f}(\overline{u} - c)\frac{\partial v'_g}{\partial x} \tag{5.6}$$

$$v'_{a1} \approx -\frac{1}{f}\left[(\overline{u} - c)\frac{\partial u'_g}{\partial x} + v'_g\frac{\partial \overline{u}}{\partial y}\right] \tag{5.7}$$

where an overbar denotes a time mean (monthly mean for our analysis) and primes indicate departures from the time mean. Kwon and Lim (1999) show that including the time tendency due to the growth rate better explains the structure of the ageostrophic wind in growing baroclinic waves, and verify this result using a linear primitive equation numerical model (which also produces baroclinic waves that tilt poleward with height, although they do not mention this feature). However, we have calculated the ageostrophic wind using both the steady wave approximation in (5.5) and explicit calculations of $\partial/\partial t$ from the regression analysis, and, since neither gives results which are obviously better than the other, we continue to use the steady wave approximation in the calculations shown here.

We can now check whether these estimates accurately describe the observed ageostrophic winds in our regression analysis. The figures which follow compare the observed and calculated ageostrophic winds for day 0 of the regression analysis for November, but results are similar for January and for lags from day -2 to day +2. Fig. 5.5 shows a latitude-pressure cross section, averaged over the half-wavelength of the baroclinic wave where upper-level u'_a is positive, of the observed u'_a from the regression analysis, u'_{a1} calculated using (5.6), and the difference $u'_{a1} - u'_a$. Although there are some errors, particularly near the ground, the general structure of u'_{a1} matches u'_a quite well. Thus, the large zonal ageostrophic wind at upper levels in baroclinic waves (westerly in highs, easterly in lows) exists to provide a Coriolis force that balances the advection of v' by the strong zonal winds in the jet relative to the phase speed c of the wave, and u'_a tends to be large where the jet is strong.

The errors in the estimate of u'_a near the ground may be explained by the neglect of friction; if we include friction, the equation for the zonal component of the ageostrophic

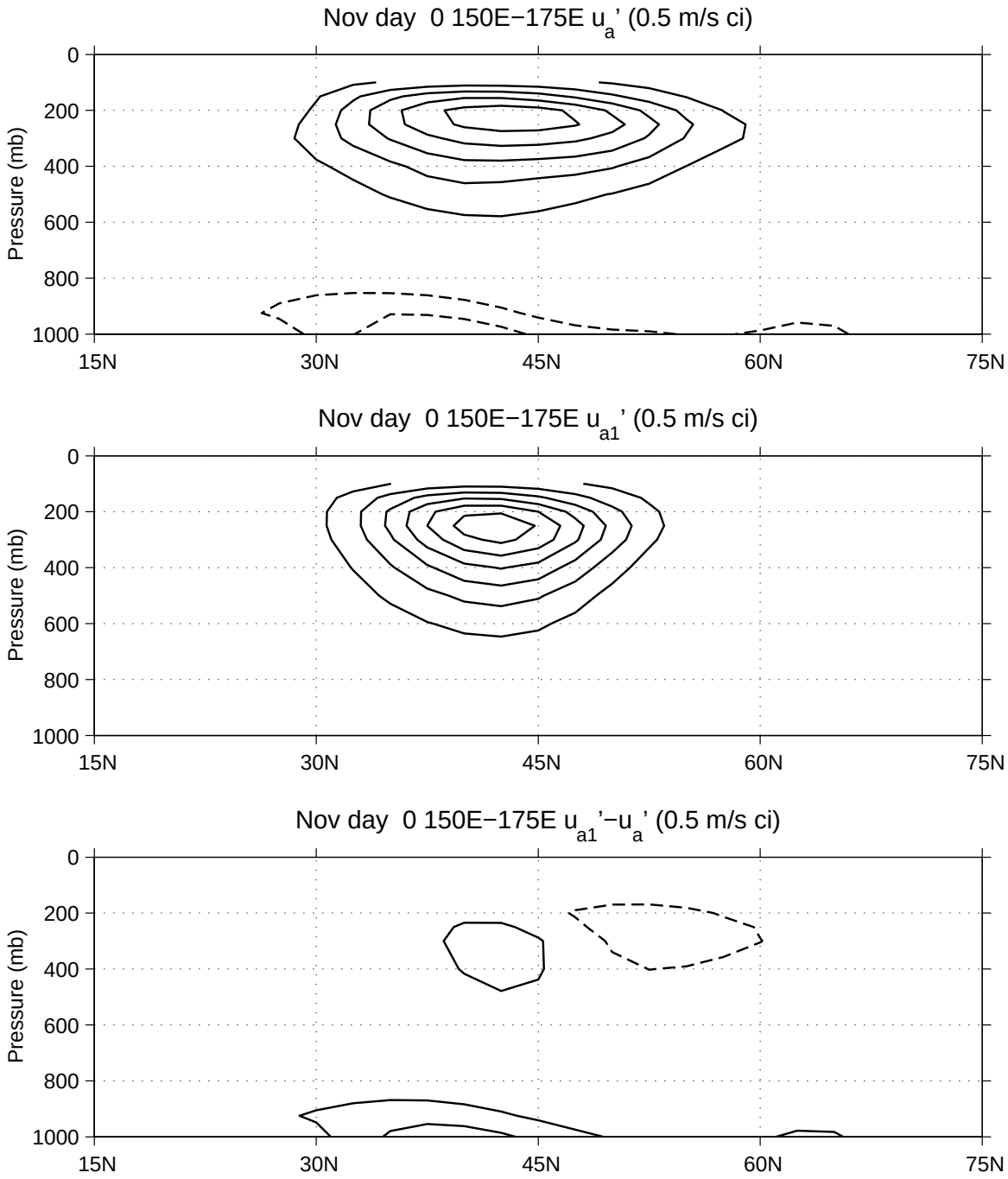

Figure 5.5: Zonal means of (a) u'_a, (b) $u'_{a1} \approx u'_a$ calculated using (5.6), (c) the error $u'_{a1} - u'_a$, from regressions on 925 mb v' at $155°$E, $37.5°$N and averaged from $150°$E to $175°$E. The contour interval is 0.5 m/s, negative contours are dashed, and the zero contour is omitted. The regressions shown are for day 0 in November, based on NCEP Reanalysis data from September 1979 to August 2001.

wind becomes

$$u_a = \frac{1}{f}\left[-\frac{Dv}{Dt} + F_{ry} \right] \tag{5.8}$$

where F_{ry} is the meridional component of the frictional force. Since the v' is poleward near the surface when averaged over this phase of the baroclinic wave, F_{ry} is negative, which will produce a negative u'_a near the surface, as we see in Fig. 5.5a. We note that neither adding more terms to calculate Dv/Dt more accurately nor explicitly calculating $\partial/\partial t$ instead of using $-c(\partial/\partial x)$ reduces the small errors in the calculation of u'_a at upper levels; further investigation of the deficiencies of this calculation are beyond the scope of the current work. Because $(\overline{u} - c)(\partial v'_g/\partial x)$ is the overwhelmingly dominant term in the equation for u'_a, the errors shown in Fig. 5.5c are of little consequence, so the calculation of u'_a by Lim et al. (1991) using (5.6) provides a satisfactory estimate of the u'_a that we observe in our regression analysis.

The same cannot be said for the estimate of v'_a calculated using (5.7). Fig. 5.6 shows a latitude-pressure cross section, averaged over the same half-wavelength as Fig. 5.4 where v' is poleward, of the observed v'_a from the regression analysis, v'_{a1} calculated using (5.7), and the difference $v'_{a1} - v'_a$. Instead of the equal magnitudes of equatorward v'_a at upper levels and poleward v'_a near the surface as observed in the regression analysis, the calculated v'_{a1} has much too strong equatorward flow aloft and weak poleward flow near the surface.

Further analysis reveals that some important terms have been left out of (5.7). First, u'_a is of comparable magnitude (3 m/s) to u'_g (6 m/s), and tends to be of opposite sign on the equatorward half of the baroclinic wave where it is largest, so including the $(\overline{u}-c)(\partial u'_a/\partial x)$ term is important. Second, v'_a can be large at upper levels on the equatorward half of the baroclinic wave, where there is strong meridional shear in the jet, so the $v'_a(\partial\overline{u}/\partial y)$ term should also be included. Third, it turns out that $\omega'(\partial\overline{u}/\partial p)$ due to the vertical motion in the strong vertical wind shear under the jet is of comparable magnitude to these other terms, so it must be included as well. Thus, we suggest that the modified estimate

$$v'_{a2} \approx -\frac{1}{f}\left[(\overline{u} - c)\frac{\partial u'}{\partial x} + v'\frac{\partial \overline{u}}{\partial y} + \omega'\frac{\partial \overline{u}}{\partial p} \right], \tag{5.9}$$

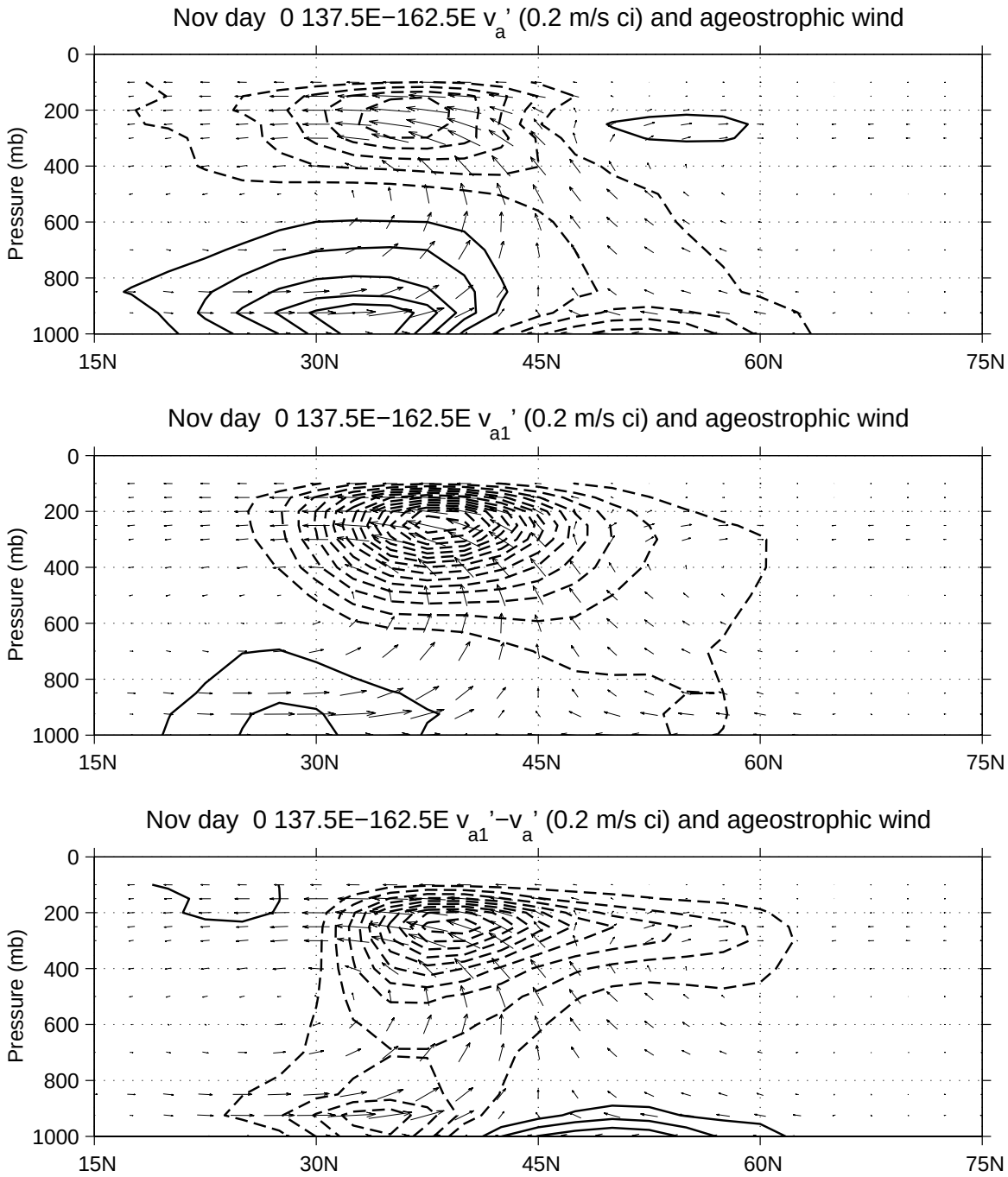

Figure 5.6: Zonal means of (a) v'_a, (b) $v'_{a1} \approx v'_a$ calculated using (5.7), (c) the error $v'_{a1} - v'_a$, from regressions on 925 mb v' at $155°$E, $37.5°$N and averaged from $137.5°$E to $162.5°$E. The contour interval is 0.2 m/s, negative contours are dashed, and the zero contour is omitted. Ageostrophic wind vectors (v'_a,ω') regressed on the same point are added to each panel. The regressions shown are for day 0 in November, based on NCEP Reanalysis data from September 1979 to August 2001.

which is essentially a combination of equations (18b) and (19b) in Kwon and Lim (1999), contains the minimum number of terms necessary to satisfactorily estimate v'_a in a baroclinic wave. Fig. 5.7 shows a latitude-pressure cross section of the observed v'_a from the regression analysis, the modified estimate v'_{a2} calculated using (5.9), and the difference $v'_{a2} - v'_a$. The structure of the v'_a field is now correct, and the magnitude of the equatorward v'_a at upper levels is quite good, although the poleward v'_a near the surface is still too weak.

As for u'_a, the deficiencies near the surface appear to be due to the neglect of friction. If we include friction, the equation for v_a becomes

$$v_a = \frac{1}{f}\left[\frac{Du}{Dt} - F_{rx}\right] \tag{5.10}$$

where F_{rx} is the zonal component of the frictional force. Because this phase of the baroclinic wave has low pressure at the surface, there are westerlies (and negative F_{rx}) which will induce poleward v'_a near $30°$N, and easterlies (and positive F_{rx}) which will induce equatorward v'_a near $45°$N. There are a number of smaller terms ($\overline{v}(\partial u'/\partial y)$, $v'(\partial u'/\partial y)$, $u'(\partial \overline{u}'/\partial x)$) which appear to have non-negligible effects on v'_a, but the importance of these terms is not as clear, and we leave investigation of the remaining small deficiencies in our calculation of v'_a to future work.

Now that we have a satisfactory estimate of the meridional ageostrophic wind in a baroclinic wave, we can explain the structure of v'_a. Fig. 5.8 shows the meridional ageostrophic wind produced by each of the three terms in (5.9). Each of the three terms produces poleward v'_a near the surface to provide a westerly Coriolis force to oppose the reduction of westerly momentum by advection. In the first term, the advection is due to easterly mean wind ($\overline{u} - c$, relative to the propagation of the wave) blowing from a surface high to a surface low on the equatorward flank of the wave near $25°$N; in the second term, the advection is due to poleward v' of the wave blowing towards stronger $\overline{u}$ on the equatorward flank of the jet near $30°$N; in the third term, the advection is due to upward motion towards the core of the jet between $35°$N and $40°$N. There is also convergence of v'_a at the surface to provide the appropriate Coriolis force to balance the friction acting on the winds in the surface low

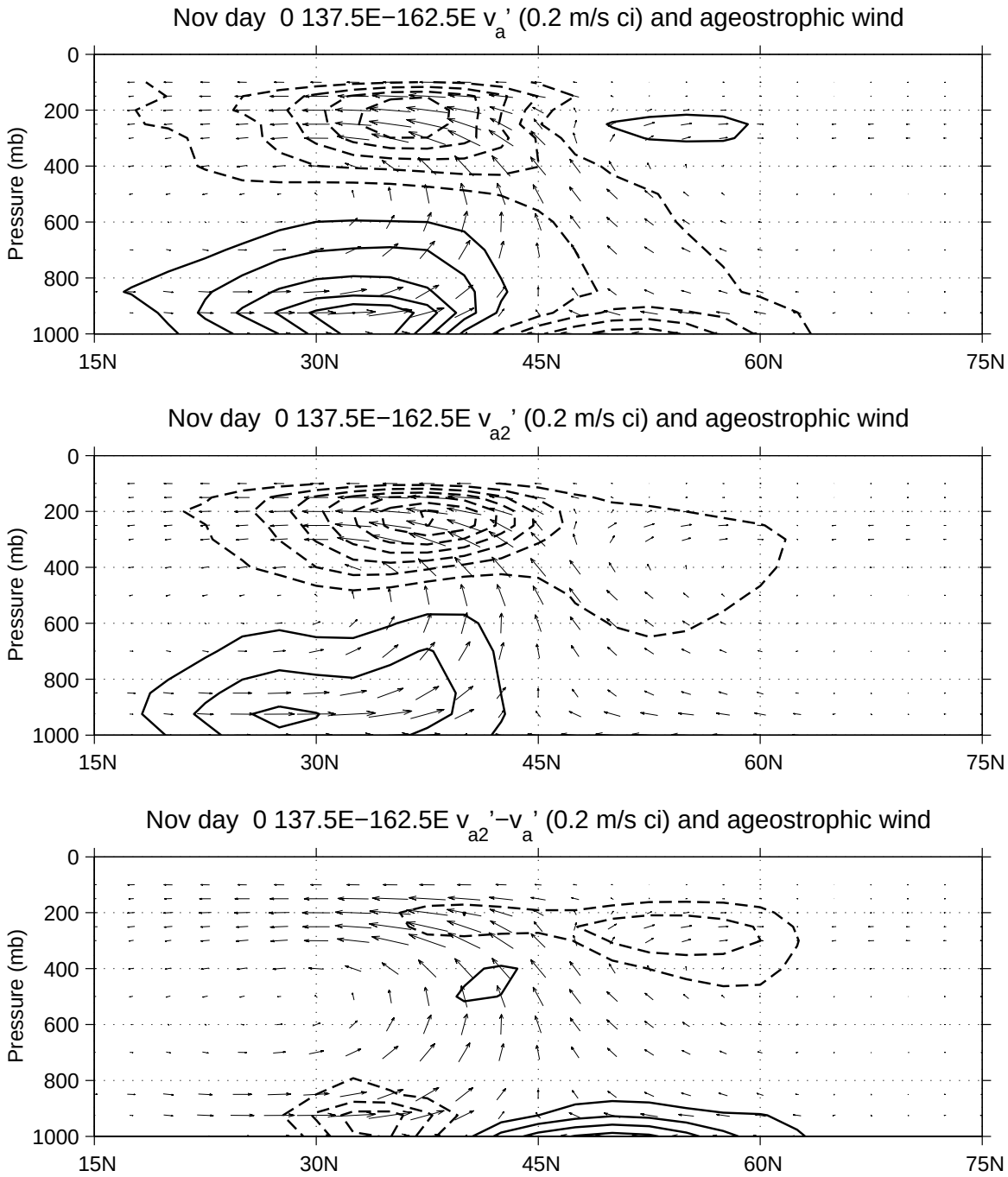

Figure 5.7: Zonal means of (a) v'_a, (b) $v'_{a2} \approx v'_a$ calculated using (5.9), (c) the error $v'_{a2} - v'_a$, from regressions on 925 mb v' at $155°$E, $37.5°$N and averaged from $137.5°$E to $162.5°$E. The contour interval is 0.2 m/s, negative contours are dashed, and the zero contour is omitted. Ageostrophic wind vectors (v'_a,ω') regressed on the same point are added to each panel. The regressions shown are for day 0 in November, based on NCEP Reanalysis data from September 1979 to August 2001.

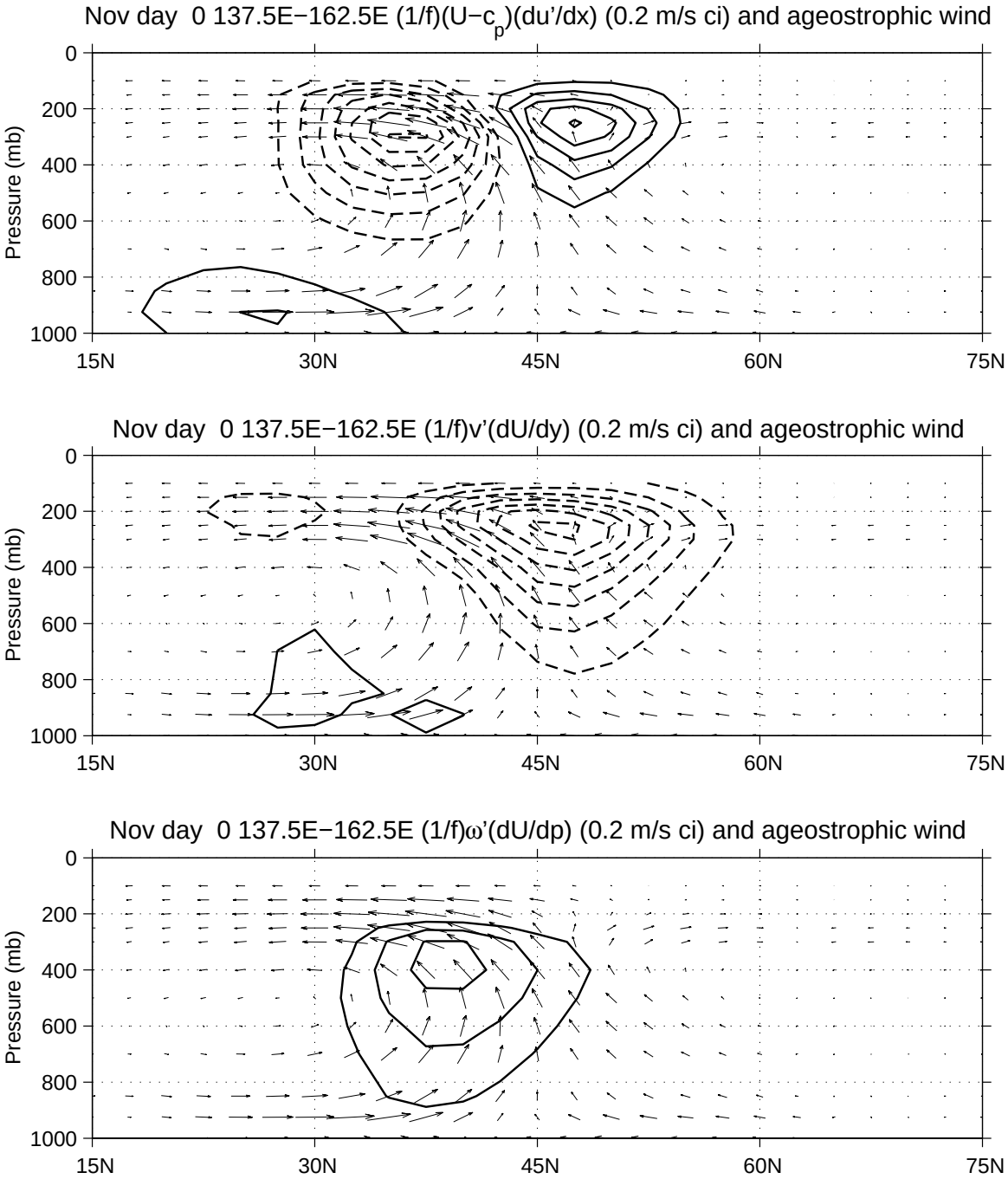

Figure 5.8: Zonal means of the three dominant terms in equation (5.9) for v'_a: (a) $f^{-1}(\overline{u} - c)(\partial u'/\partial x)$, (b) $f^{-1}v'(\partial\overline{u}/\partial y)$, (c) $f^{-1}\omega'(\partial\overline{u}/\partial p)$, calculated from regressions on 925 mb v' at $155°$E, $37.5°$N and averaged from $137.5°$E to $162.5°$E. The contour interval is 0.2 m/s, negative contours are dashed, and the zero contour is omitted. Ageostrophic wind vectors (v'_a,ω') regressed on the same point are added to each panel. The regressions shown are for day 0 in November, based on NCEP Reanalysis data from September 1979 to August 2001.

in this phase of the wave. At upper levels, there is some cancellation of terms, but there is mainly equatorward v'_a to provide an easterly Coriolis force to oppose the increase of westerly momentum due to westerly mean wind blowing from a low to a high on the equatorward flank of the wave near $35°$N (first term) and due to poleward v' of the wave blowing towards weaker $\overline{u}$ on the poleward flank of the jet near $45°$N (second term). In general, the ageostrophic wind will be stronger on the equatorward side of the wave for four reasons: (1) the $(1/f)$ factor gets larger towards the equator; (2) u'_a tends to make the $(\overline{u}-c)(\partial u'/\partial x)$ term larger on the equatorward side of the wave at upper levels; (3) the $v'(\partial\overline{u}/\partial y)$ term tends to enhance the effect of $(\overline{u}-c)(\partial u'/\partial x)$ on the equatorward side of the wave and oppose it on the poleward side of the wave; and (4) all three terms depend on $\overline{u}$, which is largest in the jet, and baroclinic waves growing in the baroclinic region under the jet tend to tilt so that they are on the poleward side of the jet at upper levels. However, even if the magnitude of the ageostrophic wind were not stronger on the equatorward side of the wave, the convergence (divergence) of v'_a near the surface and divergence (convergence) of v'_a aloft where v' is positive (negative) would increase the poleward tilt of v'.

We have examined the structure of the meridional ageostrophic wind because we want to understand how it modifies the structure of the meridional wind in baroclinic waves. In particular, we are interested in why the ageostrophic wind enhances the poleward tilt with height of v' in baroclinic waves. We have looked at the behavior of the ageostrophic wind in the half-wavelength of the baroclinic wave where v' is poleward, and now see two reasons that v'_a contributes to the poleward tilt with height of v': (1) in order to balance friction in the surface low in this phase of the wave, v'_a must be poleward in the equatorward half of the wave and equatorward in the poleward half of the wave at the surface, and (2) in order to balance advection of u' by the mean zonal wind blowing from a low to a high at upper levels, v'_a must be equatorward in the equatorward half of the wave and poleward in the poleward half of the wave at upper levels. Since the remaining two major terms ($v'(\partial\overline{u}/\partial y)$ and $\omega'(\partial\overline{u}/\partial p)$) that determine v'_a tend to increase the poleward tilt of v' at low levels and decrease the poleward tilt of v' at upper levels, the two factors mentioned above dominate

to produce the increased poleward tilt with height of v' seen in Fig. 5.4.

5.5 Summary and conclusions

Our regression analysis has shown that baroclinic waves do indeed tilt poleward with height, as predicted by many primitive equation model simulations of baroclinic waves (e.g., Gall 1977) and hinted at by figures from previous regression analyses of baroclinic wave structure (e.g., Chang 2001). This tilt with height is largest in v', and somewhat smaller in z' and θ', as predicted by Hoskins (1975). We have demonstrated that the meridional ageostrophic wind v'_a acts to enhance the poleward tilt of v' over the tilt it would have if it were purely geostrophic. We have also argued that temperature advection by the meridional ageostrophic wind $-v'_a(\partial\overline{\theta}/\partial y)$ is responsible for the tilt of the baroclinic waves in the first place, a conclusion supported by the lack of poleward tilt in baroclinic waves in quasigeostrophic and semigeostrophic models which do not include advection by the ageostrophic wind. We extend the results of Lim et al. (1991) and Kwon and Lim (1999) to show that the ageostrophic wind has its observed structure in order to maintain force balance and keep the baroclinic wave intact as a propagating entity, and in particular show that friction is important in determining the ageostrophic wind near the surface.

Although our conclusions do not disagree with previous studies on baroclinic waves, and may seem obvious after reading the references cited here, we are unaware of any observational study of the poleward tilt with height of baroclinic waves, or any published explanation of the phenomenon other than that of Hoskins (1975). In fact, conversations at a recent meeting seem to suggest that many scientists studying storm tracks and baroclinic waves are unaware that baroclinic waves tilt poleward with height. The poleward tilt of baroclinic waves is more than just an academic curiosity, since it explains the observation that the upper level storm tracks tend to occur poleward of near-surface baroclinic regions. In addition, this innate property of baroclinic waves appears to play a role in the midwinter suppression of the Pacific storm track by placing the upper level structure of baroclinic

waves on the poleward side of the Pacific jet, where the lowering of the tropopause in midwinter reduces the efficiency of eddy energy generation.

Chapter 6

DISCUSSION AND CONCLUSIONS

In this thesis, we have used NCEP Reanalysis data from September 1979 to August 2001 to study the observed midwinter suppression of the Pacific storm track. Our main finding is that the efficiency of eddy energy production is reduced in midwinter, primarily because of the increased upper level static stability associated with the lowering of the tropopause. The following section contains a more complete summary of our results.

6.1 Summary of results

We find that the midwinter suppression of the Pacific storm track occurs primarily above 500 mb, and involves an equatorward shift and overall weakening of the storm track at upper levels across the western and central Pacific. In terms of eddy TE averaged from $20°$N to $70°$N and from 100 mb to 500 mb across the longitudes of the suppression, the storm track intensity decreases by 9% from its fall maximum in November to its midwinter minimum in January, and is 13% less in January than at its spring maximum in April.

Previous work (Nakamura 1992, Christoph et al. 1997, Zhang 1997) has demonstrated a negative correlation between jet speed and storm track intensity in the Pacific in midwinter. We show that, as the Pacific jet strengthens and becomes more subtropical in midwinter, the tropopause height drops steeply on its poleward flank. A pair of idealized GCM experiments show that a strengthening of tropical convection south of the equator in the western Pacific, as occurs in midwinter, can cause the stationary wave response that produces these changes in the Pacific jet and tropopause. Thus, tropical convection appears to provide the external forcing that causes the tropopause to drop more steeply across the Pacific jet when

it becomes more subtropical in midwinter; this does not occur in the Atlantic because of the weak tropical influence on the eddy-driven Atlantic jet.

Our eddy energy budget analysis indicates that changes in the efficiency of eddy energy production are responsible for the bulk of the midwinter suppression of the Pacific storm track, while processes which affect the transport and decay of eddy energy are unlikely to force the suppression. Changes in baroclinic wave structure reduce the efficiency of baroclinic generation of eddy APE in January by factors of 0.86 relative to November and 0.84 relative to April; decreased moisture reduces the efficiency of baroclinic conversion from eddy APE to eddy KE by factors of 0.95 relative to November and 0.93 relative to April, while increased static stability reduces the efficiency of baroclinic conversion only relative to April, by a factor of 0.93; and the shallower baroclinic generation and baroclinic conversion in January reduce the fraction of eddy KE that persists by factors of 0.89 relative to November and 0.86 relative to April.

Lag regression analysis reveals that most of the decrease in the efficiency of eddy energy production in midwinter can be attributed to the increase in upper level static stability associated with the lowering of the tropopause over the Pacific. The larger upper level static stability causes all of the effect of shallowing, most of the overall effect of static stability, and at least half of the effect of changes in baroclinic wave structure. The increase in zonal wind increases the tilt of temperature perturbations in baroclinic waves in midwinter, which is responsible for the remainder of the effect of changes in baroclinic wave structure. Thus, the lowering of the tropopause on the poleward flank of the Pacific jet drives most of the midwinter suppression, while increased zonal wind and decreased moisture play smaller supporting roles.

The importance of conditions at upper levels on the poleward flank of the jet is also explained by our lag regression analysis, which shows that baroclinic waves tilt poleward with height and therefore have their largest upper level amplitude on the poleward side of the jet. We demonstrate that the ageostrophic winds that balance the momentum advection and surface friction in propagating baroclinic waves enhance the poleward tilt of meridional

wind perturbations in baroclinic waves. We also suggest that temperature advection by the ageostrophic wind is responsible for the poleward tilt of temperature and geopotential height perturbations in baroclinic waves; this is supported by the lack of a poleward tilt in baroclinic waves simulated by models that do not include advection by the ageostrophic wind (Gall 1977, Snyder et al. 1991). The poleward tilt with height of baroclinic waves enables the lowering of the tropopause on the poleward flank of the jet to more effectively suppress the Pacific storm track in midwinter.

The most relevant variables for understanding the midwinter suppression of the Pacific storm track are summarized in Fig. 6.1 for November, January, and April. In this study, we have typically viewed the suppression in the longitude-pressure plane, but Fig. 6.1 shows the suppression in the latitude-pressure plane, zonally averaged across the sector where the suppression is most strongly forced ($100°$E-$180°$), in order to illustrate the variations of jet strength, storm track intensity, and tropopause height as a function of latitude. First, the jet strength, in terms of mean zonal wind, is shown in black contours; although the jet core shifts only slightly equatorward in midwinter, its maximum in this sector is much greater in January (69 m/s) than in November (50 m/s) or April (42 m/s), and the jet is considerably narrower in January as well. The storm track intensity, in terms of eddy TE, is shown in color; it tilts poleward with height, so that its upper level maximum lies well poleward of the jet core (the equatorward bulge at upper levels is due to the equatorward propagation of eddy KE during the later stages of the baroclinic life cycle). The storm track intensity is clearly smaller in January than in November or April, particularly at upper levels, and appears to have shifted equatorward. The approximate tropopause height is shown by thick blue contours of two values of the Brunt-Väisälä frequency (0.014 s^{-1} and 0.018 s^{-1}) that are representative of the static stability near the tropopause. It is clear that the tropopause becomes more vertically oriented in the vicinity of the strong, narrow jet in January; while the tropopause rises slightly on the equatorward side of the jet, the lowering of the tropopause on the poleward side of the jet, by as much as 100 mb, is more important because the maximum storm track intensity occurs poleward of the jet. We have

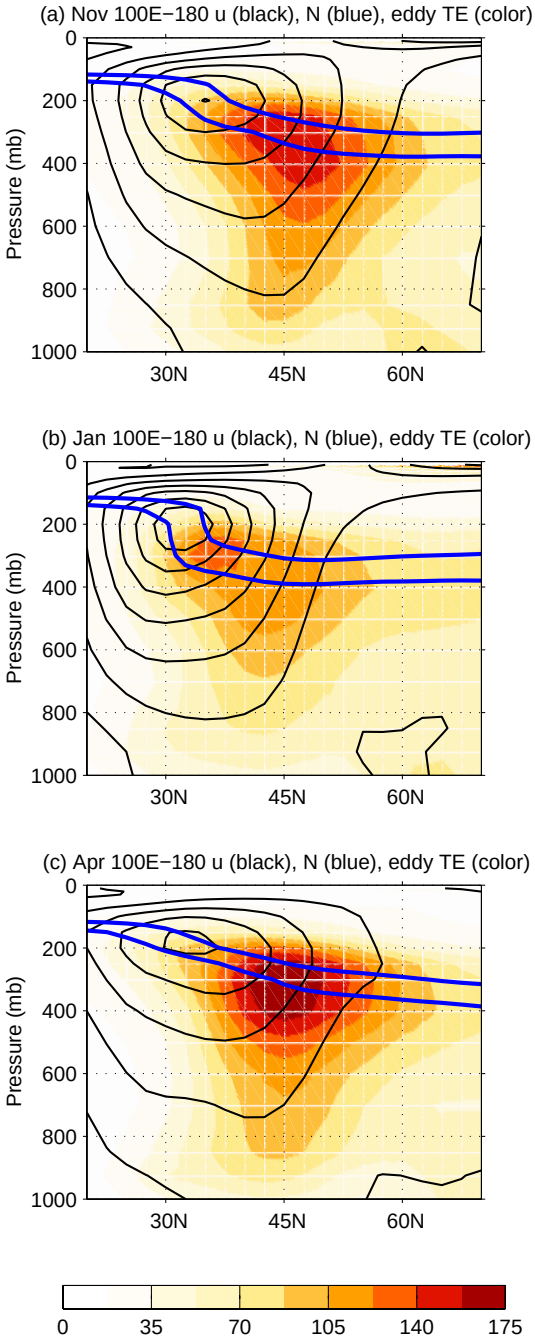

Figure 6.1: Summary of important variables in the midwinter suppression of the Pacific storm track, zonally averaged across the region where the suppression is forced (100°E-180°), for (a) November, (b) January, (c) April. Storm track intensity, in terms of eddy TE, is shown in color (contour interval 17.5 m^2/s^2). Jet strength, in terms of mean zonal wind, is shown in black contours (contour interval 10 m/s). Tropopause height is indicated by thick blue contours of two near-tropopause values of the Brunt-Väisälä frequency: 0.014 s^{-1} (lower blue line) and 0.018 s^{-1} (upper blue line). Calculations are based on NCEP Reanalysis data from September 1979 to August 2001.

demonstrated in this study that the larger static stability at upper levels associated with the lowering of the tropopause reduces the amount of eddy energy delivered to upper levels, and Fig. 6.1 shows that the region of reduced upper level eddy TE above 400 mb and poleward of $40°$N coincides with the region where the tropopause is lower in midwinter.

6.2 Discussion

At first glance, the equatorward shift of the maximum storm track intensity in midwinter appears to support the suggestion by Nakamura and Sampe (2002) that transient eddies are more trapped by the strong PV gradients in the subtropical jet in midwinter. However, an alternative explanation is that upper level eddy energy has been reduced by the lowering of the tropopause everywhere except very near the subtropical jet, so the eddies appear to be more trapped in the jet because that is the only place where they can achieve large amplitudes. While Nakamura and Sampe (2002) use lag regression analysis to demonstrate that the maximum eddy amplitude is more likely to occur in the Pacific jet core when it is stronger, a more detailed regression analysis would be useful for clarifying the roles of the PV gradient and static stability in determining the structure of baroclinic waves in midwinter.

The results presented in this thesis pertain mostly to the midwinter suppression of the Pacific storm track at upper levels. While the results of Nakamura (1992) show that the suppression is largest at upper levels, he also shows smaller decreases in storm track intensity at lower levels, particularly in terms of 850 mb $v'\theta'$, which we have not addressed. Our analysis shows that while eddy KE and eddy APE change little at lower levels (see Figs. 2.6 and 2.7), the decrease in the correlation between v' and θ' at low levels (see Figs. 3.5a and e) could explain the small midwinter decrease in 850 mb $v'\theta'$. Nakamura et al. (2002) recently found large interannual variations in midwinter 850 mb $v'\theta'$ that are also accompanied by changes in the correlation between v' and θ'. However, these variations in 850 mb $v'\theta'$ (by a factor of 2) are unlikely to be explained by the difference in correlation alone. The reduc-

tion in upper level eddy energy generation due to the lowering of the tropopause could act to decrease low level storm track activity because less eddy energy propagates downward, although that has not been demonstrated in this thesis; the cause of the changes in 850 mb $v'\theta'$ should be more apparent from an analysis of its interannual variations, because these are larger than its seasonal variations. Because 850 mb $v'\theta'$ and upper level storm track intensity are larger in the Pacific during winters with a weak jet than during winters with a strong jet, it is very likely that the same mechanisms that cause the midwinter suppression are also responsible for the interannual variations in Pacific storm track intensity. Application of the analysis techniques used in this thesis to the interannual variations in Pacific storm track intensity would be a useful test of the importance of tropopause height for the suppression of the Pacific storm track.

The large 850 mb $v'\theta'$ found by Nakamura et al. (2002) during winters with weak suppression emphasizes that the midwinter suppression of the Pacific storm track is all the more impressive given that the maximum baroclinicity occurs during midwinter. In the absence of other changes, the larger temperature gradient would enhance baroclinic generation and the stronger jet would enhance baroclinic conversion, both of which would increase storm track intensity relative to spring or fall. In order to produce the observed midwinter suppression, these effects must be overcome by the increased static stability associated with the lowering of the tropopause, with smaller contributions from decreased moisture and increased jet strength. We find that a reduction in the efficiency of eddy energy production by 27% relative to November and 38% relative to April (based on the products of the ratios shown in Table 3.1) is required to produce the observed $\sim$10% reduction in storm track intensity relative to both months. It is the coincidence of the midwinter minimum in Pacific storm track intensity with the midwinter maximum in baroclinicity, rather than the relatively small midwinter decrease in storm track intensity alone, that makes the midwinter suppression an interesting and important phenomenon to explain.

6.3 Revised explanation for midwinter suppression

We revisit the five previous explanations for midwinter suppression presented in section 1.4:

1) Diabatic generation: We confirm the result of Chang (2001) that the reduced moisture in midwinter decreases the diabatic generation of eddy energy. However, the decrease in the efficiency of baroclinic conversion from eddy APE to eddy KE due to reduced moisture is small relative to the other decreases in efficiency of eddy energy production, so the reduced moisture in midwinter plays at best a secondary role in forcing the midwinter suppression of the Pacific storm track. Damping of APE by sensible heating appears to be unimportant for the suppression, since the rate of damping increases by no more than 4% in midwinter relative to fall or spring, and changes in eddy energy production at upper levels are more likely to affect storm track intensity.

2) Upper or lower level trapping of baroclinic waves: We confirm that baroclinic waves have shallower structures in the Pacific storm track in midwinter, particularly in temperature, and show that this shallowing is caused by the lowering of the tropopause. We demonstrate that the shallower baroclinic waves lose a larger fraction of their eddy KE to friction, which contributes to the midwinter suppression. Additional lag regression analysis not shown in this thesis confirms the results of Chang (2001) and Nakamura and Sampe (2002) that upper level baroclinic waves tend to be more trapped in the subtropical jet, where they also have limited vertical extent, in midwinter. However, the reduced baroclinic generation of eddy APE in these waves could be offset by increased barotropic conversion of eddy KE from the mean flow, so the effect of trapping in the subtropical jet on the growth rate of baroclinic waves is unclear.

3) Seeding: Although our results suggest that local changes in the efficiency of eddy energy production are responsible for most of the midwinter suppression, our lag regression and eddy energy budget analysis could not directly assess the amount of eddy energy associated with baroclinic waves propagating from upstream of the Pacific storm track. The

EOF analysis of Zhang (1997) remains the most convincing evidence that seeding is not important for the midwinter suppression of the Pacific storm track.

4) Excessive advection: The changes in the advective convergence of eddy energy are of the wrong sign to drive the midwinter suppression, although they do appear to increase the downstream extent of the suppression, as expected. This supports the conclusions of Zhang (1997) and Chang (2001) that excessive advection by the strong midwinter jet does *not* cause the midwinter suppression of the Pacific storm track because the group velocity of baroclinic waves changes little in midwinter. However, the stronger zonal wind in midwinter appears to make a small contribution to the midwinter suppression by increasing the eastward tilt of temperature perturbations in baroclinic waves.

5) Enhanced diffluence: We confirm the result of Chang (2001) that barotropic conversion is less negative in midwinter than in fall, so enhanced diffluence in the exit of the stronger Pacific jet cannot cause the midwinter suppression.

Of the previously suggested mechanisms, the reduced vertical extent of baroclinic waves seems to be the most important for causing the midwinter suppression, although reduced diabatic generation by moist heating and increased advection of eddy temperature perturbations also appear to make small contributions. We emphasize that the increased static stability due to the lowering of the tropopause in midwinter, rather than a "barotropic governor" or other dynamical mechanism, is responsible for the shallowing of temperature perturbations in baroclinic waves that drives much of the midwinter suppression. To our knowledge, this is the first demonstration of the importance of tropopause height in the midwinter suppression of the Pacific storm track.

6.4 Concluding remarks

We conclude that the paradox of the midwinter minimum in Pacific storm track intensity during the time of maximum baroclinicity in the Pacific can be explained as follows: Although the maximum baroclinicity in the Pacific storm track occurs in conjunction with the

strong Pacific jet in January, the decrease in tropopause height on the poleward flank of the strong midwinter jet reduces the efficiency of eddy energy production to more than compensate for the increase in baroclinicity. As a result, the amount of eddy energy delivered to upper levels in January is less than that in November or April despite the greater baroclinicity. Because the strengthening of the jet and the associated lowering of the tropopause are driven by tropical convection, the midwinter suppression of the storm track is observed only in the Pacific sector, where tropical forcing of the jet is most important. This raises the interesting possibility that stronger tropical convection in a warmer world could oppose the effects of increased moisture in the storm tracks. We look forward to future work on the interactions between transient eddies and the mean flow and the role of moisture in baroclinic waves that will provide more insight on how storm tracks may change in a warmer world.

BIBLIOGRAPHY

Blackmon, M. L., 1976: A climatological spectral study of the 500 mb geopotential height of the Northern Hemisphere. *J. Atmos. Sci.*, **33**, 1607–1623.

Blackmon, M. L., Y.-H. Lee and J. M. Wallace, 1984: Horizontal structure of 500 mb height fluctuations with long, intermediate, and short time scales. *J. Atmos. Sci.*, **41**, 961–979.

Blackmon, M. L., J. M. Wallace, N.-C. Lau and S. L. Mullen, 1977: An observational study of the Northern Hemisphere wintertime circulation. *J. Atmos. Sci.*, **34**, 1040–1053.

Chang, E. K. M., 1993: Downstream development of baroclinic waves as inferred from regression analysis. *J. Atmos. Sci.*, **50**, 2038–2053.

Chang, E. K. M., 2001: GCM and observational diagnoses of the seasonal and interannual variations of the Pacific storm track during the cool season. *J. Atmos. Sci.*, **58**, 1784–1800.

Christoph, M., U. Ulbrich and P. Speth, 1997: Midwinter suppression of Northern Hemisphere storm track activity in the real atmosphere and in GCM experiments. *J. Atmos. Sci.*, **54**, 1589–1599.

Gall, R., 1977: Some non-quasigeostrophic effects in linear baroclinic waves. *Mon. Wea. Rev.*, **105**, 1039–1051.

Holton, J. R., 1992: *An Introduction to Dynamic Meteorology*. Academic Press, 511 pp.

Hoskins, B. J., 1975: The geostrophic momentum approximation and the semi-geostrophic equations. *J. Atmos. Sci.*, **32**, 233–242.

Hoskins, B. J. and P. J. Valdes, 1990: On the existence of storm tracks. *J. Atmos. Sci.*, **47**, 1854–1864.

James, I. N., 1987: Suppression of baroclinic instability in horizontally sheared flows. *J. Atmos. Sci.*, **44**, 3710–3720.

Kiehl, J. T., J. J. Hack, G. B. Bonan, B. A. Boville, B. P. Brieglieb, D. L. Williamson and P. J. Rasch, 1996: Description of the NCAR Community Climate Model (CCM3). Tech. rep., NCAR, 152 pp. [Available from NCAR, Boulder, CO 80307].

Kwon, H. J. and G.-H. Lim, 1999: Reexamination of the structure of the ageostrophic wind in baroclinic waves. *J. Atmos. Sci.*, **56**, 2512–2521.

Lim, G. H., J. R. Holton and J. M. Wallace, 1991: The structure of the ageostrophic wind field in baroclinic waves. *J. Atmos. Sci.*, **48**, 1733–1745.

Lim, G. H. and J. M. Wallace, 1991: Structure and evolution of baroclinic waves as inferred from regression analysis. *J. Atmos. Sci.*, **48**, 1718–1732.

Lindzen, R. S. and B. F. Farrell, 1980: A simple approximate result for the maximum growth rate of baroclinic instabilities. *J. Atmos. Sci.*, **37**, 1648–1654.

Lorenz, E. N., 1955: Available potential energy and the maintenance of the general circulation. *Tellus*, **7**, 157–167.

Nakamura, H., 1992: Midwinter suppression of baroclinic wave activity in the Pacific. *J. Atmos. Sci.*, **49**, 1629–1642.

Nakamura, H., T. Izumi and T. Sampe, 2002: Interannual and decadal modulations recently observed in the Pacific storm track activity and east Asian winter monsoon. *J. Climate*, **15**, 1855–1874.

Nakamura, H. and T. Sampe, 2002: Trapping of synoptic-scale disturbances into the North Pacific subtropical jet core in midwinter. *Geophys. Res. Lett.*, submitted.

Nigam, S. and R. S. Lindzen, 1989: The sensitivity of stationary waves to variations in the basic state zonal flow. *J. Atmos. Sci.*, **46**, 1746–1768.

Orlanski, I. and J. Katzfey, 1991: The life cycle of a cyclone wave in the Southern Hemisphere. Part I: Eddy energy budget. *J. Atmos. Sci.*, **48**, 1972–1998.

Simmons, A. J. and B. J. Hoskins, 1976: Baroclinic instability on the sphere: Normal modes of the primitive and quasi-geostrophic equations. *J. Atmos. Sci.*, **33**, 1454–1477.

Simmons, A. J. and B. J. Hoskins, 1978: The life cycles of some nonlinear baroclinic waves. *J. Atmos. Sci.*, **35**, 414–432.

Snyder, C., W. C. Skamarock and R. Rotunno, 1991: A comparison of primitive-equation and semigeostrophic simulations of baroclinic waves. *J. Atmos. Sci.*, **48**, 2179–2194.

Thorncroft, C. D., B. J. Hoskins and M. E. McIntyre, 1993: Two paradigms of baroclinic-wave life-cycle behaviour. *Q. J. R. Meteorol. Soc.*, **119**, 17–55.

Trenberth, K. E., 1991: Storm tracks in the Southern Hemisphere. *J. Atmos. Sci.*, **48**, 2159–2178.

Wallace, J. M., G.-H. Lim and M. L. Blackmon, 1988: Relationship between cyclone tracks, anticyclone tracks and baroclinic waveguides. *J. Atmos. Sci.*, **45**, 439–462.

Zhang, Y., 1997: *On the mechanisms for the mid-winter suppression of the Pacific storm-track*. Ph.D. thesis, Princeton University, 152 pp.

VITA

JEFFREY H. YIN

Department of Atmospheric Sciences

University of Washington – JISAO, Box 354235

Seattle, WA 98195-4235

Phone: 206.685.3602

Fax: 206.685.3397

email: jyin@atmos.washington.edu

EDUCATION

Ph.D. Atmospheric Sciences, University of Washington, August 2002 (expected). Advisors: David S. Battisti and Edward S. Sarachik.

B.A. Applied Mathematics, Harvard University, June 1995.

EMPLOYMENT

Research Assistant, Atmospheric Sciences, University of Washington (Sept 1995-present). Studied storm tracks using the NCEP Reanalysis and NCAR CCM3.6 general circulation model, paleoclimate using the CCM3.6, and the global carbon cycle using simple box models.

Teaching Assistant, University of Washington, OCEAN 529B/ATM S 591A: Modeling the Global Carbon Cycle (March-June 2002).

Teaching Assistant, University of Washington, ATM S 101: Weather, (Jan-March 1997).

Research Assistant, Atmospheric Chemistry, Harvard University (June-Aug 1995). Analyzed 15 years of EPA ozone data using Fortran and S-Plus.

Research Assistant, Cloud Physics, University of Hawaii (June-Aug 1993 and 1994). Performed lab tests on particle measuring equipment and participated in 5-week field experiment to study aerosols on Christmas Island.

JOURNAL PUBLICATIONS

Seager, R., D. S. Battisti, J. Yin, N. Naik, A. C. Clement, and M. A. Cane, 2002: Is the Gulf Stream responsible for Europe's mild winters? Accepted, *Q. J. R. Meteorol. Soc.*

Yin, J. H., and D. S. Battisti, 2001: The importance of tropical sea surface temperature patterns in simulations of Last Glacial Maximum Climate. *J. Climate*, **14**, 565-581.

Fiore, A. M., D. J. Jacob, J. A. Logan, and J. H. Yin, 1998: Long-term trends in ground level ozone over the contiguous Unived States. *J. Geophys. Res.*, **103**(D1), 1471–1480.

CONFERENCES AND WORKSHOPS ATTENDED:

May 2002: AGU Spring Meeting, Washington, DC (presented).

June 2001: NCAR CSM Workshop, Breckenridge, CO.

June 2001: U.S. CLIVAR Atlantic Meeting, Boulder, CO.

June 2001: AMS 13th Conference on Atmospheric and Oceanic Fluid Dynamics, Breckenridge, CO (presented).

June 1998: NCAR CSM Workshop, Breckenridge, CO.

May 1998: NATO ASI on Numerical Modeling of the Global Atmosphere, Castelvecchio Pascoli, Italy.

HONORS AND AWARDS:

October 2002-: NOAA Postdoctoral Program in Climate and Global Change Fellowship.

June 2001: Outstanding Student Presentation, American Meteorological Society 13th Conference on Atmospheric and Oceanic Fluid Dynamics, Breckenridge, CO.

Sept 1995-Sept 1998: National Science Foundation Graduate Research Fellowship.